Improved Collision Modeling for Direct Simulation Monte Carlo Methods

THESIS

Sarah E. Summers, Captain, USAF

AFIT/GAE/ENY/11-M29

DEPARTMENT OF THE AIR FORCE
AIR UNIVERSITY

AIR FORCE INSTITUTE OF TECHNOLOGY

Wright-Patterson Air Force Base, Ohio

AFIT/GAE/ENY/11-M29

Improved Collision Modeling for Direct Simulation Monte Carlo Methods

THESIS

Presented to the Faculty

Department of Aeronautics and Astronautics

Graduate School of Engineering and Management

Air Force Institute of Technology

Air University

Air Education and Training Command

In Partial Fulfillment of the Requirements for the

Degree of Master of Science in Aeronautical Engineering

Sarah E. Summers, BS

Captain, USAF

March 2011

Improved Collision Modeling for Direct Simulation Monte Carlo Methods

Sarah E. Summers, BS

Captain, USAF

Approved:

_____	_____
Robert B. Greendyke, PhD (Chairman)	date
_____	_____
Lt Col Richard E. Huffman, PhD (Member)	date
_____	_____
Maj Andrew J. Lofthouse, PhD (Member)	date

AFIT/GAE/ENY/11-M29

Abstract

The key to Direct Simulation Monte Carlo (DSMC) is decoupling of particle motion and particle collisions. Particles within each cell are randomly chosen as collision partners, and the collision is then accepted or rejected by comparing collision criteria to a random number. In the Smoothed Accept/Reject (SAR) algorithm, the accept/reject criteria is altered: rather than a binary function of rejection or acceptance, collisions can be partially accepted with a linear weighting between zero and one. The partial acceptance is based on a band around the original accept/reject criteria defined as a percentage of the collision criteria, which is called ϵ. The weighting is used in sampling the particles in order to calculate the macroscopic flowfield parameters. Previous work included comparisons to experimental data using inverse shock thickness, the results of which implied a relationship for the appropriate value of ϵ as a function of Mach number, and this is explored in the present work. Additionally, 2-dimensional experimental data is used for comparison between SAR and the original algorithm. Velocity distributions of the particles are examined for all algorithms and compared to experimental data to determine the effect of the SAR algorithm at a microscopic level. Both of the 1-dimensional comparisons to experiment shows that SAR provides results that best matches the experimental data. All of the comparisons to experiment show a Mach dependency that has previously been noted, and the dependency was defined for the normal shock simulations. DSMC does adequately simulate the nonequilibrium within the cells at a high Mach number through the shock, but SAR does. The SAR algorithm models the flowfield in the shock better than DSMC through a change in the collision rate and particle sampling methods, which allows for a more accurate simulation.

Acknowledgements

First and foremost I would like to thank my family and friends that have supported me along my journey throughout my life. My parents have always loved me and supported me, and hopefully I can make them proud. My brother, who definitely got the smart genes as well as the tall genes, has been a constant source of computer advice and encouragement. My grandparents, who are no longer with us, always provided us with a place we could call home no matter where we were living at the time and helped me grow to be the person I am. The amount of love and pride they had for their children and grandchildren is immeasurable and will never be forgotten. To my friends here at AFIT, we've spent many a long night in the Linux lab, and you guys helped me make it through! Dave Doak has been a lifesaver in the Linux lab, and helped us in anyway he could. Without his assistance in the Linux lab none of us would have accomplished as much as we have. My advisor, Dr Greendyke provided wisdom and insight, and I learned a great deal working with him over the past year and a half.

Sarah E. Summers

Table of Contents

List of Figures

List of Tables

List of Symbols

List of Abbreviations

Improved Collision Modeling for Direct Simulation Monte Carlo Methods

I. Introduction

1.1 Motivation

The United States Air Force (USAF) has twelve core functions that are integral to its role in the defense of our nation. Of these twelve functions, hypersonics plays a direct role in five: nuclear deterrence operations, air superiority, space superiority, global precision attack, and rapid global mobility. The ability to understand hypersonic flows and apply the research to the design of hypersonic vehicles increases access to space and allows a greater range and response time of air and space vehicles throughout the world. Recently, the new report on Technology Horizons by Dr. Werner Dahm, the Chief Scientist of the Air Force [2], emphasized important future capabilities that depend on hypersonics research, including prompt strike systems that would cruise at Mach 6 and a two-stage-to-orbit reusable space launch vehicle, both of which will fly through a rarefied atmosphere. Therefore, it is imperative for the Air Force to accurately model and predict the behavior of these vehicles within the rarefied hypersonic regime.

At higher altitudes, starting around 100 km [3], the air is less dense and therefore the Knudsen number (Kn) is higher. The Knudsen number is a measure of the rarefaction of a gas, and will be explained more thoroughly in the following chapter. Continuum solvers that use Navier-Stokes or Euler equations cannot accurately predict the gas behavior in high Knudsen number regimes. Figure 1.1 illustrates the Knudsen number limits for the continuum solvers.

Euler based solvers are used in the inviscid limit (when viscosity is at or very near zero) while Navier-Stokes based solvers can be used for a simulation with a Knudsen number of less than 0.1. The continuum assumption breaks down at about

1
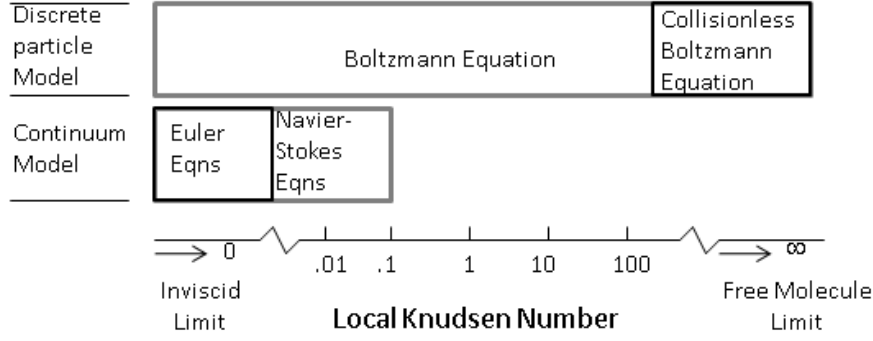
Figure 1.1:   Knudsen Number Limits on Mathematical Models [4]

Kn=0.1, and the flow can be considered rarefied above that value. Direct Simulation Monte Carlo (DSMC) is a stochastic method which utilizes the Monte Carlo statistical model to simulate gas behavior, which is very useful for these rarefied atmosphere hypersonic simulations, and has been used for this purpose for decades. Notably, DSMC has been used for simulations of the space shuttle reentry [3,5]. DSMC has also compared well to many wind tunnel tests, which have been used to enhance understanding of hypersonic flows [6,7]. Additionally, DSMC has been heavily used in the study of microflows [7]. DSMC will be explained in more detail in Chapter 2.

There are two other methods which are used to predict behavior in a rarefied condition. The first is molecular dynamics (MD), which is a direct simulation of each particle, and therefore has generally been limited to nanoscale simulations [8]. MD is more computationally expensive than DSMC, but there has been research to improve the computational efficiency of MD in the last couple of years so MD can be used more in dilute gas simulations [8]. MD is a deterministic simulation of the system whereas DSMC is a statistical model of the system, which requires simulated particles representing a large number of real particles in order to get accurate results. The methodology of DSMC makes it more computationally efficient compared to MD, even though results of DSMC are very similar to MD. The other method is direct numerical simulation, generally referred as a Boltzmann solver. Boltzmann solvers are also computationally expensive, but they can be coupled with continuum

solvers to reduce computational cost in cells that have a low local Knudsen number [9]. Therefore DSMC is a just as accurate, but more cost effective method for hypersonic method simulations.

There are, however, some problems with the original DSMC algorithm within areas of nonequilibrium such as shocks and boundary layers. The collision rate is not high enough to allow for proper equilibration compared to experimental data. A few collision models, one of which is discussed in more detail in Chapter 2, were created in order to better simualte the flow in nonequilibrium conditions. These methods change the collision rate, and also alter the transport properties, which only occur in nonequilibrium. The simple code that this project uses has one method to correct the problem, but there are more methods that have been developed over the years. The scope of this project is not to evaluate the newer collision models, but to investigate a new accept/reject method that may correct DSMC in another manner.

Over the past 3 years, a modified DSMC algorithm known as Smooth Accept/Reject (SAR) was developed by Greendyke et al [10] that may give more accurate results. The previous research investigated a potential method that would reduce the convergence time for DSMC simulations. The research showed that convergence was not effected by SAR, but the flowfield results were different. The previous work also showed that DSMC is not always accurate at higher Mach numbers. A one dimensional DSMC shock program predicts a thicker normal shock wave when comparing to experimental data [10, 11] for velocities above Mach 3. Further discussion of the previous work can be found in the next chapter.

The purpose of this thesis is to further refine the technique used in the SAR modification and to better understand why SAR produces the results that have been seen thus far. The new technique, once understood and applied, can be used for development of aircraft that operate within the rarefied regime at hypersonic velocities. The methodology of the project includes comparison of the new algorithm's results to experiment and theoretically understanding the effects of the algorithm.

Additionally, the velocity distribution of specified cells will be compared to the speed distribution, as derived from the Maxwellian Distribution. Mach dependency will also be investigated, as a proportional relationship has been noted in previous studies [11].

II. Background

In order to have an understanding of the project, one must first understand the derivation and application of the Boltzmann equation. The Boltzmann equation can be used to calculate gas flow in any condition, incuding in rarefied and nonequilibrium conditions. Rarefaction will be further discussed in Section 2.2. Nonequilibrium can be defined as a perturbation from an equilibrium condition, and when the departure from equilibrium is large, the conservation equations which were derived using a small perturbation from equilibrium are incomplete. The moments of the Boltzmann equation, which are found by multiplying the Boltzmann equation by a function of velocity and integrating over velocity space, must be applied in order to fully describe the fluid flow in nonequilibrium [12]. The Boltzmann equation must then be simulated in order to calculate the flowfield, which can be done using DSMC. DSMC uses statistical modeling to predict the collisional behavior of a gas using a Monte Carlo scheme and then calculating the expected motion through the use gas kinetics. DSMC requires knowledge of kinetic theory, therefore the next two sections will include a description of both the Boltzmann equation and the associated kinetic theory before DSMC is explained.

2.1   The Boltzmann Equation and Statistical Mechanics

The Boltzmann equation "describes the rate of change, with respect to position and time, of the distribution function." [12] The distribution function being discussed is the velocity distribution function of the particles within the system. In otherwords, the Boltzmann equation describes the molecular motion of a system, which can be used to determine the overall behavior of that system. Molecular motion can be described using velocity space; particles can occupy velocity space just as they occupy physical space. Just as a particle has a position in physical space that can be described with coordinates in a reference frame, a particle in velocity space can be described in a coordinate system. The velocity element that the particles reside in can be defined as: $c_1 + dc_1, c_2 + dc_2, c_3 + dc_3$, where c_1, c_2, and c_3 represent the three dimensional

components of the particle's velocity. The number of particles within the element can be found by:

$$dN = Nf(c)dc_1dc_2dc_3 \tag{2.1}$$

where N refers to the total number of particles, and f(c) refers to the velocity function. Just as a spatial volume can be defined by multiplying the three dimensions of elements that make up the volume, $dV_x \equiv dx_1dx_2dx_3$, the volume in velocity space is: $dV_c \equiv dc_1dc_2dc_3$ [12]. The Boltzmann equation can be derived by examining molecules of a particular velocity class, c_i, within a volume in physical space and a volume within velocity space. A velocity class refers to a group of particles occupying the same velocity element. The Boltzmann Equation accounts for the complete behavior of the particle within the velocity class: [12]:

$$\frac{\delta[nf(c_i)]}{\delta t} + c_j\frac{\delta[nf(c_i)]}{\delta x_j} + \frac{\delta[F_jnf(c_i)]}{\delta c_j} = \left[\frac{\delta[nf(c_i)]}{\delta t}\right]_{coll} \tag{2.2}$$

Where δt is the change in time, n is the number density, δx_j is the change in position, δc_j is change in velocity, and $f(c_i)$ is the velocity function. The first term in Equation 2.2 is the convection term, the second term is the flux of molecules across the surfaces of the volume, the third term represents flux of molecules into the velocity volume due to external forces such as gravity, and the right hand side of the equation is the collision integral, which represents the rate of change in the number of molecules in the velocity class due to collisions. The convection term simply refers to the movement of the particles through the system. The flux of molecules accounts for an open system where particles are moving in and out of the domain. The right hand side of the equation, known as the collision integral, is what makes the Boltzmann equation so difficult to solve analytically. The computations are very expensive, and only very simple geometries with a fairly small domain have been solved using a direct Boltzmann solver. The collision integral requires knowledge of the velocity states of the particles before and after collision in order to be calculated [13], which can be done using kinetic theory and statistical mechanics.

The collision integral describes the rate of collisions between two particles belonging to different velocity classes at a certain point on the sphere of influence as referenced from the velocity vector and the line of centers. The sphere of influence refers to the spherical distance at which a particle will begin to effect another particle. If intermolecular forces are being neglected, the sphere of influence is the radius of the particle, but the sphere of influence will be larger if intermolecular forces are being considered. For the purpose of this discussion, sphere of influence could refer generically to either of these definitions. Line of centers refers to a line that can be drawn by connecting the center of the two colliding particles. The two colliding particles belong to different velocity classes, which are called c and ζ. These particles will collide and change velocity classes due to the collision, while other particles will have collisions that cause them to enter into the two velocity classes. These two types of collisions are referred to as depleting and replenishing collisions, respectively. The collision term can now be expressed as the integral of the velocity functions over the volume of the sphere of influence of the ζ particles:

$$\left[\frac{\delta[nf(c_i)]}{\delta t}\right]_{coll} = \int\limits_{-\infty}^{\infty}\int\limits_{0}^{2\pi}\int\limits_{0}^{\pi/2} n^2[f(c_i')f(\zeta_i') - f(c_i)f(\zeta_i)]gd^2 sin\psi cos\psi d\psi d\epsilon dV_\zeta \quad (2.3)$$

where c_i' and ζ_i' replenish the velocities while c_i and ζ_i deplete the velocity classes, g is the relative velocity between the particles, d is the radius of the sphere of influence of the particle, n is the number density, and ϵ and ψ represent angles that define the location of the collision on the sphere of influence. The principle of reciprocity is an assumption that for every collision that depletes from a velocity class, there is a collision that replenishes from another velocity class. The principle holds true for equilibrium cases only. Therefore, in equilibrium the collision integral equals zero, which means the integral only matters for nonequilibrium conditions, such as shocks or boundary layers where gradients are large [12].

As stated before, nonequilibrium can be expressed as a perturbation away from equilibrium, and occurs in two areas of the flowfield: shock layers and boundary layers,

both of which happen in hypersonics. In equilibrium, particles in a system can be distributed into energy states according to the Boltzmann Distribution Function [12]:

$$N_j^* = \frac{NC_j e^{\frac{-\epsilon_j}{kT}}}{\sum_j C_j e^{\frac{-\epsilon_j}{kT}}} \tag{2.4}$$

where N is the number of particles, N_j^* is the number of j macrostates, C_j is the number of increments, or degeneracy, k is the Boltzmann constant, T is the temperature, and ϵ_j is the energy. The Boltzmann Distribution Function is the ratio of particles at a given energy level over the sum of possible energy levels. At any given time, the particles may not be distributed according to the Boltzmann Distribution, but the particles spend the majority of the time distributed around it. In nonequilibrium, particles are not distributed around the Boltzmann Distribution. The energy states are associated with the macroscopic properties of the system; the macroscopic properties are known as long as the temperature and the partition function are known. The partition function (Q) describes how the energy is partitioned across the energy states, and is defined as [12]:

$$Q = \sum_j C_j e^{\frac{-\epsilon_j}{kT}} \tag{2.5}$$

A particle can store energy in different ways: as translational energy, rotational energy, vibrational energy, or electronic energy. Each type of energy storage will have its own distributon function associated with it. When particles go through a shock wave, the particles' higher energy modes are activated, and through collisions the particles return to a new equilibrium state. The rate at which particles return to equilibrium is called the relaxation rate [12], and each type of energy storage will have its own relaxation rate dependent on types of collisions required for reequilibration. Kinetic theory is therefore important to discuss in order to fully understand the behavior of the gases through molecular collisions.

There are a few assumptions that go into the derivation of the Boltzmann equation that must be discussed before moving on. The density is considered low enough

that only binary collisions occur and intermolecular forces are negligible [13]. In other words, there are so few particles in the volume that the likelihood of three molecules being at the same place at the same time in order to cause a tertiary collision is highly unlikely. Additionally, since there are so few particles, a particle's path will not be altered simply by being affected by another molecule's presence unless a collision takes place. Another assumption is that of molecular chaos, which means that the velocities of two colliding particles are not correlated and are independent of position. Boltzmann referred to the molecular chaos assumption as "stosszahlansatz." These assumptions are common with DSMC methodology.

2.2 Kinetic Theory

Rarefied conditions have been mentioned in the previous sections, but not yet defined. The degree of rarefaction of a gas is expressed in terms of the Knudsen number [4]:

$$Kn = \frac{\lambda}{L} \tag{2.6}$$

where λ is the mean free path is the distance between molecular collisions, and L is a characteristic length associated with the system. The more rarefied the gas is, the less likely it is that particles will collide. The mean free path will be larger, which means that particles will travel a longer distance before colliding, which is the mechanism particles use to equilibrate. Therefore, particles will not be in equilibrium with the other particles in the flowfield for longer. As a particle moves through space, it sweeps out a volume per unit time which is $\pi d^2 \overline{C}$ [12]. The number of collisions per unit time (θ) is given by:

$$\theta = \pi d^2 \overline{C} n \tag{2.7}$$

where d is the diameter of the particle, $\overline{C}$ is the average molecular velocity. Using the above equation, the mean free path is:

$$\lambda = \frac{\overline{C}}{\Theta} = \frac{1}{\pi d^2 n} \tag{2.8}$$

9

Additionally, the number of collisions per volume (N_c) is [4]:

$$N_c = \frac{1}{2}n^2\overline{\sigma_T c_r} \qquad (2.9)$$

Where σ_T is the collision cross-section and c_r is the relative velocity between particles. The characteristic length used to find a local Knudsen number can be defined as [4]:

$$L = \frac{\rho}{d\rho/dx} \qquad (2.10)$$

A high Knudsen number indicates that the mean free path is near the same magnitude as the characteristic length, which is a condition that occurs at high altitudes when the density is low or if an incredibly small characteristic length is used, such as in nanoscale simulations.

Velocity functions were discussed in the preceeding description of the Boltzmann Equation, but have not yet been defined. The equilibrium velocity distribution is called the Maxwellian distribution:

$$f(C_i) = \left(\frac{m}{2\pi kT}\right)^{\frac{3}{2}} e^{-\frac{m}{2kT}(C_1^2+C_2^2+C_3^2)} \qquad (2.11)$$

where m is the mass of the particle, k is the Boltzmann constant, T is the temperature, and C is the particle thermal velocity broken into its 3 components [12]. The magnitude of the velocity can be investigated using the speed distribution, which is derived from the Maxwellian distribution [12]:

$$\chi(C) = 4\pi \left(\frac{m}{2\pi kT}\right)^{\frac{3}{2}} C^2 e^{-\frac{m}{2kT}C^2} \qquad (2.12)$$

The speed distribution ($\chi(C)$) is written for a gas with no bulk motion, which is not true for the computational cases in this thesis. A method to adapt the speed equation for use in hypersonic and supersonic flows has been developed, and will be discussed in Chapter 3. The most probable thermal velocity is derived from the speed equation

and is defined as:

$$C_{mp} = \sqrt{\frac{2kT}{m}} \tag{2.13}$$

The most probable thermal velocity (C_{mp}) is the velocity that the particles are most likely to have given the temperature of the system. The C_{mp} should not be confused with the average velocity, as they are not the same.

2.3 Direct Simulation

Now that the theoretical background that forms a basis for DSMC has been investigated, DSMC itself can be discussed. DSMC is a stochastic model that simulates a flowfeld using the Monte Carlo statistical method, and is primarily used for rarefied gas simulations and nanoscale simulations. The Monte Carlo method is used to determine if a collision occurs. Once the collision is accepted, kinetic theory is used to calculate the collision behavior of the particles. There are a few molecular models used to describe particle collisions that have been implemented in DSMC. The most basic is the hard sphere (HS) model, which is known as the "billiard ball" model. In the HS model, intermolecular forces are neglected, and it is assumed that molecules only interact with each other by physically colliding. In other models, such as the Sutherland model, that take intermolecular forces into account, molecules can interact simply by being within a certain radius of each other. The Sutherland model adds weak atractive forces before the molecules contact [12]. Neither Sutherlands nor HS demonstrate reality. Molecules actually display an attractive force until they get within a certain distance of each other, at which point the force becomes repulsive. The repulsive force increases as the distance between the particles decreases, and force will eventually become infinitely strong [12]. An improvement on the HS model is the variable hard sphere (VHS) model, which is used primarily thoughout this project. The VHS model varies the diameter, and therefore the collision cross-section of the particles based on the velocity of the particle, and will be further discussed in another section.

The process of DSMC is fairly simple, and is based on an assumption that the motion and collision of particles are decoupled. The assumption allows the algorithm to collide particles and then separately move the particles, which will be explained in further detail when DSMC assumptions are discussed. The DSMC algorithm uses a small time scale, usually on the order of the mean free time, which is the time between molecular collisions. This small time scale, usually on the order of 10^{-6} seconds, and a small cell size allow the algorithm to decouple the particle motion and particle collision processes. The DSMC program progresses through a basic set processes for a specified number of time steps. The process begins by moving particles on the velocity vector of each particle. The number of collisions (P) are then calculated using the probability equation:

$$P = \frac{F_N \sigma_T c_r \Delta t}{V_c} \tag{2.14}$$

where F_N is the ratio of actual particles per simulated particle, σ_T is the collision cross-section, c_r is the relative velocity, Δt is the change in time, and V_c is the volume of the computational space, which for the purposes of this equation is the cell volume. Next, a randomly selected pair of particles from a cell are chosen and the following ratio is calculated and compared to a randomly selected number:

$$\frac{\sigma_T c_r}{(\sigma_T c_r)_{max}} > Ran \tag{2.15}$$

If the randomly selected number is larger than the ratio, the particles do not collide. If the randomly selected number is smaller than the ratio, the particles do collide. The pair selection and comparison repeats for the calculated number of collisions in the cell for all cells in the domain. All the particles are then moved based on their new velocity vectors (if collided) or the same velocity vector (if not collided) and the process is repeated until the flowfield reaches a steady state.

A few notes to make about the above process before moving on: the cell size must be on the order of the mean free path or smaller in order to properly decouple the movement and collision process, which can be verified by making sure that each particle only collides once per step. If a cell size is on the order of the mean free path and the time step is on the order of the mean free time, then a particle should only collide once per time step. If the particles do collide more than once per step, the assumption of decoupling is no longer valid, and either the cell size or time step will need to be reduced. In particular, one should look at particles in the stagnation region and shock layer (if one exists for the particular flowfield) since that will be the most dense area of the flowfield and is the limiting factor when designing a simulation. The ratio of simulated particles to real particles can also be increased to avoid more than one collision per particle per time step. Additionally, because of the nature of this statistical simulation, if there are not enough simulated particles in a cell the variance can be quite large. If a flowfield is too rarified, the time steps or cell size can be increased, or the ratio of simulated particles to real particles can be decreased.

Bird made a few key assumptions when he developed DSMC [4]. The first is local equilibrium in each cell. A flow through a shock is not in equilibrium, and it takes a number of collisions after the shock to requilibrate. Additionally, flows within a boundary layer are not in equilibrium. When there is a gradient present in the flowfield, there will be areas of nonequilibrium. A shock layer is an area between two different equilibrium states, and there will be a gradient present between the states. Boundary layers exist because the velocity at a wall is zero, so a gradient between the wall and the freestream develops. The flows in this research contain both shock layers and boundary layers and therefore are at nonequilibrium. Bird makes the assumption that if a cell size is roughly the mean free path or smaller, the particles within each cell are in local thermodynamic equilibrium. Bird uses the following equation to calculate the mean free path using the collision frequency [4]:

$$\lambda = \frac{\overline{c'}}{\nu} = \left[n \left(\frac{\overline{\sigma_T c_r}}{\overline{c'}} \right) \right]^{-1} \tag{2.16}$$

13

Where $\overline{c'}$ is the mean thermal speed of the particle, ν is the collision frequency, and n is the number density. Essentially, there are so few particles in a small enough space that they can collide with each other and stay in equilibrium even if the flowfield itself is not in equilibrium. These cells create a piecewise equilibrium where the particles within the cell are in equilibrium, but the particles are not in equilibrium with the particles in neighboring cells. Therefore, on a macroscale the flowfield is not in equilibrium even though on a microscale the particles are in equilibrium with the particles in their immediate vicinity. Another assumption made by Bird is within a cell particle collisions are not a function of location. In other words, if a cell is small enough, one does not need to know where the particle is within the cell in order to decide if it can collide with another particle within the cell. Since the collisions within the cells are not a function of location, Boltzmann's assumption of molecular chaos is satisfied. The assumption of molecular chaos simply means colliding particles are independent of position. Additionally, the two random selections during the collision process satisfy the molecular chaos assumption that is required with the Boltzmann equation [4]. Another significant assumption of DSMC is that every simulated particle represents many real particles, usually around 10^{13}, which not only allows DSMC to be computationally tractable but also provides the sampling pool of particles required for the statistical model. Given a small enough cell size, the first two assumptions are reasonable. In conditions such as a high Mach number flow over a body, the assumption that so many particles have the exact same characteristics may not be an accurate assumption [14]. This last assumption will be explored further as the results of the project are discussed in Chapter 4.

2.4 Variable Hard Sphere

As discussed previously, intermolecular forces are neglected in the HS model, and the model is not realistic. The inverse power law accounts for the change in intermolecular forces as a function of distance between particles, but it is also computationally expensive [15, 16]. The VHS model is a combination of the inverse power

law and HS models. The VHS model uses an inverse function to relate the temperature and the average cross-section of the particle. Therefore, just as the name implies, a hard sphere is still modeled, but the sphere changes cross-section according to the relationship [15]:

$$\overline{\sigma} \propto T^{-\zeta} \tag{2.17}$$

where T is temperature and ζ is an exponent that is unique to the particular gas being examined and is related to the viscosity index by:

$$\omega = 1/2 + \zeta \tag{2.18}$$

where ω is the viscosity index. The viscosity index for the gases used in this project can be found in Bird [4]. Equation 2.17 shows that as temperature increases, the collision cross-section will increase on average. Bird uses a reference diameter at a corresponding reference temperature to calculate the diameter of the particle:

$$d = d_{ref} \left(\frac{(\frac{2kT_{ref}}{m_r c_r^2})^{\omega - \frac{1}{2}}}{\Gamma(\frac{5}{2} - \omega)} \right)^{\frac{1}{2}} \tag{2.19}$$

where d_{ref} has been defined in multiple references [4,16], and m_r is the reduced mass, which is defined as:

$$m_r = \frac{m_A m_B}{m_A + m_B} \tag{2.20}$$

where m_A and m_B are masses of two colliding particles. The gamma function from Equation 2.19 is defined as:

$$\Gamma(j) = \int_0^\infty x^{j-1} e^{-x} dx \tag{2.21}$$

As one can see in Equation 2.19, the diameter is dependent on the relative velocity, and the other values should remain fixed for a given particle. As a particle's velocity increases, the diameter (and therefore collision cross-section) also increase. The SAR procedure, which will be fully defined in the next chapter, also has a velocity depen-

dency. Bird has proven that the VHS model applied in a DSMC simulation compares well to experiment with a normal shock wave with M=2, but at higher Mach numbers DSMC does not compare as well to experimental data [11]. Therefore a question that must be asked is whether SAR could be used rather than or in addition to VHS to give accurate results for higher Mach flows.

2.5 Experimental Data

Two experiments are used for comparison in this project. The first is a 1-dimensional normal shock, and the second is the 2-dimensional axisymmetric hollow cylinder with a step. These experiments are detailed in this section, and in the following chapter the simulations used for comparison will be described.

2.5.1 1-Dimensional Normal Shock.
Alsmeyer performed experiments measuring the density distribution of Argon and Nitrogen across a normal shock wave for Mach numbers between 1.55 and 9 [1]. A stainless-steel shock tube was used for the experiment with an inner diameter of 150 mm. The density measurements were taken by measuring the attenuation of an electron beam which was generated by a commercial electron gun and collected by a Faraday cage. Once the data was collected, Alsmeyer plotted the normalized density profile across the shock and the inverse shock thickness. The density was normalized by [1]:

$$\rho_n = \frac{\rho - \rho_1}{\rho_2 - \rho_1} \tag{2.22}$$

where ρ is the measured density at a point, ρ_1 is the density before the shock, and ρ_2 is the density after the shock. The normalization allows for comparison to Alsmeyer's data regardless of the initial density, which means that many different sets of experimental data can be evaluated with each other. The error of the normalized density is accurate within $\pm 1\%$, and the inverse shock thickness is believed to be accurate to $\pm 4\%$.
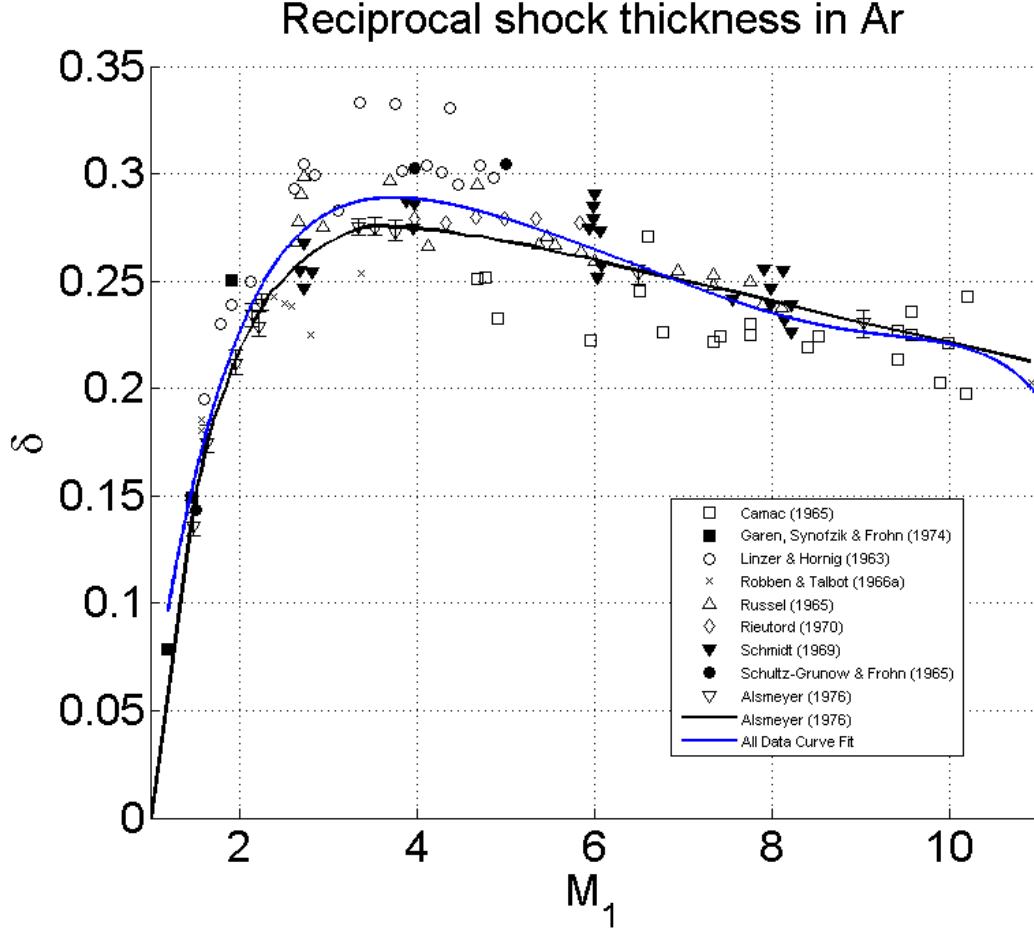
Figure 2.1:   Inverse Shock Thickness with Argon [1]

Figure 2.1 shows a range of inverse shock thicknesses at each Mach number, which were created by nine different researchers. Alsmeyer compiled the experimental data and used it as a reference in Ref [1]. The black line is the curve fit of Alsmeyer's data, and the blue curve fit is a 6th order curve fit of all the experimental data on the figure. The computational results will be comapred to the blue curve fit of all the data. The data shows that shock thickness initially thins quickly as Mach number increases until just past Mach 3, at which point the shock thickens at a much slower rate.

2.5.2   2-Dimensional Axisymmetric Hollow Cylinder.   Davis' experiment that is serving as a comparison is a 2d axisymmetric hollow cylinder with a step

[17]. The experiments used a heated nitrogen wind tunnel at the Imperial College in London in the 1970s [18]. The flow travels axially at approximately Mach=21 with a static temperature of 23K. Below is a schematic of the cylinder used in the experiment:
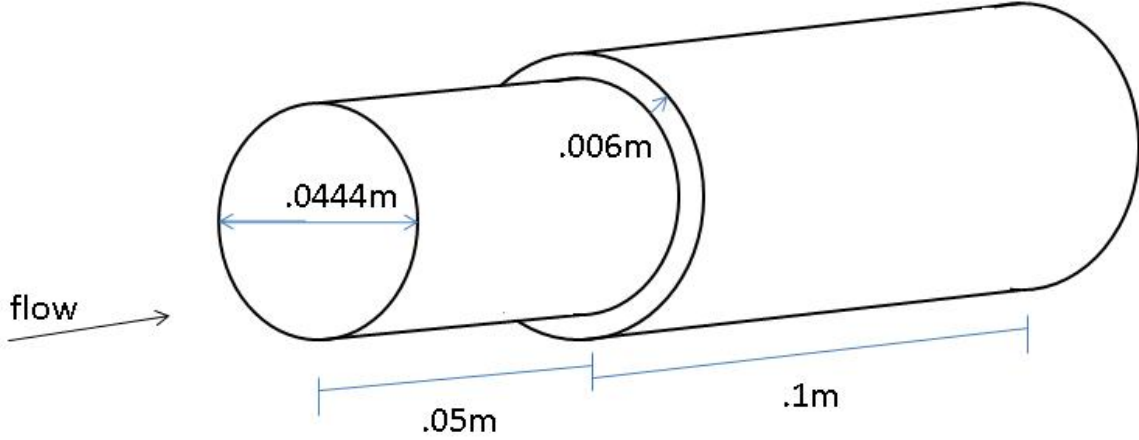
Figure 2.2:   Hollow Cylinder with a Step [17]

The air flows axially along the hollow cylinder and impacts the 6 mm tall step 50 mm from the leading edge of the cylinder. The initial radius of the cylinder is 444 mm, which becomes 456 mm after the step. The leading edge of the hollow cylinder is approximately 0.02 mm thick and has a 10° bevel in order to split the flow around the 1 mm thick cylinder [17]. The cylinder is constructed of a copper, cobalt, and zirconium alloy that has a high thermal conductivity in order to maintain the uniform wall temperature of 318K. The wall was not water cooled for the asymmetric testing as it was for other studies, but the wall temperature was measured [17]. The temperature measurement served as the wall temperature input for the computational study performed for this thesis. The density values were measured with an electron beam probe [17]. The nitrogen gas fluoresces when an electron probe fires electrons through the gas, and the intensity of the fluoresence is directly proportional to the density. The flouresence is photographed, and a microdensitometer, which measures the amount of blackness in a photograph, is used to quantitatively measure the fluoresence. Density profiles were created at five points along the cylinder: 18 mm before

the step, 3 mm before the step, at the step, 1 mm after the step, and 7 mm after the step. Davis' density profiles can be found in Figures 2.3 through 2.7.
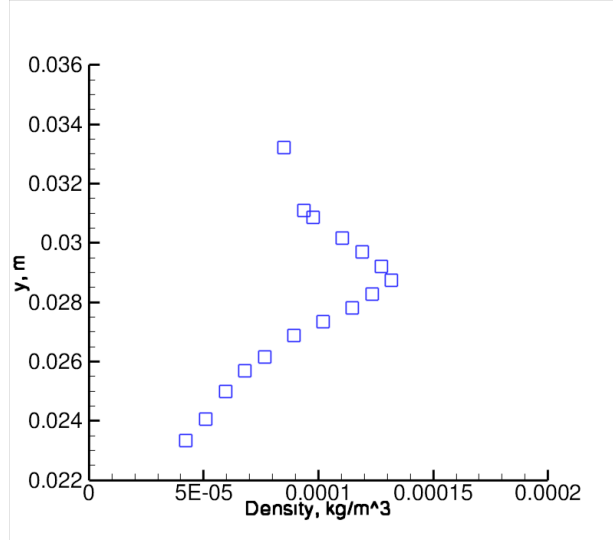
Figure 2.3:   Davis Density Profile at x=0.0313m [17]

In Figure 2.3, the profile data is taken .0187m upstream of the step. The change in density is due to a weak shock layer merging with the boundary layer.
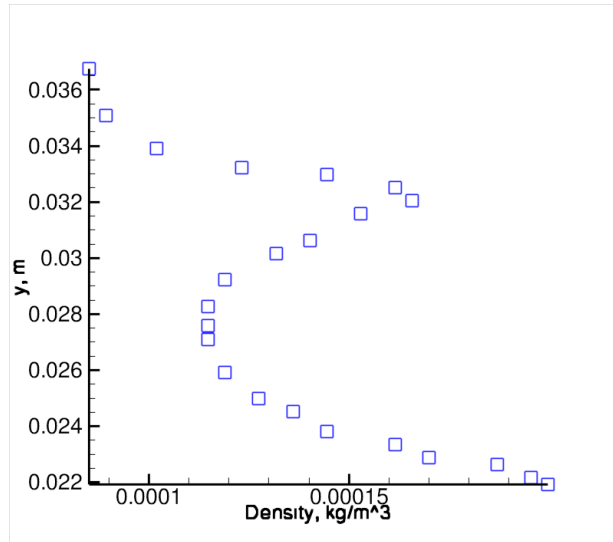
Figure 2.4:   Davis Density Profile at x=0.0462m [17]

The density profile in Figure 2.4 is taken 0.0038m upstream of the step. The increased density towards the wall is due to the stagnation layer. The density peak

19

is at approximately 0.032 m rather than 0.029 m in Figure 2.3, indicating a growing boundary layer as distance from the leading edge increases.
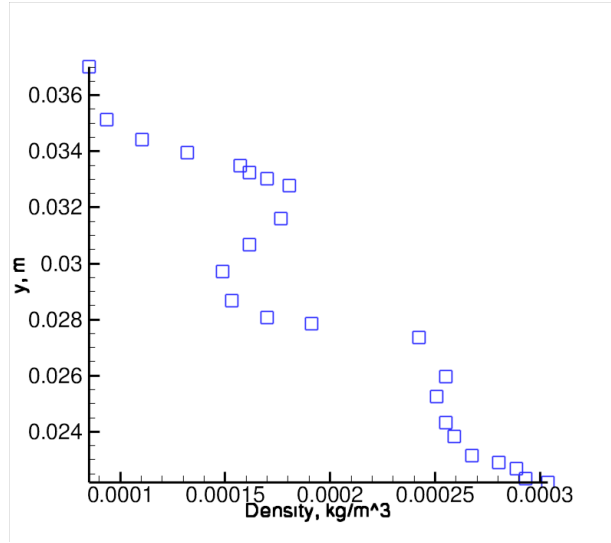
Figure 2.5:   Davis Density Profile at x=0.0495m [17]

Figure 2.5 shows the profile closest to the stagnation point and therefore it has the highest density value at the wall. A smaller peak at approximately y= 0.033 m shows the location of the shock layer at x=0.0495 m.
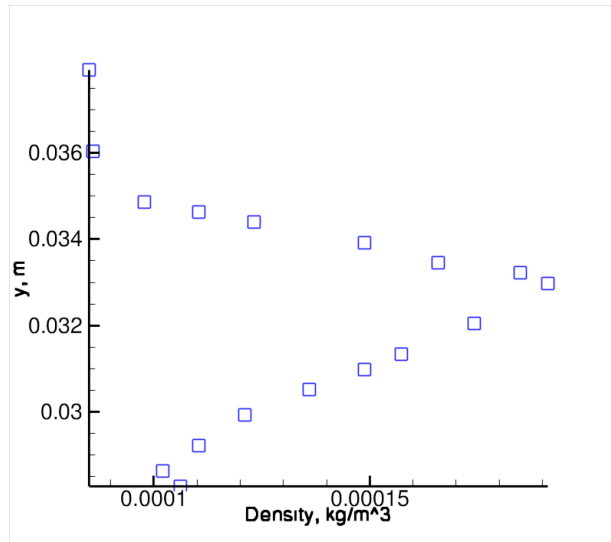
Figure 2.6:   Davis Density Profile at x=0.0509m [17]

Past the stagnation point, the density profile is similar to the first profile at x=0.0313 m. The change in density is larger, as the shock is stronger after the step. However, both of the profiles at x=0.0509 m and 0.0561 m show an increase in density close to the wall, at approximately y=0.0305 m.
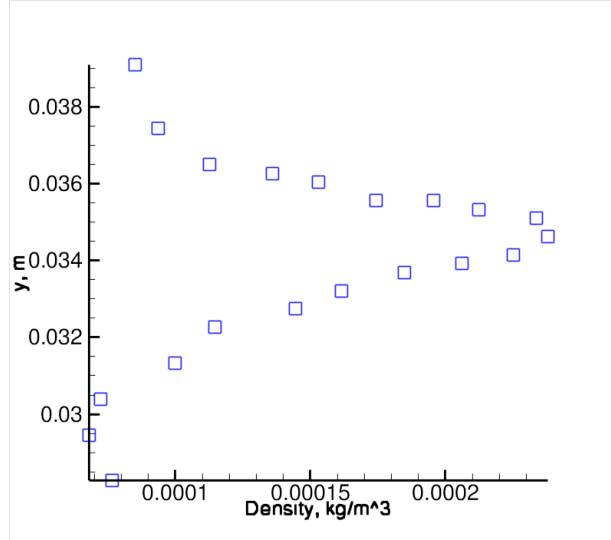
Figure 2.7:   Davis Density Profile at x=0.0561m [17]

The shock is stronger 6 mm downstream from the step compared to Figure 2.6, as shown by the change in density at x=0.0561 m in Figure 2.7.

2.6   Velocity Distributions

The velocity distributions across a shock wave at Mach 7.18 were derived from experimental data by Holtz and Muntz [19]. An electron beam flourescence technique was used, just as with the other experiments discussed in this project. In order to adequately resolve the regions in the flowfield, a Fabry-Perot etalon was implemented in the observations [19]. The Fabry-Perot etalon acts as a filter and only allows certain emission frequencies to be evaluated. The relative velocity between the sensor and the molecules are calculated using the equation [19]:

$$\frac{\Delta\lambda}{\lambda_0} = \frac{V}{c}$$

(2.23)

Where $\Delta\lambda$ is the wavelength shift due to molecular motion, λ_0 is the unshifted wavelength of fluorescence, V is the relative velocity, and c is the velocity of light [19]. The sampling locations are identified by a normalized density value so that the data may be compared to other experiments and computational results [19]:

$$\hat{n} = \frac{n - n_1}{n_2 - n_1} \tag{2.24}$$

where $\hat{n}$ is the normalized number density, n is the number density at the location, n_1 is the upstream number density, and n_2 is the downstream number density. These techniques are accurate within $\pm 4\%$ [19]. Holtz and Muntz take data at multiple points throughout the shock, but three points were chosen to use as a comparison for this project: $\hat{n} = .24$, $\hat{n} = .333$, and $\hat{n} = .542$. These points were chosen based on the changes occuring as the large number of particles traveling at the upstream velocity collide with other particles in the shock. After $\hat{n} = .542$, the distributions take on a fairly symmetric appearance and do not change significantly. The velocity distributions are normalized for ease of comparison. The velocity is divided by the upstream bulk velocity, and the y axis is normalized by the maximum velocity function so that the distributions all peak at unity. The distributions chosen for comparison in this project have been reproduced so that they can be plotted with the computational results.
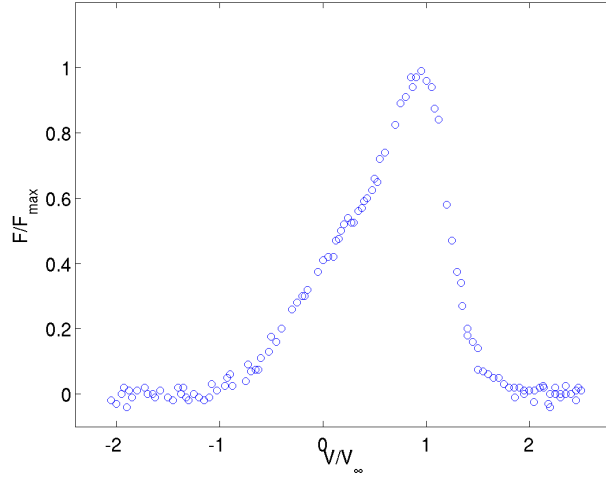
Figure 2.8:   Velocity Distribution at $\hat{n} = .24$ [19]

The distribution in Figure 2.8 shows that most of the particles are still at the bulk velocity, which is located at V/V_∞. These particles that are traveling at the bulk velocity have not collided with another particle in the shock layer, yet.
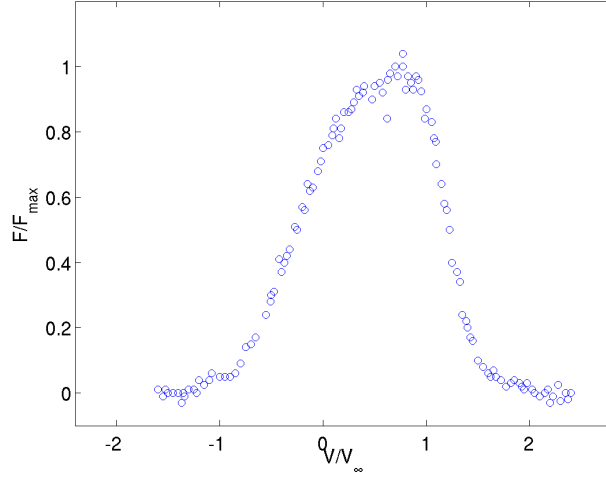
Figure 2.9:   Velocity Distribution at $\hat{n} = .333$ [19]

In Figure 2.9, the distribution is much wider and there is no longer a peak at the bulk velocity. The majority of particles have collided within the shock later and are traveling slower than the bulk velocity. The distribution is still slightly skewed

23

to the right and not symmetrical, indicating that there are still a number of particles that have not collided and are still traveling at the bulk velocity.
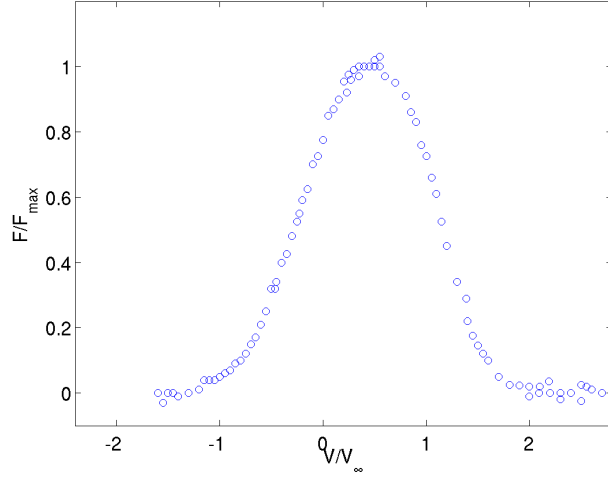
Figure 2.10:   Velocity Distribution at $\hat{n} = .542$ [19]

At the last sampling point within the shock, the distribution is very smooth and symmetrical, indicating that at a little over halfway through the shock layer the vast majority of particles have experienced a collision. The distributions before and after the shock, which are equilibrium distributions, should also be used for comparison.
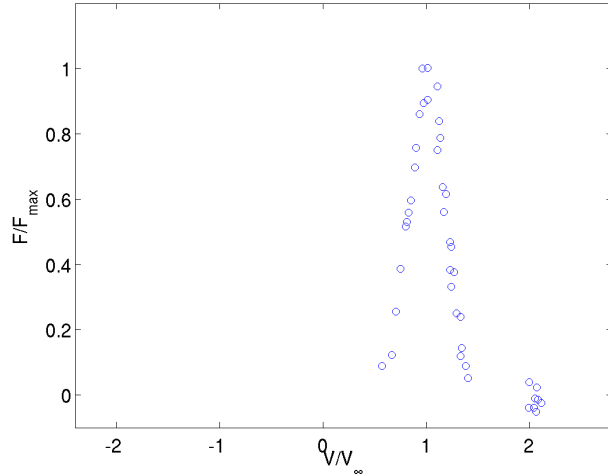
Figure 2.11:   Velocity Distribution Upstream of the Shock [19]

Upstream of the shock, the majority of the particles are at the bulk velocity, and the distribution is relatively thin. Since the majority of the particles are traveling straight from left to right at the bulk velocity, there are fewer collisions, which causes the tight concentration around the bulk velocity.
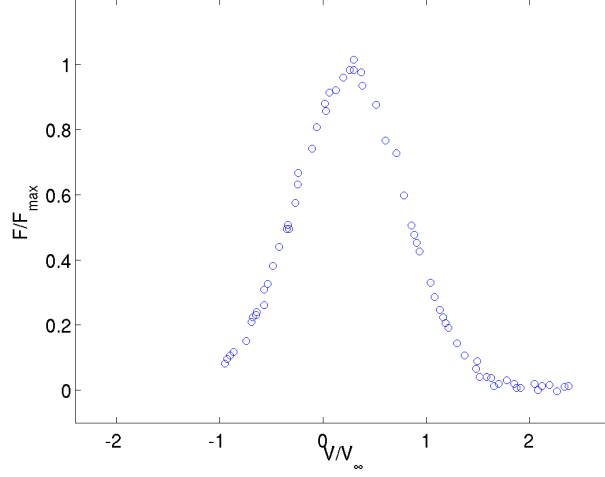
Figure 2.12:   Velocity Distribution Downstream of the Shock [19]

After the shock, the vast majority of the particles have collided and they have reached a new equilibrium state. The new bulk velocity is about half of the upstream bulk velocity. The distribution is wider, reflecting the fact that there is a large range of particle velocities after the shock due to collisions.

III.   Methodology

As stated in the introduction, the purpose of this project is to explore the applicability and usefulness of the SAR method. SAR will be fully defined in this chapter, and the computational experiments will be outlined. Additionally, another variation of the collision accept/reject criteria will be evaluated called No Accept/Reject(NoAR). As the name implies, there is no accept/reject criteria in NoAR: if a pair of particles is chosen to collide, then they are automatically accepted. A more detailed explanation of NoAR will be found in the next section.

The first experiment that must be done on these two new algorithms is the random walk test. Bird discusses in his book [4] that DSMC is a Markovian system, which means that the next time step is only dependent on the current time step. A random walk is a subset of the Markov chain, and will not conserve molecular quantities such as position, velocity, and internal energies. Random walks can occur in DSMC because the molecular quantities are conserved on the average and because of rounding that is inherent with any computer program [4]. Once SAR and NoAR have been proven to contain no more random walks than the original DSMC code, the rest of the experiments can begin.

The second experiment is the comparison to the 1-dimensional normal shock experiment by Alsmeyer [1] using Bird's 1-dimensional code, called DSMC1S [4]. Alsmeyer measured density and used the measurements to calculate the inverse shock thickness of the shockwave. The inverse shock thickness will be calculated at several Mach numbers ranging from 1.5 to 9, which will not only allow for comparison to experimental data, but also provide insight into the relationship between Mach number and ϵ.

The third is the comparison to the hypersonic flow over 2-dimensional axisymmetric cylinder with a step experiment that was performed by Davis [17]. Davis created density plots which can be compared to computational results using Bird's DSMC 2-dimensional axisymmetric (DSMC2A) code [4].

The fourth comparison uses velocity distributions created using data from both the DSMC2A and DSMC1S codes that can be compared to the velocity distributions from Holtz and Muntz. Additionally, velocity distributions at four different Mach numbers are compared to each other to understand the effects of Mach number on the velocity distributions.

Lastly HS simulations with SAR and NoAR are compare to the VHS simulations and the experimental data for the hollow cylinder and the normal shock. Since both SAR and VHS have Mach dependencies, it was decided for completeness to run HS couple with SAR.

3.1 SAR Method

The Smoothed Accept/Reject collision algorithm varies only slightly from that of the original DSMC algorithm by Bird [4, 10, 11]. The collision accept criteria becomes:

$$\frac{\sigma_T c_r}{(\sigma_T c_r)_{max}} \pm \frac{\epsilon}{2} \frac{\sigma_T c_r}{(\sigma_T c_r)_{max}} > Ran \tag{3.1}$$

where ϵ is a user determined percentage of the ratio of collision cross-section times relative velocity over the maximum product within the cell. Just as with Bird's code, if the random number is larger than the left side of Equation 3.1, the collision is rejected, and if the random number is smaller the collision is accepted. Unlike Bird's code, however, random numbers that are within the band of the ratio plus or minus $\frac{\epsilon}{2}$ are partially accepted and given a weighting between 0 and 1 that varies linearly. Additionally, particles that are fully accepted are given a weighting of 1 and rejected particles are given a weighting of zero [11]. These weightings are used to calculate the macroscopic flowfield properties. Only particles with a non-zero weighting are considered when sampling the flowfield, which was hoped to make the DSMC simulations converge faster [11], using the equation:

$$\overline{Q} = \frac{\Sigma_i w_i Q_i}{\Sigma_i w_i} \tag{3.2}$$

where Q_i is a flowfield parameter and w_i is the weighting. Note that density does not use the weighting scheme in order to conserve mass. The simulations did not converge faster, but variations in the flowfield were noted for further study [10]. The cases for this project include ϵ values of 0%, 25%, 50%, 75%, 100%, and 200%. The $\epsilon = 0\%$ case has the same accept/reject criteria as the original code and will only have weightings of zero and one because there will be no partially accepted collisions. The resulting flowfield therefore should be closest to the flowfield produced by Bird's code, but not necessarily identical because of the sampling differences associated with SAR compared to the original DSMC algorithm. As the ϵ value increases, the number of rejected and fully accepted particles will decrease while the number of partially accepted particles will increase [14]. In the NoAR code, if a pair of particles is selected to collide they are accepted and given a weighting of 1 [10]. Just as with SAR, only particles with a non-zero weighting are sampled in the NoAR algorithm, and particles that are not selected to collide have a weighting of zero. The NoAR algorithm was developed because it is the complete opposite of an orderly Markovian system with an accept/reject criteria. NoAR is an extreme case that higher ϵ values should tend toward. The 200% SAR case was selectively run to verify that the results do continue to tend toward NoAR. The expected results of the study are that Bird and NoAR produced flowfield results that are the extrema and the SAR results are in between, with lower ϵ values closer to Bird.

An illustration of the smoothed accept/reject concept is seen below:
The blue line in Figure 3.1 represents the $\frac{\epsilon}{2}$ limit and the green line is $-\frac{\epsilon}{2}$. The pink line is the original Accept/Reject criteria. Values in Equation 3.1 that compare less than the random number, value are fully accepted and would appear under the green curve and have a weighting of 1. The rejected particles that are above the random number would appear above the blue line and have a weighting of 0. The partially accepted particles would be between the green and blue lines and have a weighting between 0 and 1.
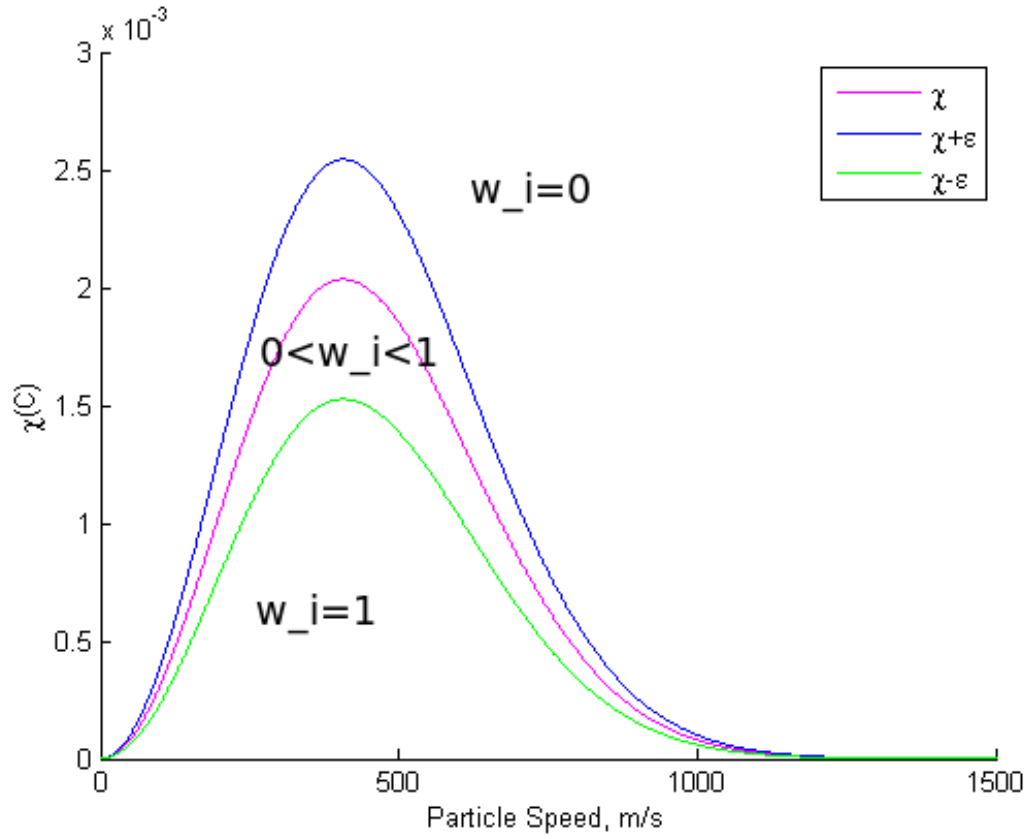
Figure 3.1:   SAR Illustration

During the previous work, a one-dimensional shock simulation was compared to experimental data using the original algorithm, SAR, and NoAR [10,11]. The results of the one-dimensional shock thickness experiment with Argon are shown in Figure 3.2 on the next page.
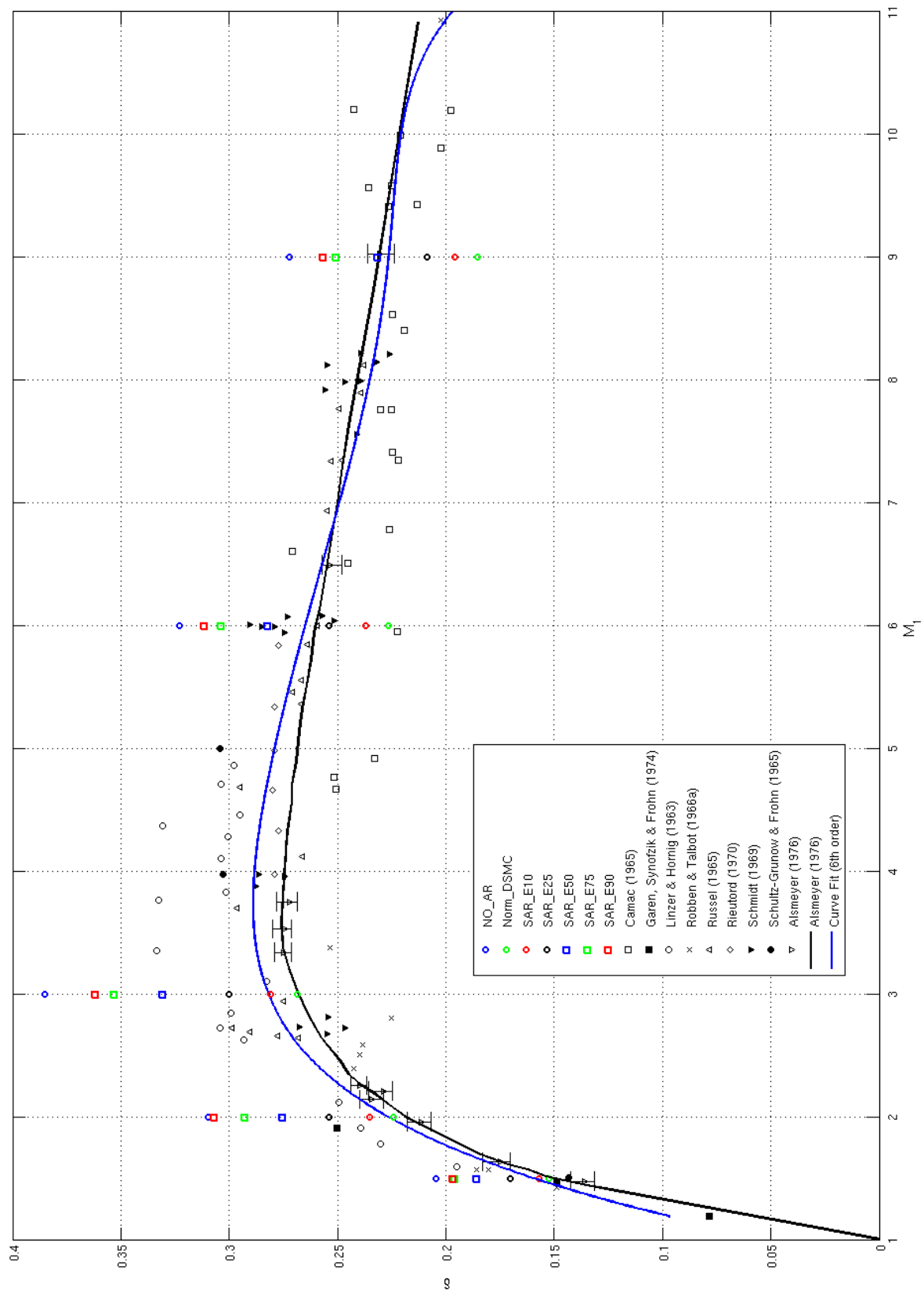
Figure 3.2:   1d Shock Thickness Comparison with Experimental Data

In the Figure 3.2, inverse shock thickness is shown as a function of Mach number. The black line is a curve fit of Alsmeyer's experimental data, and the blue line is the curve fit for all experimental data displayed on the graph. The figure also shows inverse shock thicknesses as calculated from the results of the original DSMC code, NoAR, and ϵ values of 10%, 25%, 50%, 75%, and 90%. The calculation for inverse shock thickness is explained in Section 3.3. The NoAR case results in a thinner shock for all cases, and the SAR results are in between Bird's and NoAR's results. As one can see, the results from Bird's original code becomes inaccurate above M=3, when Bird's code begins to predict a thicker shock compared to experimental results, but the SAR algorithm is able to match the experimental data. As the Mach number increases, a higher ϵ value is required to agree with experimental data, which is a result that requires more study as described in Section 3.3.

3.2 Random Walk Testing

In DSMC, the macroscopic values are stored as an average value of all the particles in the cell [4]. Using average values can lead to random walks in the Markovian system. A Markovian system is one in which the event at the next step is stochastically generated based on the event at the current time step without information from any previous steps [20]. Random walks can be tested, as Bird did, by simulating a closed system where particles are allowed to collide with each other and the walls as described in 10.4 of Ref [4]. The kinetic energy of the system is monitored for consistency over a number of time steps. If there is a significant change in kinetic energy, random walks are occuring and conservation of energy is not maintained. If kinetic energy remains nearly the same (one needs to account for changes due to round-off errors associated with repeating a process many times), random walks are not occurring in the program. The particular test for this project used 400,000 particles that were allowed to collide for 1,000 sample steps. The kinetic energy and the variance of the kinetic energy are used for comparison between the algorithms and to verify that the random walks are at a minimum.

3.3   1-Dimensional Shock Thickness

In addition to the new work as described later in this chapter, the 1d shock thickness comparison was reaccomplished, partially to verify that the same trends are seen and partially to see what additional information can be garnered from the comparison. The same 1d shock algorithms used for the speed distribution comparisons are used for the shock thickness plots. The programs are used with Mach numbers 1.5, 2, 3, 6, and 9. The resulting shock thickness for each Mach number is then graphically compared to Alsmeyer's data [1].

The inputs into DSMC1S for the project are an initial temperature of 293K, a number density of 10^{19}, and the ratio of simulated particles to real particles is $0.4 * 10^{16}$. The time step is set at $0.75 * 10^{-6}$ seconds and the cell size is 2 mm with a computational domain length of 0.6 m. The project compares to Alsmeyer's argon experiment, and the properties of argon where found in Bird [4]. DSMC uses a velocity input with units of meters per second while Alsmeyer's data is in terms of Mach number. The input velocities were calculated using the following equation:

$$M = \frac{V}{\sqrt{\gamma RT}} \tag{3.3}$$

The velocities and associated Mach numbers are tabulated below for ease of repeatibility:

Table 3.1:   Velocity Inputs Calculated From Mach Number

Mach	V (m/s)
1.5	478.25
2	637.67
3	956.51
6	1913.02
9	2869.18

According to Vincenti and Kruger, shock thickness can be related to the pre-shock supersonic velocity and the post-shock subsonic velocity over the velocity gra-

32

dient [12]:

$$\overline{x_u} \equiv \frac{u_\alpha - u_\beta}{|\frac{du}{dx}|_{max}} \qquad (3.4)$$

Where u_α is the before shock velocity, u_β is the after shock velocity, and the denominator is the maximum velocity gradient in the shock. Bird uses a similar equation, but instead of calculating shock thickness in terms of velocity, he uses density [4]. Bird's equation is used to find shock thickness in this project.

The information needed for Bird's equation comes from the data out file that is produced by the DSMC algorithm, which is then processed by a MATLAB™code written by Bentley and adapted by the author to calculate the shock thickness [11].

3.4 Comparison to 2-Dimensional Axisymmetric Cylinder Experimental Data

The third step in the research project is to compare the results of Bird's original code to experimental data that Bird also used for comparison [4, 14] by Davis. Simulations for this portion of the project were conducted using Bird's original code [4], a NoAR case, and a range of ϵ values which are 0%, 25%, 50%, 75%, 100%, and 200%. Bird's 2d axisymmetric code, and all the DSMC codes used in this project, can only create surfaces along a cell boundary and cells can only be rectangular [4]. Therefore the leading edge will not have a bevel in the simulations which may have a minor impact on the simulation - that impact will be taken into consideration when reviewing the results. The dimensions of the computational space are 0.15 m in the x-directon and 0.085m in the y-direction in order to match the experiment and subsequent simulations performed by Davis [17]. The computational domain in relation to the experimental set-up for the hollow cylinder is shown below in Figure **??**

The hollow cylinder is 1 mm from the bottom of the computational domain, and the leading edge begins at the left side of the domain. The cell size for the simulations is 1 mm in the x and y directions. A grid with cell dimensions of 0.5 mm, which is on the order of the mean free path, was also used in the study to see if the solution
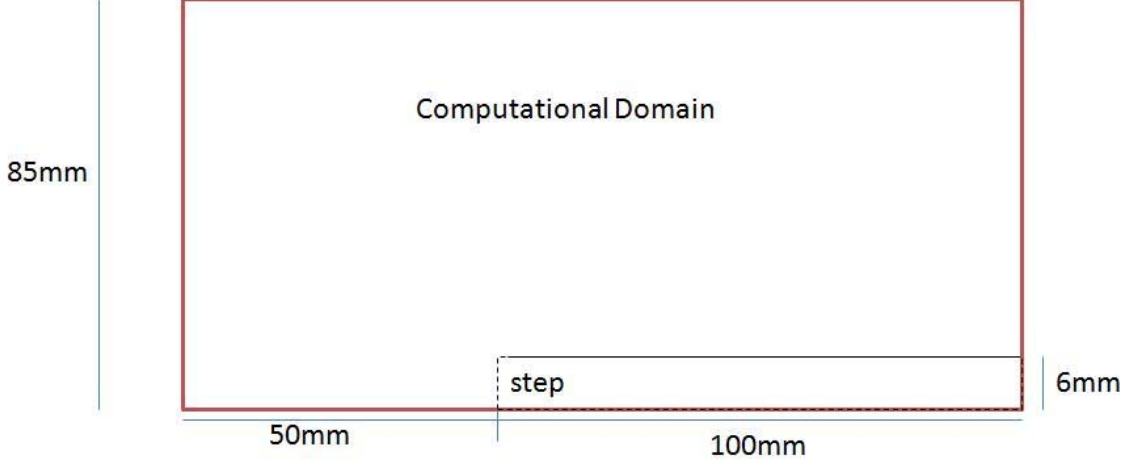
Figure 3.3:   Computational Domain

is improved. The hollow radius of the cylinder is not part of the computational space in the simulation, but the radius is not neglected. Bird's 2-dimensional axisymmetric code accounts for an internal radius that is not in the computational space [4].

In addition to comparing the results to experimental data, the results have been compared to each other. Contour plots generally provide a qualitative method of comparing results. In order to improve upon the comparison, the contour plots have been generated by subtracting the result of each of the SAR and NoAR algorithms from Bird's results, and dividing by Bird's result and multiplying by 100 in order to plot the percentage of difference between the results. For example, the density percent difference between Bird and the results of SAR with $\epsilon = 0\%$ is found by:

$$\rho_{\%diff} = \frac{\rho_{Bird} - \rho_{Eps00}}{\rho_{Bird}} 100 \tag{3.5}$$

There are some cases where the value of density will be zero, in particular where the step is. In Bird's code, the wall boundaries are defined in the data subroutine, but these areas with no flow are a part of the computational domain, and data is written out for these locations. Therefore, the areas of no flow need to be taken into account. For these cases, the density is assumed to be 10^{-6}, which gives a large value for the percent difference. The difference calculations were performed for density,

34

u-velocity, and temperature. These contour plots also give an idea of which cell the velocity data should be exported from for the speed distributions in order to see the largest difference between results. It would make sense that the cells with only small differences in the u-velocity would have similar velocity distributions while cells with larger differences will have disimilar velocity distributions. Choosing of the sample cells is further discussed in Section 3.5.

3.5 Velocity Distribution Comparisons

The velocity distributions as described in Section 2.6 will provide further insight into the behavior of the particles as they travel through the shock layer. Before the shock, the majority of the particles are traveling at the bulk velocity, which creates a thin profile. Within the shock, the particles transition from traveling at the bulk velocity to traveling at a lower speed via molecular collisions. The distributions in Section 2.6 show the behavior of the particles as they collide and eventually reequilibrate to a new flow velocity. Velocity distributions resulting from the DSMC, SAR, and NoAR simulations will be compared to Holtz and Muntz's data at Mach 7.18, and velocity distributions will also be created for Mach 1.5, 3, 6, and 9 in order to observe the change in the distributions with Mach number. As the Mach number increases, the shock becomes stronger and the perturbation from the equilibrium state becomes larger. The velocity distributions should reflect the change in the amount of nonequilibrium, and DSMC, SAR, and NoAR may handle the changes differently.

The distributions will all be normalized just as Holtz and Muntz normalized their distributions [19]. Using the normalized distributions gives a height of 1 for all the distributions and compares the particle velocities to the bulk velocity of the flowfield, which allows for direct comparisons regardless of the input bulk velocity used in the DSMC, SAR, or NoAR codes. The histogram program for the unweighted velocities uses the histogram function in MATLAB™ to calculate the distributions, which are then normalized. The weighted velocities required a different approach. With the unweighted velocity histogram, if a particle's velocity falls within a certain

bin, then one is added to the number of particles within that bin. The weighted particles however do not all have a weighting of one. Therefore, if a weighted particle's velocity falls within a bin, the weighting is added to the number of particles in the bin.

Speed distribution studies were initially accomplished with DSMC1S, and the modifications to the program with SAR and NoAR. The particle velocity components and weights at locations within the flowfield were exported into a file. The computational domain has 300 cells, with the shock occuring at the middle. The shock is at x=0 m, the left boundary is at x=-0.3 m, and the right boundary is at x=0.3 m. Mach 1.5, 3, 6, and 9 simulations have three sampling locations: before the shock, in the shock, and after the shock. The preshock sampling location is 10 cells into the domain from the left side of the domain, at x=-0.28 m. The location within the shock was chosen at cell 150 at x=0m, and the post shock location is cell 290 at x=0.28 m. The Mach 7.183 distributions were taken at sample locations based on the location of the normalized density. The DSMC, SAR, and NoAR simulations were all run 10,000 time steps, and the normalized density was calculated for each case. The simulations were then run again and the particle velocities were written at the locations of the normalized densities previously mentioned in Section 2.6.

The DSMC2A code is also used to investigate the velocity distributions. The flowfield is very complicated, and the velocity distributions are difficult to predict. The same flowfield complications make it difficult to choose which cells should be sampled for the distributions. Four locations were initially chosen as sample cells for the velocity distributions, which are 495, 795, 1255, and 1295 as seen in Figures 3.4 and 3.5. Cell 1295 was in the boundary layer for some of the simulations, which affected the comparison of velocity distributions, so 1255 and 1295 were replaced with 1705 and 1755. Cells 350 and 3669 were chosen by using the percent difference contour plots to determine the areas of the flow with the largest differences. Not entirely surprisingly, the biggest differences were found at the stagnation point (350) and in the shock layer (3669). The points are identified by the cell number that they

36

are assigned in DSMC. DSMC assigns each cell a number starting with one in the bottom left hand corner, and goes left to right and then up to the next row of cells. The figure below shows the location of the points in reference to the flowfield:
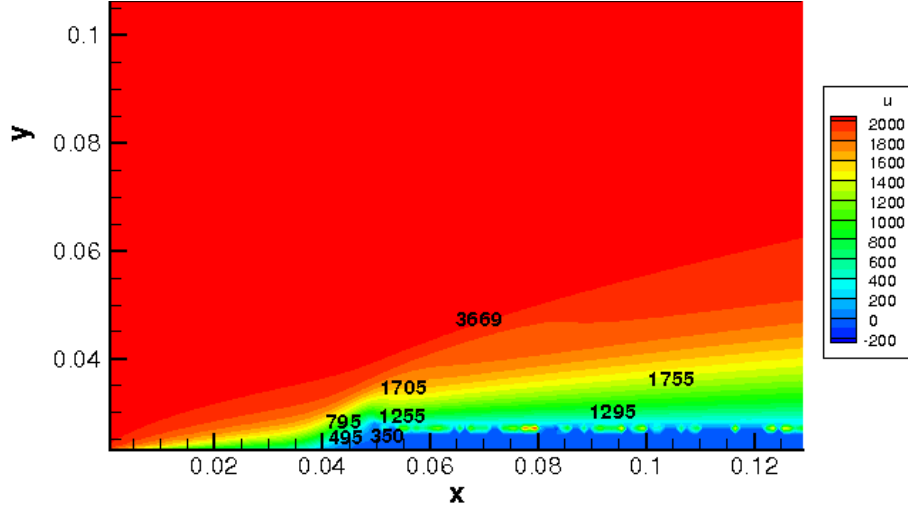
Figure 3.4:   Sampled Points on Velocity Contour Plot

The location of the shock is more easily visible in Figure 3.5, which is a contour plot of density rather than velocity.
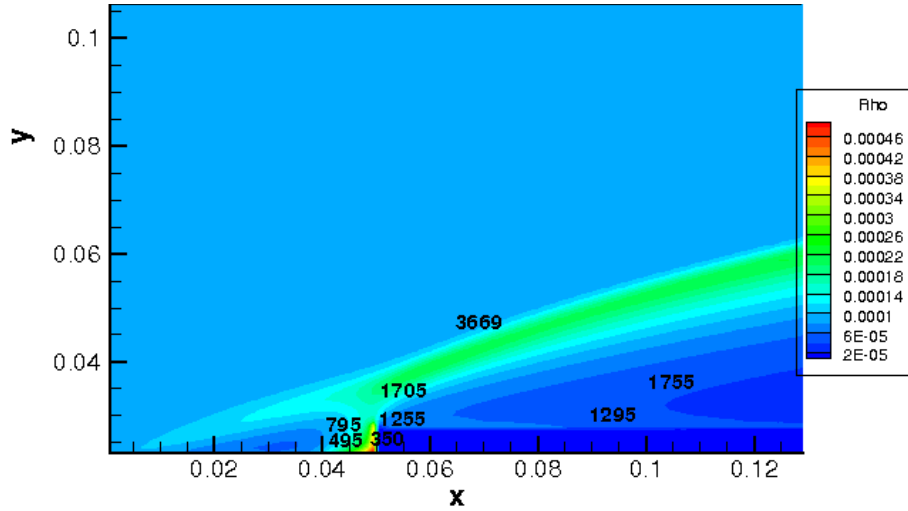
Figure 3.5:   Sampled Points on Density Contour

Figures 3.4 and 3.5 show that the recirculation region is represented by cells 495 and 795. Cell 350 is in the stagnation region, and 1255 and 1705 are just after the step. Cells 1295 and 1755 will show the behavior well past the step, and cell 3669 will allow the investigation of the shock layer velocity distributions. These points were sampled using Bird's code, NoAR, and SAR with ϵ values of 00%, 25%, 50%, 75%, and 100%. The distributions are compared visually and with the statistical equations discussed earlier in the section.

After creating all the plots and visually comparing them, it was determined that the histograms are only minutely different. A more precise way to compare them must be developed. Evaluating the characteristics of the distributions, such as maximum value, the average velocity, C_{mp}, and moments of the histogram, specifically kurtosis and skewness. The maximum value of n will be located in the velocity bin with the most probable velocity. If C_{mp} matches the location of the maximum n value, then the histogram programs are working correctly. A distribution with high kurtosis will be tall, thin, and pointed at the peak, while a low kurtosis distribution will be short, and broad. Sample kurtosis is calculated by [20]:

$$\overline{x^4} = \frac{\frac{1}{n}\sum_{i=1}^{n}(x_i - \overline{x})^4}{(\frac{1}{n}\sum_{i=1}^{n}(x_i - \overline{x})^2)^2} \tag{3.6}$$

Skewness is the measure of symmetry around the mean. A distribution with no skewness will be perfectly symmetric about the mean. A distribution with negative skewness is asymmetric, favoring the left of the mean and a distribution with a positive skewness favors the right side of the mean. Skewness of a sample distribution can be calculated by [20]:

$$\overline{x^3} = \frac{\frac{1}{n}\sum_{i=1}^{n}(x_i - \overline{x})^3}{(\frac{1}{n}\sum_{i=1}^{n}(x_i - \overline{x})^2)^{\frac{3}{2}}} \tag{3.7}$$

3.6 Hard Sphere Comparison

In order to verify if the SAR method can be used as a Mach dependent parameter, rather than VHS, that can be varied to produce a more accurate result, it is

necessary to use the HS model with SAR and compare to Bird's original code for a given Mach number. The DSMC1S and DSMC2A codes were both altered for HS. The collision cross-section of the particle is calculated using [4]:

$$\sigma_T = \pi d^2 \tag{3.8}$$

The diameter is constant, unlike the diameter in Equation 2.19. The results of the hard sphere model cases will be compared both to Bird's original code with VHS and SAR and NoAR codes with VHS. For DSMC2A, HS will be compared using the density plots from Davis. The DSMC1S, HS codes will be evaluated using line plots and inverse shock thickness calculations.

IV. Results

4.1 Random Walk Testing

The random walk testing results include variance and average kinetic energy. If the average kinetic energy stays relatively constant, there are no random walks in the system and the algorithms are conserving energy.
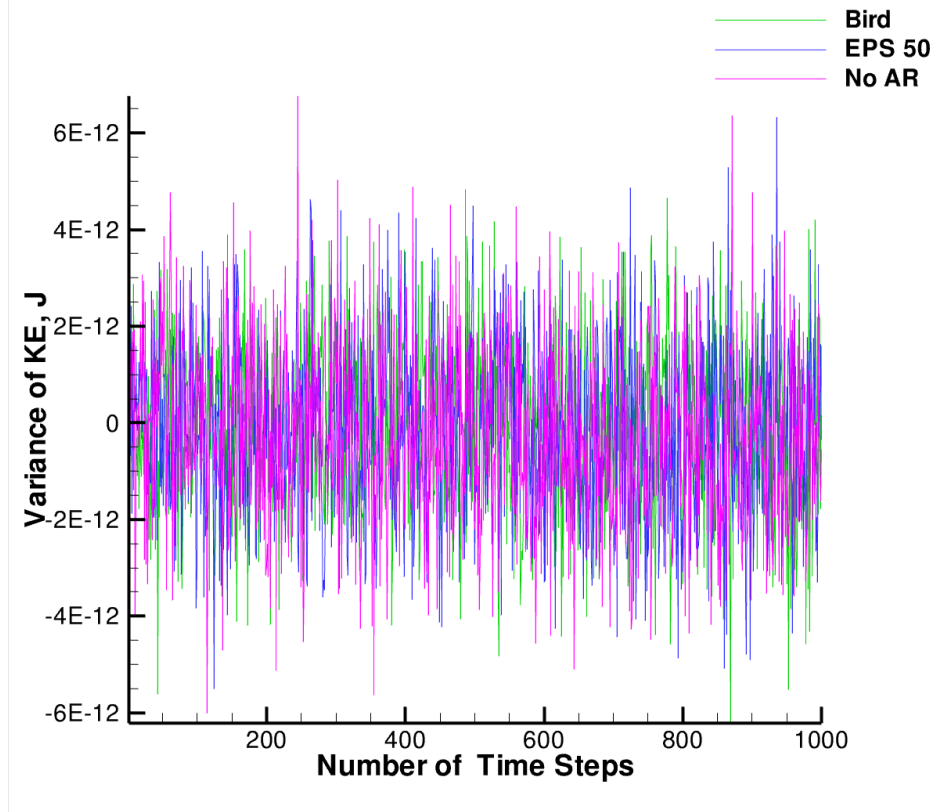
Figure 4.1: Variance for Random Walk Test

As can be seen in Figure 4.1, the variance for all three cases are on the same order of magnitude. The average kinetic energy stays constant at about 0.0004 while the variance is between $-6*10^{-12}$ and $6*10^{-12}$. The small amount of variance is most likely caused by rounding errors due to the computations performed by the computer, rather than problems with the codes.

4.2   1-Dimensional Shock Experimental Comparisons

4.2.1   Inverse Shock Thickness.   A few small changes were made in the sampling subroutine of DSMC1S from previous research, so the first part of the investigation was to verify that the inverse shock thickness plot is still showing the same behavior as was noted before.

Just as with Figure 3.2, the black line in Figure 4.2 is Alsmeyer's curve fit, and the blue line is the 6th order curve fit for all the experimental data. The crosses all represent simulation results, with the red being DSMC, blue is SAR 00%, pink is SAR 25%, yellow is SAR 50%, cyan is SAR 75%, green is SAR 100%, and black is NoAR. Through Mach 3, Bird's code matches well with the blue curve fit, but at Mach 4, Bird begins to over predict the shock thickness. Bird's symbol cannot always be seen on the figure because the SAR 00% data is colocated.

An effort was then made to curve fit the ϵ input values that would provide the correct inverse shock thickness for each given Mach number, and the resulting plot can be seen in Figure 4.3. The initial value of ϵ at each Mach number was found by interpolating the ϵ values using Figure 4.2. These values were then used as an input in a SAR simulation, and the output was used to calculate the inverse shock thickness. The resulting inverse shock thickness was then evaluated, and a new ϵ value was chosen if the inverse shock thickness did not match the blue curve fit. The process was repeated until the inverse shock thickness for each Mach number all matched the blue curve fit line in Figure 4.2. Figure 4.3 is the result of the ϵ fitting process just described.
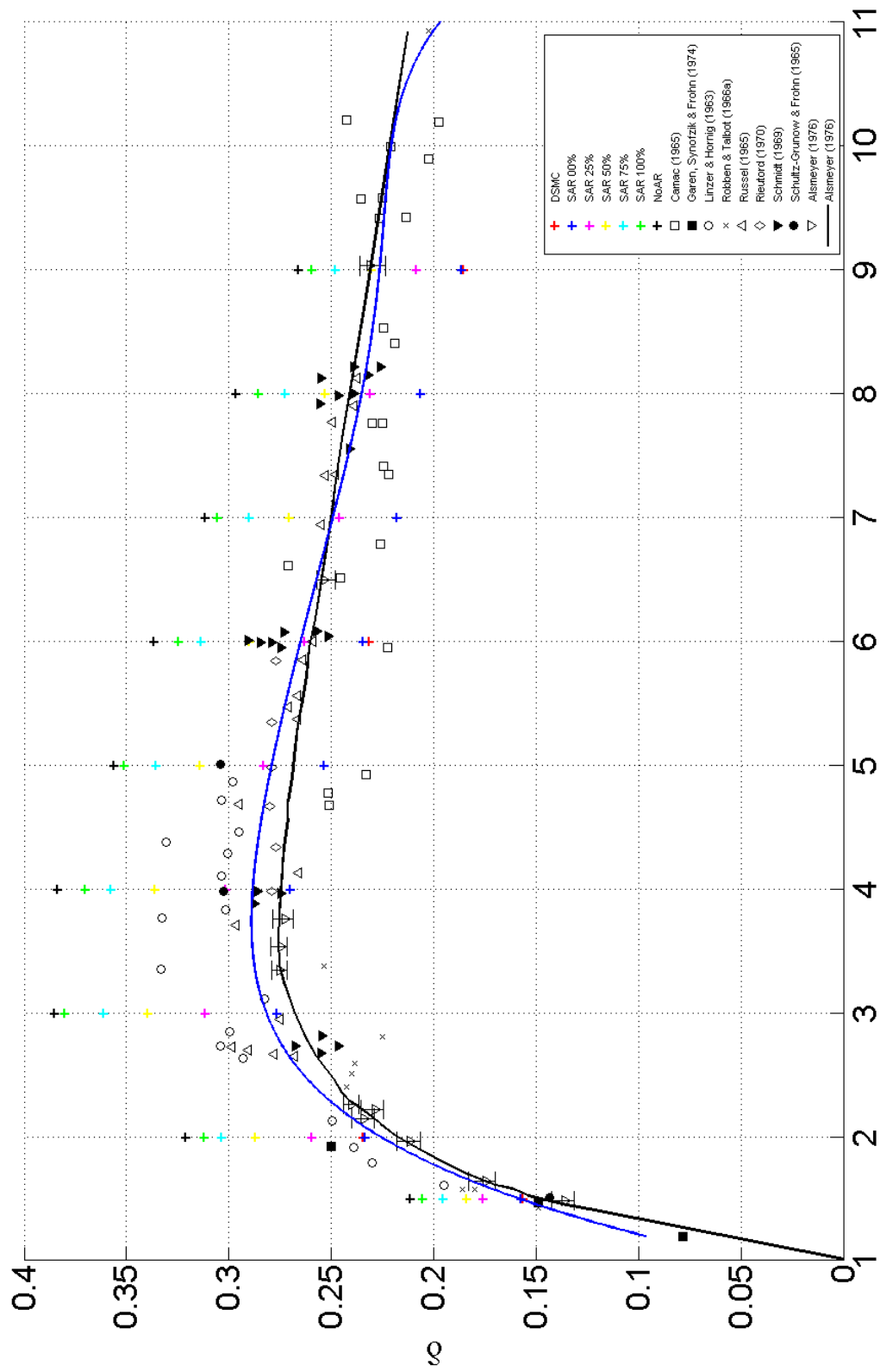
Figure 4.2: Inverse Shock Thickness vs Mach Number [1]
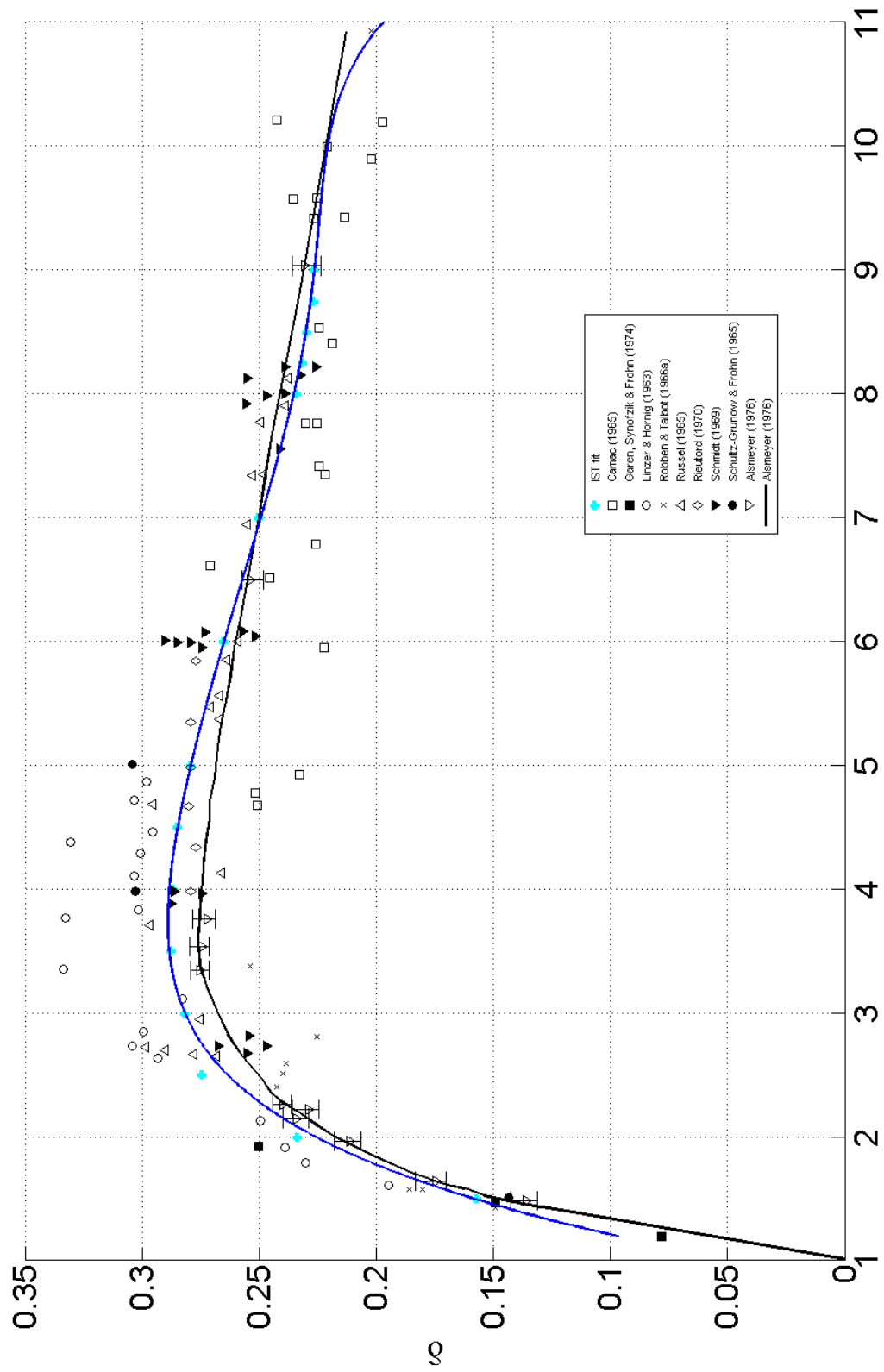
Figure 4.3: Inverse Shock Thickness vs Mach Number SAR Fit

The cyan crosses in Figure 4.3 are the calculated results. The Mach number and their associated ϵ values are displayed in the Table 4.1. The additional Mach numbers were added in areas where the change in ϵ versus Mach number were large in order to get a good understanding of the behavior in high gradient portions of the curve. Table 4.1 shows the values plotted in Figure 4.3.

Table 4.1: ϵ Values Fit to Mach Number

Mach	ϵ (%)
1.5	0
2	0
2.5	.5
3	5
3.5	10
4	15
4.5	18
5	22
6	27
7	28
8	30
8.25	30.5
8.5	33
8.75	34
9	45

Since Bird's results fit through Mach 3, the first two points in the curve fit are zero, which will negatively affect the curve fit. Two curve fits were therefore created, one that includes the first 5 points, and one that does not. The two curves in Figure 4.4 allow one to tell which curve fit will work best.

The orange line in Figure 4.4 represents the curve fit over the entire data set, the green line represents the curve fit of data above Mach 4, and the blue crosses are the points used to calculate the curve fits. One can see that the curve fit for the whole data set does not match the points between Mach 8 and Mach 9, but the curve fit for just the higher Mach data does match. Note the significant increase in ϵ required to maintain the correct inverse shock thickness at higher Mach numbers. In order
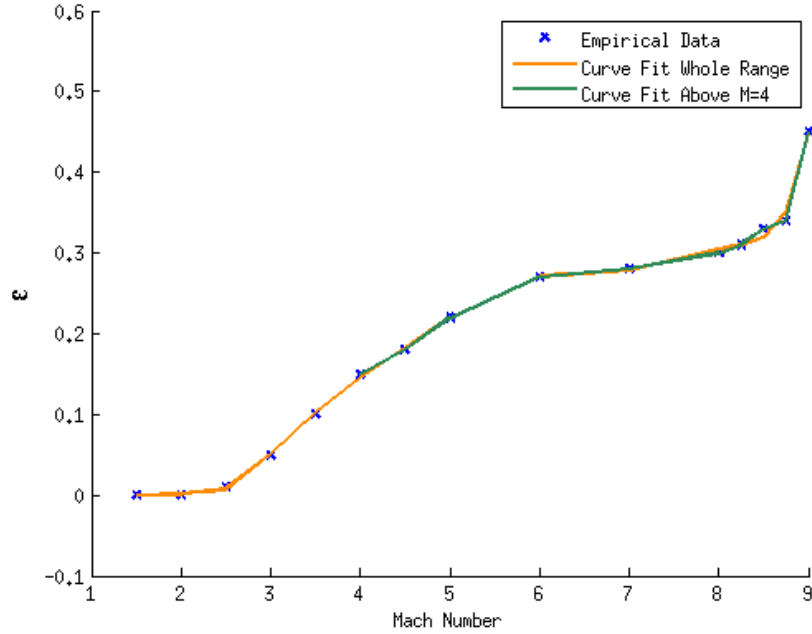
Figure 4.4:   Inverse Shock Thickness vs Mach Number Curve Fit

to better understand the relationship between the algorithms and Mach number in producing the correct inverse shock thickness, a graph was created that shows the percent difference between the experimental inverse shock thickness and the inverse shock thickness calculated by the algorithms. The experimental values used for the graph came from the blue curve fit of all the experimental data on Figure 4.2.

In Figure 4.5, Bird's and $\epsilon = 0\%$'s results match the experimental data at Mach 1.5, but then underpredict the shock thickness at Mach 2. After Mach 2, the two algorithms consistently predict a thicker shock compared to experimental data. $\epsilon = 25\%$ underpredicts the inverse shock thickness through Mach 5, but at Mach 6, is very close to the experimental data, which matches Figure 4.4. The higher ϵ values and NoAR predict a thinner shock at every Mach number in Figure 4.5. The overall behavior of Figure 4.5 matches Figure 4.4. The percent differences steadily rise until Mach 6 in Figure 4.5, and flattens out until Mach 8, at which point the percent difference increases drastically. The curve fit in Figure 4.4 increases also until Mach 6, becomes relatively flat until Mach 8, then spikes at Mach 9. One would

45
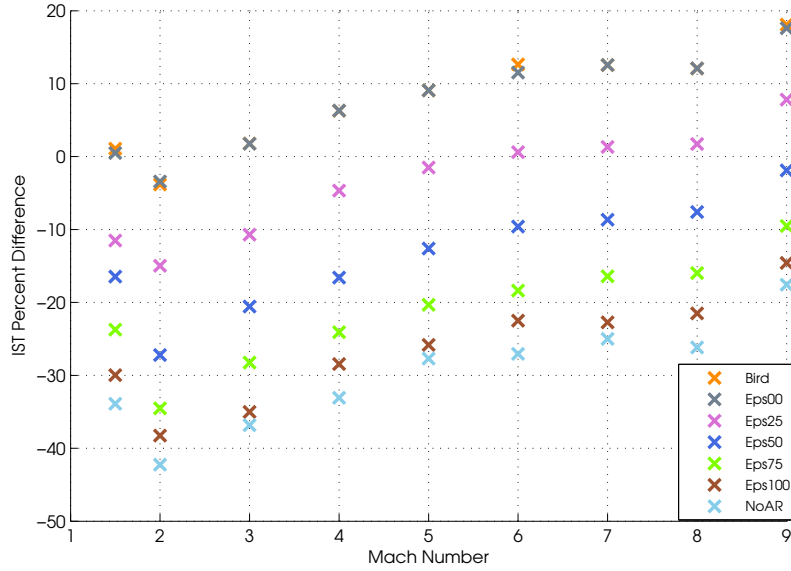
Figure 4.5:   Inverse Shock Thickness Percent Difference vs Mach Number

expect that these two graphs would match, since both of these graphs are different ways to show the relationship between Bird, SAR with different ϵ input values, and NoAR to an inverse shock thickness associated with Mach numbers. The relationship should be extended to higher Mach number data set to best confirm the relationship or modify it as needed for higher Mach numbers.

Now that it has been established that there is a Mach dependency, it is necessary to find out what causes the dependency. The first thing to look at is the collision ratio, which is the ratio of pairs of particles accepted (fully and partially) over the total number of pairs selected as possible collision partners.

In Figure 4.6, the blue diamond is $\epsilon = 100\%$, the red square is $\epsilon = 75\%$, the green triangle is $\epsilon = 50\%$, the purple x is $\epsilon = 25\%$, the blue start is $\epsilon = 0\%$, and the orange circle is Bird. NoAR by definition always has a collisions ratio of 1. Bird has the smallest collision ratio, which is expected since it has a binary accept/reject criteria. $\epsilon = 0\%$ provides the same values for the collision ratio as Bird. As ϵ increases, so does the collision ratio. The ϵ value will increase the number of partially accepted collisions, which increases the overall collision ratio. As Mach number increases, the
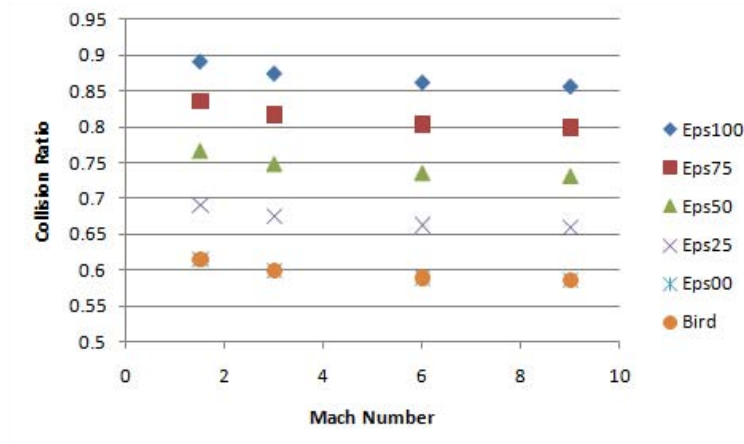
Figure 4.6:   Collision Ratio vs Mach Number

collision ratio decreases, and begins to reach an asymptotic limit. This limit is due
to the change of the velocity distribution with velocity.
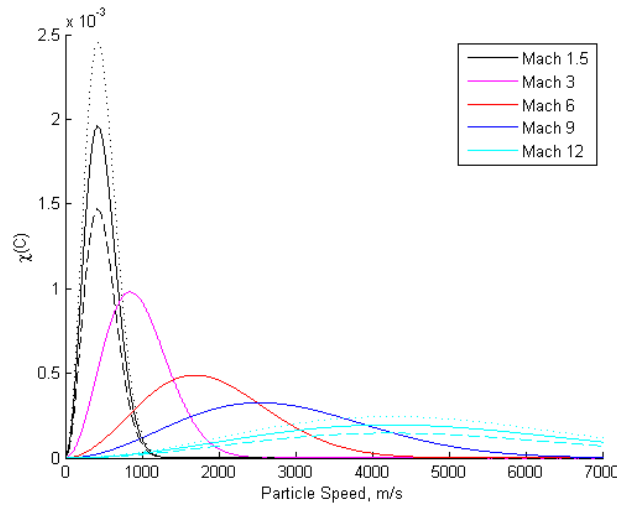
Figure 4.7:   Change in Velocity Distribution with Mach Number

In Figure 4.7, the black line is Mach 1.5, the magenta line is Mach 3, the red
line is Mach 6, the blue line is Mach 9, and the cyan line is Mach 12. The dotted black
and cyan lines represent the upper limit of the SAR criteria, and the dashed line is
the lower limit of the SAR criteria all for an $\epsilon = 25\%$ input value. One can see how
at lower velocities the distribution is tall and thin, but as the velocity increases the
distribution becomes shorter and wider. The change between Mach 1.5 and Mach 3

is drastic, but as the velocities become larger, the change in the distribution becomes smaller. These smaller changes result in smaller differences in collision ratio as the Mach number increases. Additionally, as the velocity increases, the maximum $\sigma_T c_r$ value is going to increase, which will decrease the likelihood of a particle pair having a large ratio in Equation 2.15, which will decrease the number of collisions that are accepted. This behavior is small though, and does not explain the drastic change in ϵ as Mach number increases required to match experimental data. The velocity distributions will allow for further investigation of the behavior of DSMC, SAR, and NoAR.

4.2.2   Velocity Distribution Comparisons.   The velocity distribution comparisons provide insight into the differences of the algorithms, especially with how well the algorithms keep with the assumption of local equilibrium. As previously stated, local equilibrium within the computational cells can be assumed if the cell size in on the order or smaller than the mean free path. The cell size for the 1-dimensional algorithms is one order of magnitude smaller than the mean free path. The Mach 7.18 case can be compared to Holtz and Muntz's experimental data. These distributions are taken using the velocity traveling in the x-axis in order to compare appropriately to the experimental data.

In Figure 4.8, Bird's result is the tan color with the x symbol, $\epsilon = 0\%$ is gray with the line, the $\epsilon = 50\%$ is the red line with the triangle, $\epsilon = 100\%$ is the green dashed line, NoAR is the blue line with the upside down triangle, and Holtz and Muntz's data is the blue circle. All of the distributions in Figure 4.8 are unweighted. The SAR distributions are created by using the modified accept/reject criteria, but the weightings are neglected, which allows for an understanding of the effect of the accept/reject portion of the algorithm by itself.
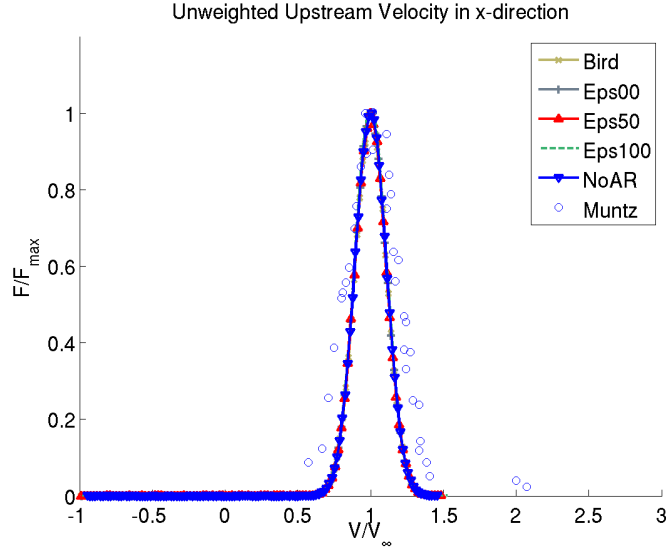
Figure 4.8: Unweighted Velocity Distributions Upstream of Shock

The distributions in Figure 4.8 are taken upstream of the shock, and at this point the distributions are thin. These cells are in equilibrium, and all of the distributions follow Holtz and Muntz's experimental data similarly well.
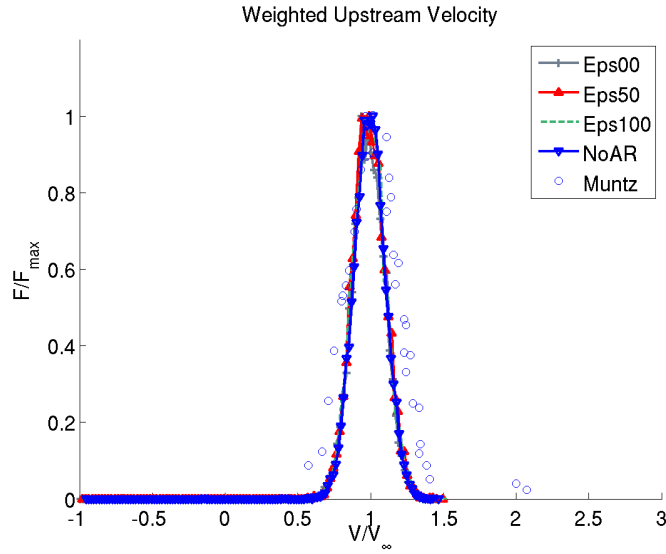
Figure 4.9: Weighted Velocity Distributions Upstream of Shock

Figure 4.9, the distributions are created using the particles weights based on the SAR methodology. Just as with the previous figure, all of the distributions match the experimental data well.
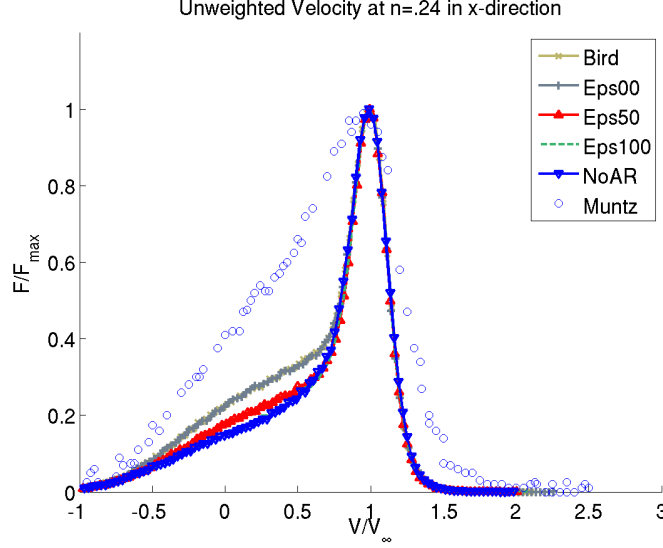
Figure 4.10:   Unweighted Velocity Distributions at $\hat{n} = 0.24$

Figure 4.10 shows the unweighted distributions about a quarter of the way through the shock structure. Bird and the unweighted SAR distributions severely underestimate the number of collided particles. There is a large number of particles at the bulk velocity, and few particles traveling slower than the bulk velocity. The $\epsilon = 0\%$ shows more particles traveling slower than the bulk velocity, and as the ϵ value increases, the number of particles tends towards NoAR. The NoAR distribution has the lowest number of particles traveling slower than the bulk velocity, indicating that the number of collided particles is fewer. The changes in accept/reject criteria allow for a wider range of particles to collide that would have otherwise been unable to, which causes minor changes in the distribution, as seen in the area of the distribution to the left of the peak at unity.

Figure 4.11 shows a similar peak as the unweighted distributions, but the portion of the distributions to the left of the peak are very different from the unweighted cases. The weighted $\epsilon = 0\%$ distribution matches well to the experimental, but pre-
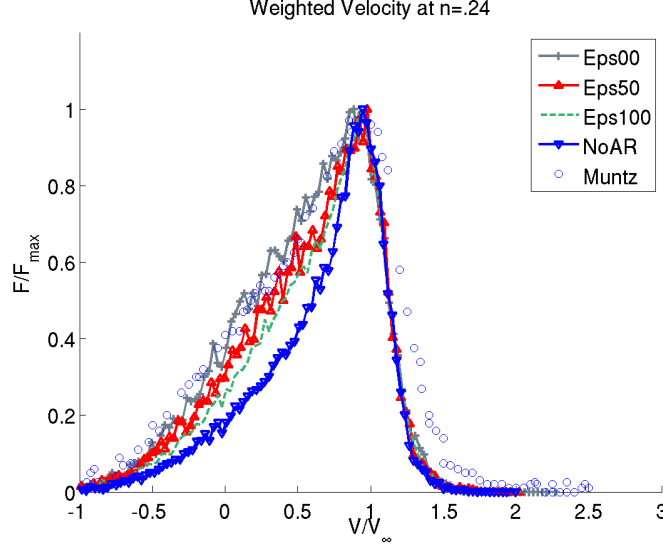
Figure 4.11: Weighted Velocity Distributions at $\hat{n} = 0.24$

dicts slightly more particles at the lower velocities than the experimental observations. The $\epsilon = 50\%$ distribution underpredicts the number of particles traveling less than the bulk velocity, as do $\epsilon = 100\%$ and NoAR. As ϵ increases, the number of particles traveling less than the bulk velocity decreases, which is most likely due to the weighting. As the band of partially accepted collisions increases, more particles are given a weighting between zero and one, and these partial weightings will decrease the number of particles compared to $\epsilon = 0\%$.

In Figure 4.12, the velocity distributions are taken at approximately one third of the way through the shock layer. The experimental plot widens as more particles have now collided and are traveling at velocities other than the bulk velocity. The unweighted distributions still show a thin peak at the bulk velocity and underpredicts the number of particles that are going slower than the bulk velocity. The number of particles to the left of the peak has increased compared to Figure 4.10, indicating that more particles have collided as the particles have move farther into the shock layer.

51
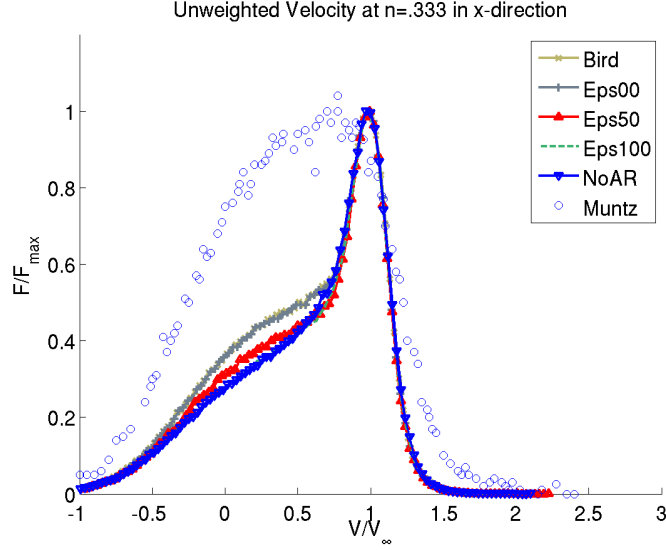
Figure 4.12:   Unweighted Velocity Distributions at $\hat{n} = 0.333$
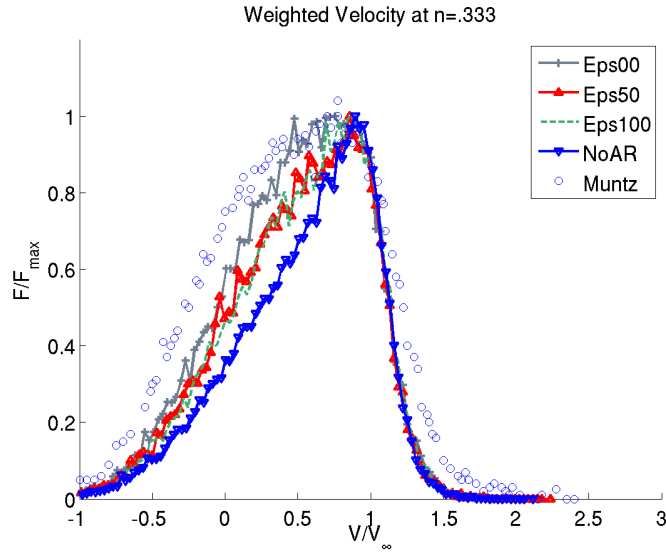
Figure 4.13:   Weighted Velocity Distributions at $\hat{n} = 0.333$

The weighted distributions in Figure 4.13 again show a much better comparison to experimental data than the unweighted distributions. All of the distributions underpredict the number of particles to the left of the peak, but match the peak well. As seen previously, the $\epsilon = 0\%$ case underpredicts the least, and NoAR underpredicts the most.
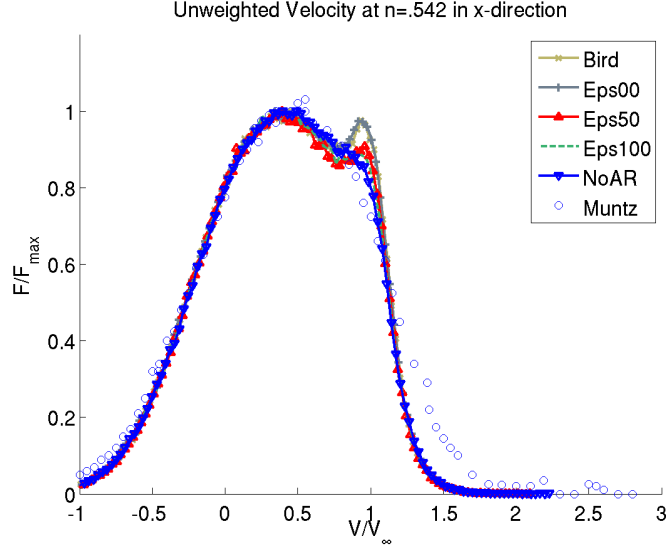
Figure 4.14:   Unweighted Velocity Distributions at $\hat{n} = 0.542$

The unweighted distributions in Figure 4.14 match the experimental data very well to the left of the peak at one, and the width of the distributions compare well to the experimental data. Bird and $\epsilon = 0\%$ have the most pronounced peak at one, and as ϵ increases, the peak is reduced. NoAR does not show a peak, but the slope does not quite match the experimental data.
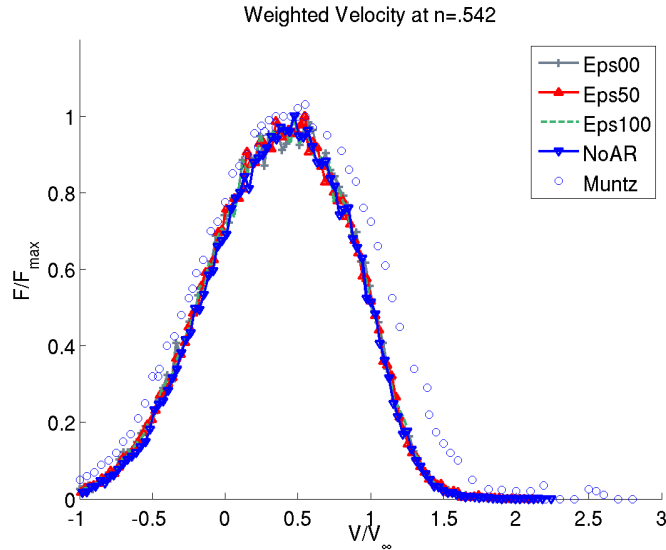
Figure 4.15:   Weighted Velocity Distributions at $\hat{n} = 0.542$

Figure 4.15 shows that all of the weighted distributions match very well to the experimental data. The experimental velocity distribution is very near to the post shock equilibrium distribution, and as will be seen in the next figure, there is little change after this point in the shock structure. All of the weighted distributions show that enough collisions have occured in order to compare favorably to the experimental data. Even the unweighted distributions shown in Figure 4.14 are fairly close to matching the experimental distribution.
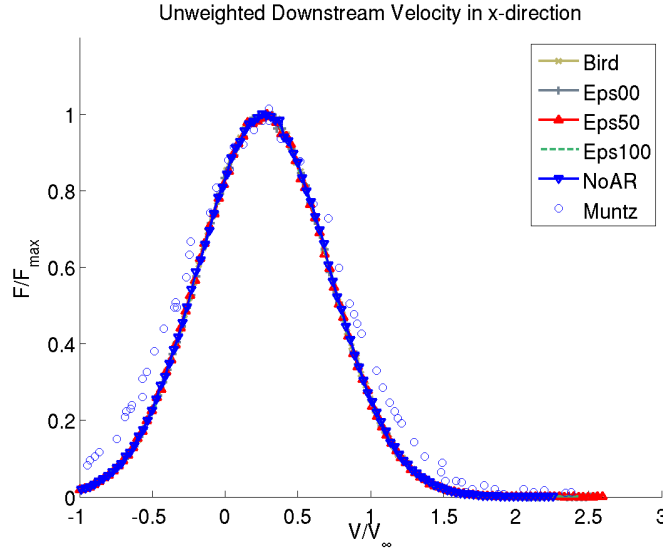
Figure 4.16:   Unweighted Velocity Distributions Downstream of Shock

Downstream of the shock, in Figure 4.16, the flowfield has returned to an equilibrium state. The unweighted distributions again are very similar to the experimental data, which confirms the idea that in equilibrium the algorithms produce similar results because the collision integral is not a factor.

In Figure 4.17, there is very little difference between these distributions, and they all compare well to the experimental data. Just as with the unweighted distributions downstream of the shock, now that the flow has returned to an equilibrium state, all of the algorithms produce comparable results.
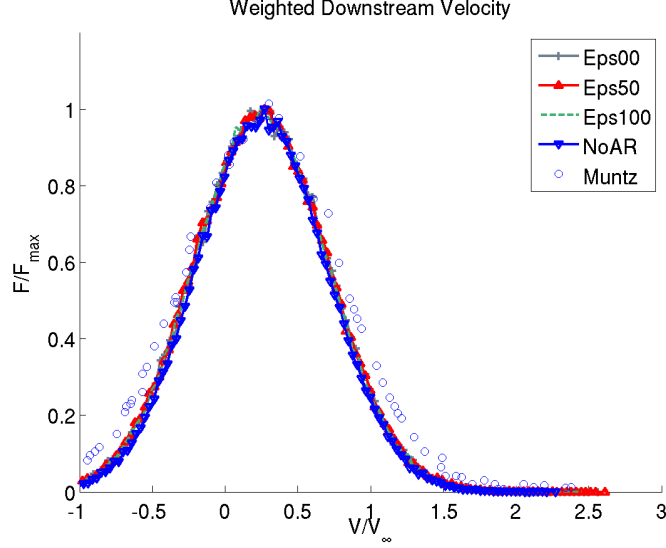
Figure 4.17: Weighted Velocity Distributions Downstream of Shock

The results of the experimental comparison show that in equilibrium, the results of the algorithms are very similar, but in nonequilibrium within the shock layer, clear differences can be seen. Bird and the unweighted SAR and NoAR distributions show that the algorithms do not predict the collision rate accurately, which results in particles maintaining the bulk velocity longer through the shock than is seen in experiment. The weighted SAR distributions better match the experimental data, with the lower $\epsilon = 0\%$ matching best compared to $\epsilon = 100\%$ and NoAR. NoAR matches the worst of the weighted distributions through the shock, even though NoAR has the highest collision rate.

4.3   1-Dimensional Data

4.3.1   Line Plots.   Line plots were created using Mach 1.2 and Mach 9 cases for density, u-velocity, and temperature in order to gain an understanding of how the SAR algorithm affects the flowfield parameters at the lowest and highest Mach numbers evaluated in this study. Mach 1.2 was the first case evaluated:

In Figure 4.18, Bird's result is green, $\epsilon = 0\%$ is red, $\epsilon = 25\%$ is blue, $\epsilon = 50\%$ is brown, $\epsilon = 75\%$ is light blue, $\epsilon = 100\%$ is orange, and NoAR is purple. The color
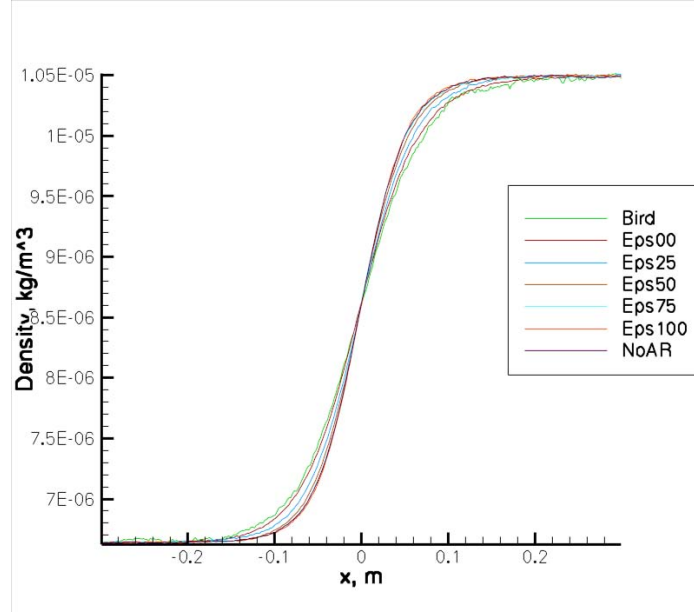
Figure 4.18:   Density Line Plot for Mach 1.2 Normal Shock

scheme for each case is kept throughout this report for ease of reading. Bird's results and $\epsilon = 00\%$ do not lie on top of each other. However, Bird and NoAR are still the extrema with the SAR results in between. The same is true for the velocity in Figure 4.19.
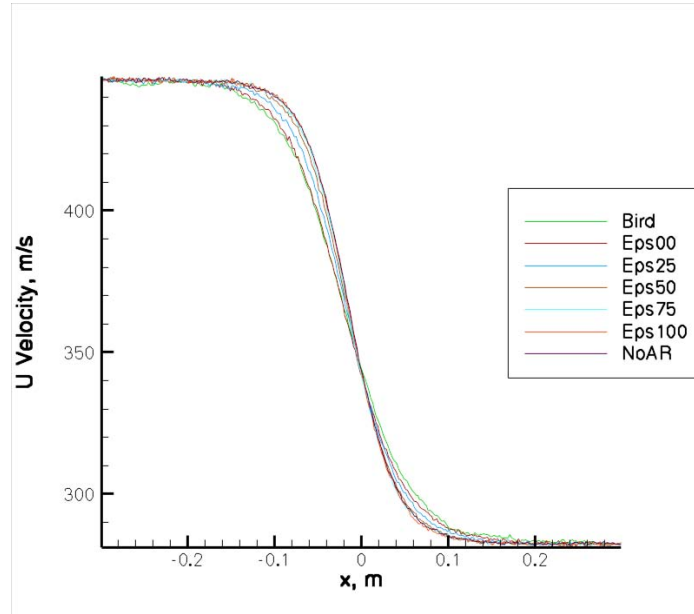
Figure 4.19:   U-Velocity Line Plot for Mach 1.2 Normal Shock

Magnifying the figure at the top of the profile, it can be seen that all the results of $\epsilon = 75\%$ and higher lie on the NoAR results. Additionally, the NoAR result does not show as much variance as the other cases.
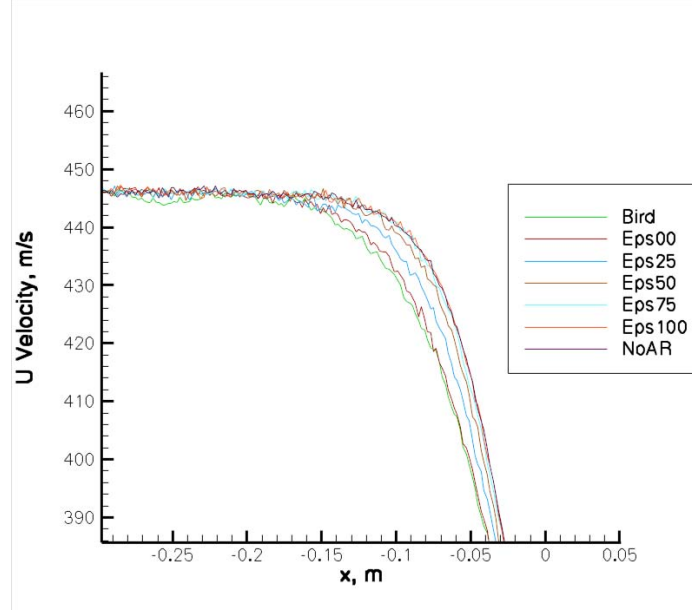
Figure 4.20:   U-Velocity Line Plot for Mach 1.2 Normal Shock Zoomed In

The temperature profile shows that the SAR results seem to be offset by about 18 K compared to Bird and NoAR. The codes both have the same initial temperature in the data subroutine, so the issue must be one of sampling.

An attempt to offset the temperature difference shown in Figure 4.21 by changing the input temperature in the data subroutine still does not line up with Bird's results. It should be noted that Bird's results matches the analytical temperature difference using normal shock relations, while SAR does not.
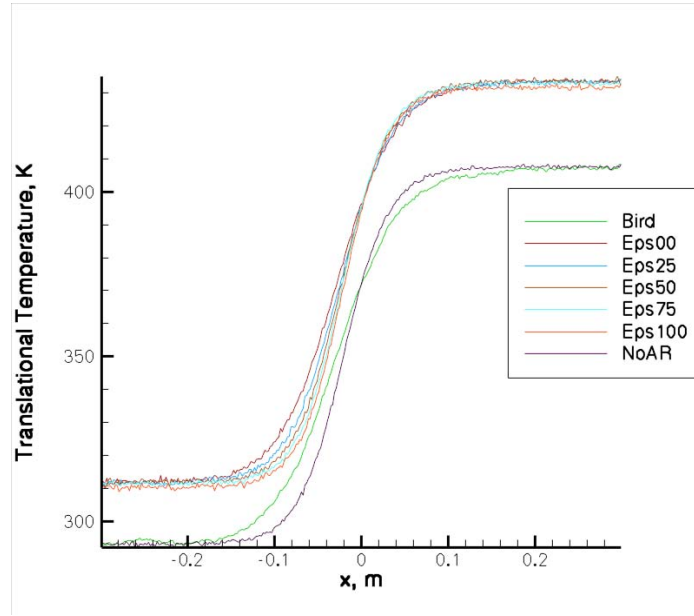
Figure 4.21:   Temperature Line Plot for Mach 1.2 Normal Shock
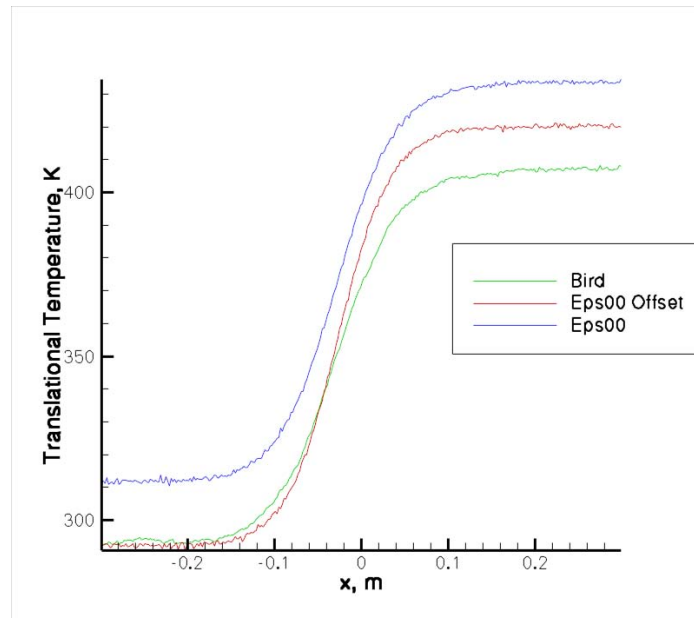
Figure 4.22:   Temperature Line Plot for Mach 1.2 Normal Shock with Offset

Additionally, the change in input temperature affects other parameters, as seen in Figure 4.23. The offset value causes the velocity after the shock to be smaller than it should be. The issue with temperature needs to be looked at further in order to understand why only that flowfield parameter is affected while velocity without the
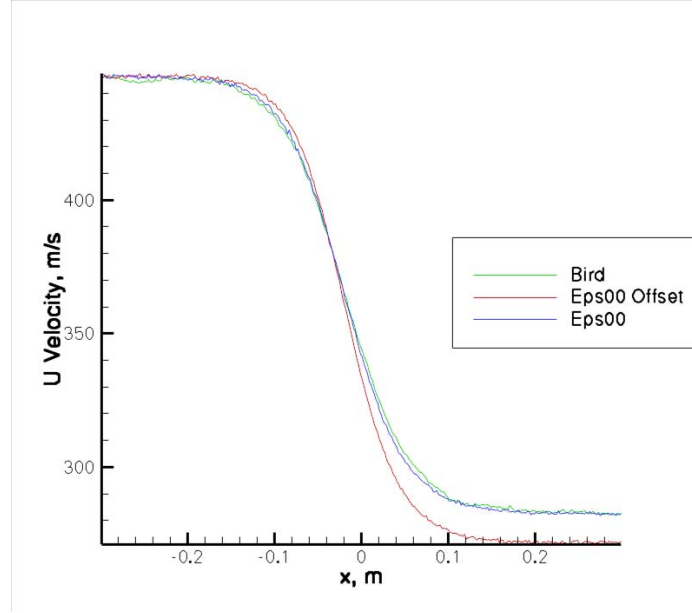
Figure 4.23:   U-Velocity Line Plot for Mach 1.2 Normal Shock with Offset

offset seems to produce good results. A considerable amount of time investigating the temperature issue has not led to any resolution of the problem, and DSMC2A SAR algorithms do not have this issue.

Line plots have also been produced for Mach 9 in order to understand the effect of higher velocities on the flowfield properties.

Bird and $\epsilon = 0\%$ do not match exactly. It was expected that they would match since they have the same accept/reject criteria and density is not sampled based on weighting. The Mach 9 results show much less variance than the Mach 1.2 results, even though they are both computed for 10,000 time steps, which can be seen by the smooth lines as compared to Mach 1.2.
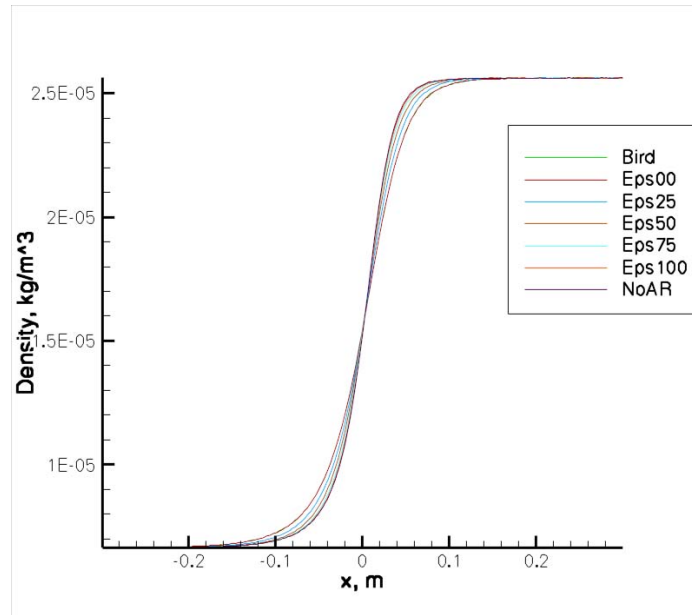
Figure 4.24:   Density Line Plot for Mach 9 Normal Shock
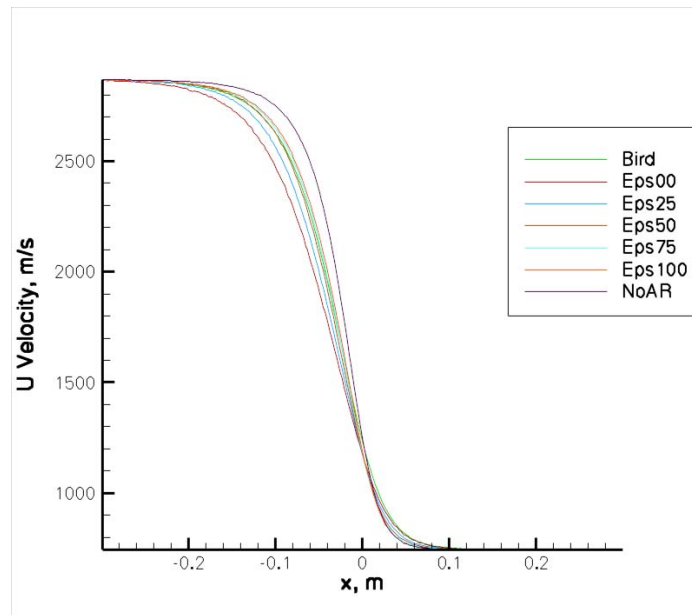
Figure 4.25:   U-Velocity Line Plot for Mach 9 Normal Shock

Bird is not at the extrema, but rather in the middle of the SAR results. The smooth lines can best be seen in the magnified velocity profile in Figure 4.26.
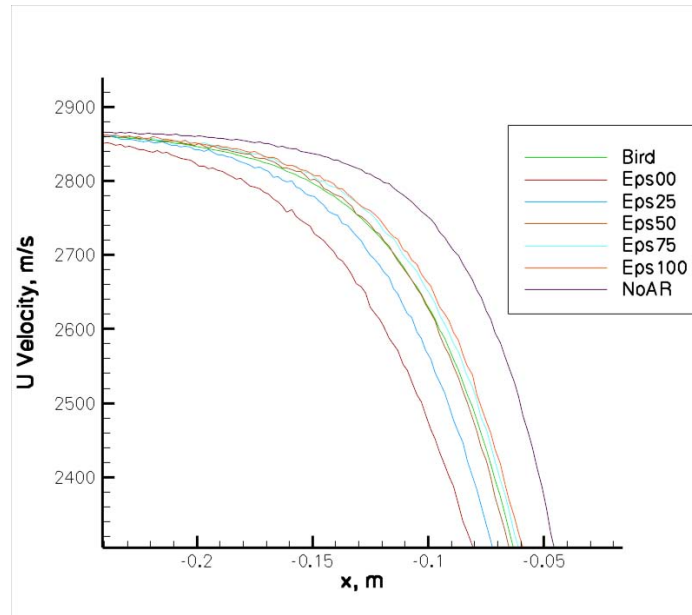
Figure 4.26:   U-Velocity Line Plot for Mach 9 Normal Shock Zoomed In

Again, the SAR temperature values are offset from Bird and NoAR in Figure 4.27. There does not appear to be a significant offset before the shock, but after the shock there is a difference of about 500 K.
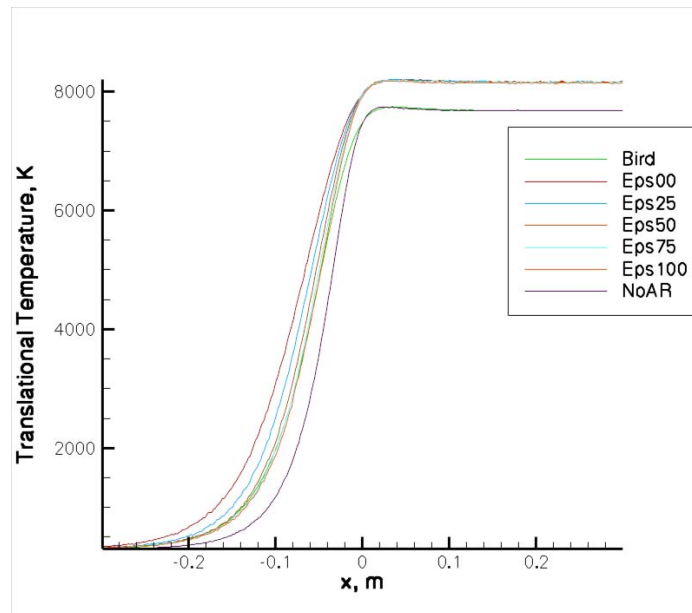
Figure 4.27:   Temperature Line Plot for Mach 9 Normal Shock

The Mach 9 line plots are very similar to Mach 1.2 plots with the exception of the smoother lines. Additionally, the change in flowfield properties across the shock is larger, due to the stronger shock typical of a much higher Mach number. Velocity distributions will be evaluated next in order to compare the macroscopic properties to the particle velocities.

4.3.2 Velocity Distributions. There are two sets of velocity distribution data for the SAR and NoAR algorithms. The first set is all the particles in the cell, without regard to weighting, which will show how the surface would experience the flow in the SAR and NoAR algorithms, since weighting is not taken into account for the reflect module [4]. The weighted and unweighted distributions will also show if the changes are due more to the change in collision rate due to the SAR method or if they are due to the weighting scheme. The velocity distributions were sampled at four different Mach numbers: 1.5, 3, 6, and 9 before the shock, in the shock, and after the shock. The distributions will be compared each other, and are sampled after the collision in order to correctly investigate the influence of the accept/reject changes on the flowfield.
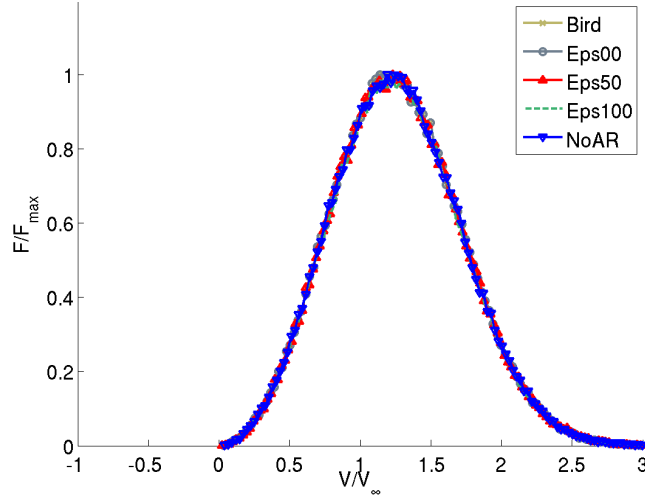
Figure 4.28:   Unweighted Velocity Distributions Before Shock Mach 1.5

In Figure 4.28, the unweighted velocity distributions for Bird, ϵ values of 0%, 50% and 100%, and NoAR before the shock was plotted in the same manner as the

simulation data compared to Holtz and Muntz was plotted. The distributions are all nearly identical, which shows again that the change in accept/reject criteria is not the main cause of the flowfield changes, but rather the weighting associated with SAR created the large differences. All of the simulation results have a peak to the right bulk velocity. Since these distributions are taken before the shock, one would expect the peak to be at one. The distributions are wider than the upstream velocity distribution in Figure 2.11, which is due to the lower velocity of the flow field. The unweighted $\epsilon = 0\%$ distribution is identical to Bird's distribution, as is expected. $\epsilon = 0\%$ has the same accept/reject criteria as Bird, therefore the only difference between a SAR algorithm with $\epsilon = 0\%$ and DSMC is the weighting. If weighting is neglected, the flowfields match exactly.
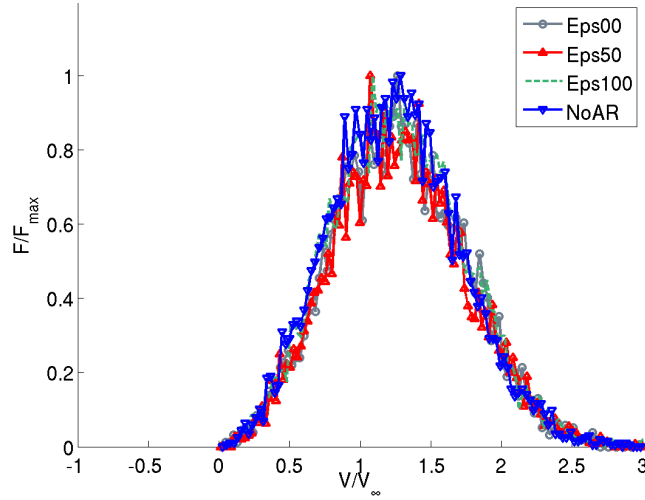
Figure 4.29:   Weighted Velocity Distributions Before Shock Mach 1.5

The weighted distributions in Figure 4.29 are jagged compared to the unweighted distributions, which due smaller sample size. The peak of the weighted distributions is in the same location as the unweighted distribution.
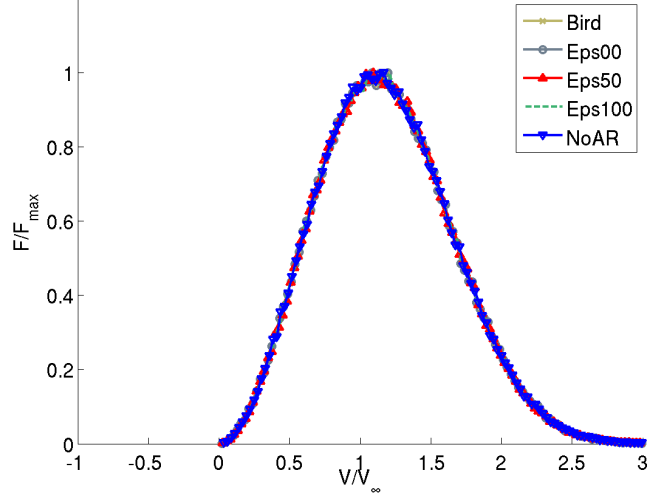
Figure 4.30:   Unweighted Velocity Distributions In Shock Mach 1.5

In Figure 4.30 the distributions are very similar to the distributions before the shock. A shock at Mach 1.5 is fairly weak, and the amount of nonequilibrium is fairly small. Therefore, the macroscopic flowfield parameters and the velocity distributions will show smaller changes compared to shocks at higher Mach numbers.
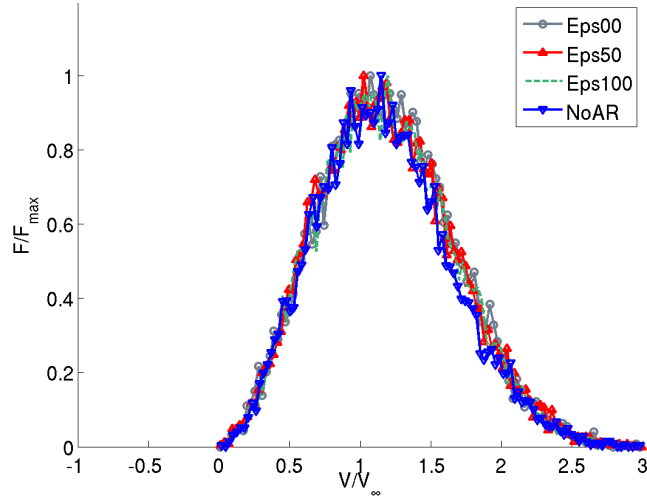
Figure 4.31:   Weighted Velocity Distributions In Shock Mach 1.5

In Figure 4.31, the weighted distributions are slightly less jagged than before the shock, which is due to a larger number density in the shock which increases the

sample size of the distribution. The peaks for the weighted distributions are in about the same location as the peaks of the unweighted distributions.
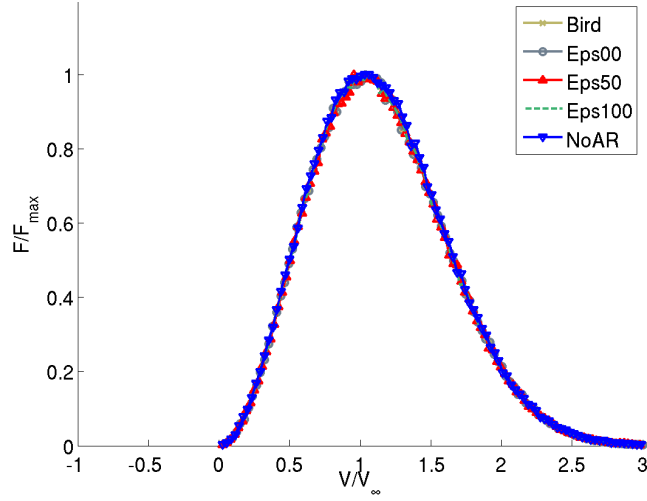
Figure 4.32:   Unweighted Velocity Distributions After Shock Mach 1.5

After the shock, in Figure 4.32, the distributions again look very similar to the distributions before the shock and in the shock. Since the shock is weak, it is expected that the distributions would not change very much, but it was expected that the peak of the distribution would be at a location less than one.
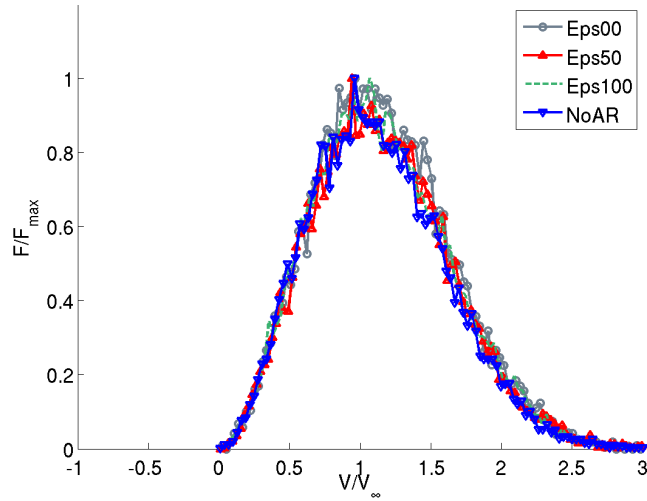
Figure 4.33:   Weighted Velocity Distributions After Shock Mach 1.5

The weighted distributions in Figure 4.33 are still fairly jagged. The changes in the distribution across the shock are very minor, so a larger Mach number will need to be investigated in order to show how the distributions compare when there is a larger gradient within the shock, which leads to more of a nonequilibrium condition.
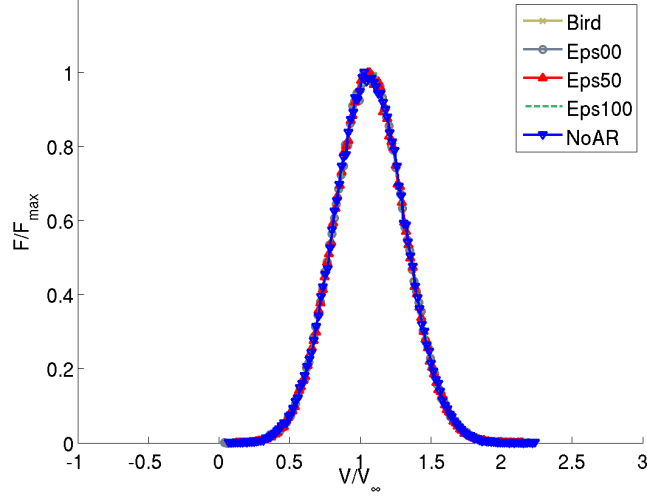
Figure 4.34:   Unweighted Velocity Distributions Before Shock Mach 3

As seen in Figure 4.34, at Mach 3, the preshock distributions are thinner than the Mach 1.5 preshock distributions. The distributions are still centered to the right of the bulk velocity, but they are not as far off as they were in the Mach 1.5 case. All of the unweighted distributions are very similar to each other, just as was seen with the Mach 1.5 figures.
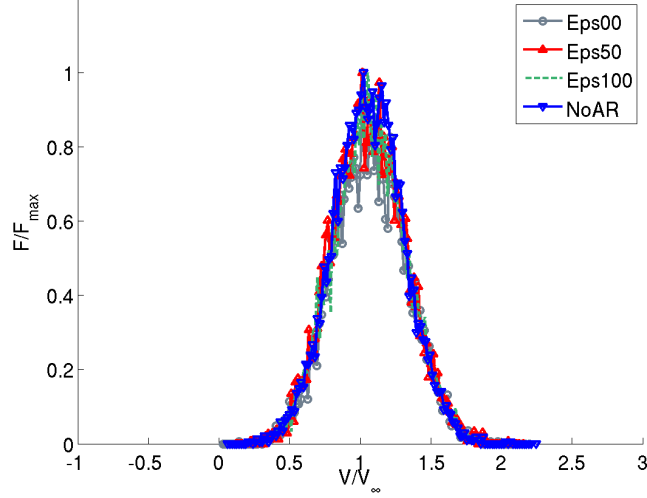
Figure 4.35:   Weighted Velocity Distributions Before Shock Mach 3

The weighted distributions in Figure 4.35 are very jagged compared to the unweighted distributions. The $\epsilon = 100\%$ distribution is less jagged than the $\epsilon = 0\%$ distribution, and NoAR is the least jagged of the weighted distributions. As ϵ value increases, so does the sample size, and NoAR has the largest sample size of weighted distributions and therefore is more smooth.
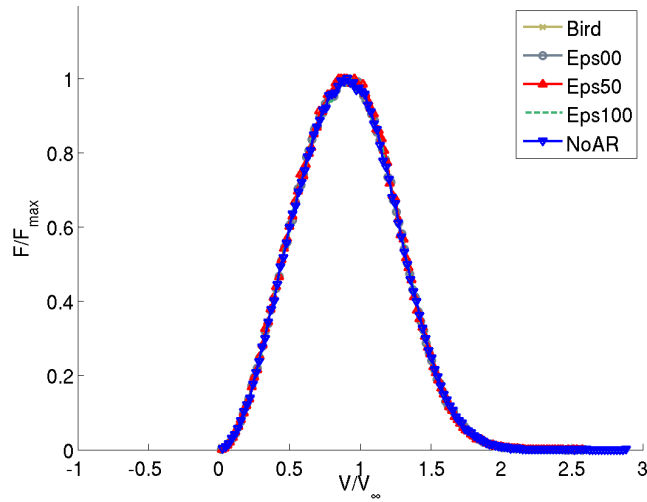
Figure 4.36:   Unweighted Velocity Distributions In Shock Mach 3

Figure 4.36 shows a wider distribution for all of the cases compared to the distributions before the shock. Also, the distributions are centered around a value less than the bulk velocity, as expected.
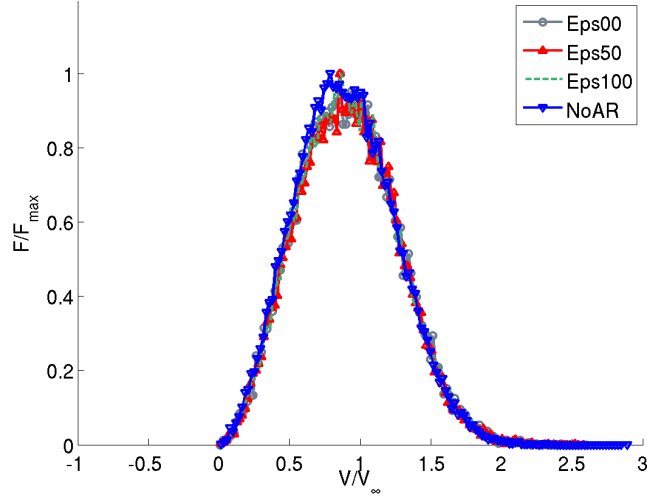
Figure 4.37:   Weighted Velocity Distributions During Shock Mach 3

Just as with Mach 1.5, the weighted distributions in the shock are less jagged than before the shock due to an increase in density in Figure 4.37. The weighted NoAR distribution is very smooth, and other than being flatter at the top of the distribution, very closely resembles the unweighted NoAR distribution.
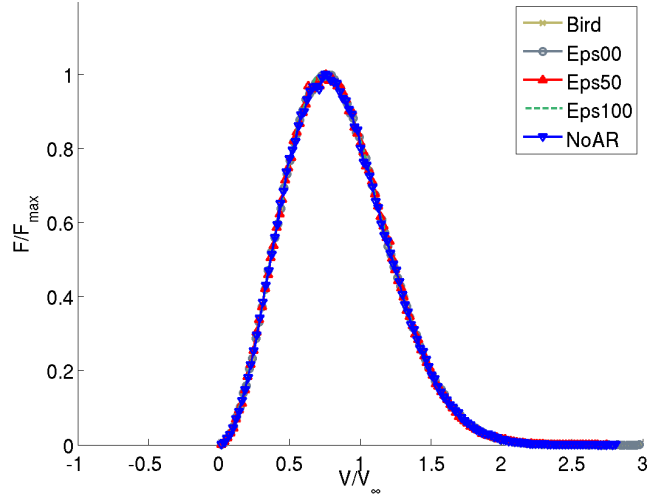
Figure 4.38:   Unweighted Velocity Distributions After Shock Mach 3

Figure 4.38 shows that after shock the distributions are centered to the left of the bulk velocity, which indicates that the particles have reequilibrated around a new bulk velocity that is lower than the upstream bulk velocity. So far, there has been very little difference between the unweighted distributions at each location, which indicates that the change in the collision rate does not play as large of a role in the flow field compared to the weighting.
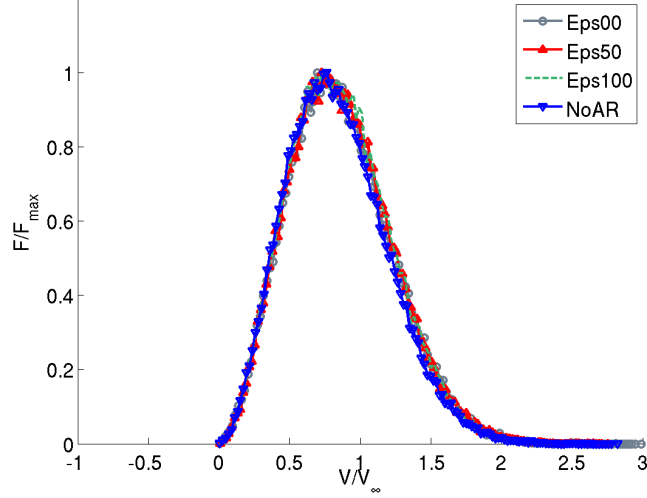
Figure 4.39:   Weighted Velocity Distributions After Shock Mach 3

The weighted distributions in Figure 4.39 after the shock are very similar to each other, as is expected because this portion of the flowfield is in equilibrium. The weighted NoAR distribution again is the most smooth of the weighted distributions. There is very little difference between the weighted distributions in the shock and the distribution after the shock, except for the fact that the distributions after the shock are more smooth.
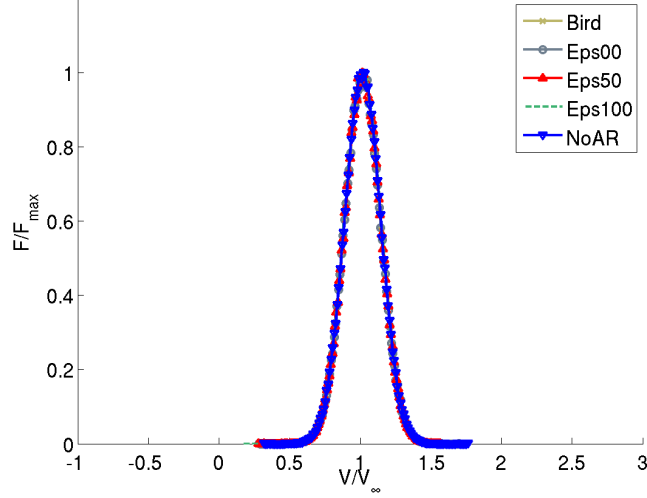
Figure 4.40:   Unweighted Velocity Distributions Before Shock Mach 6

In Figure 4.40, the unweighted distributions are more thin than the lower Mach numbers already investigated. These distributions, which are at Mach 6, are centered on the bulk velocity, unlike the lower Mach numbers.
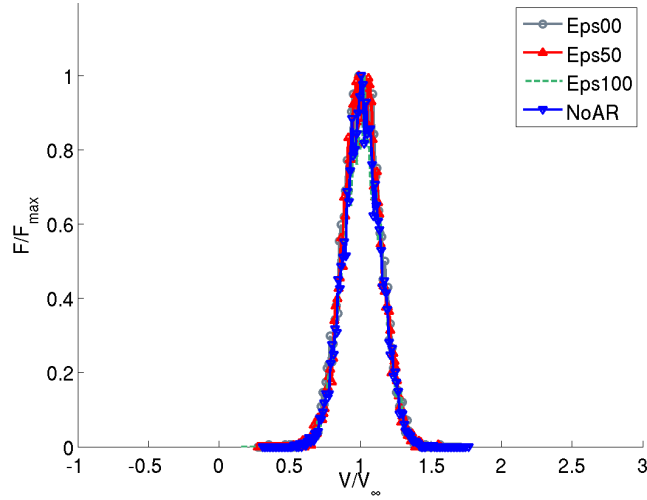
Figure 4.41:   Weighted Velocity Distributions Before Shock Mach 6

The weighted NoAR is still the most smooth of the weighted distributions in Figure 4.41. The weighted $\epsilon = 0\%$ distribution is jagged at the top. The distributions are centered on one, as expected.
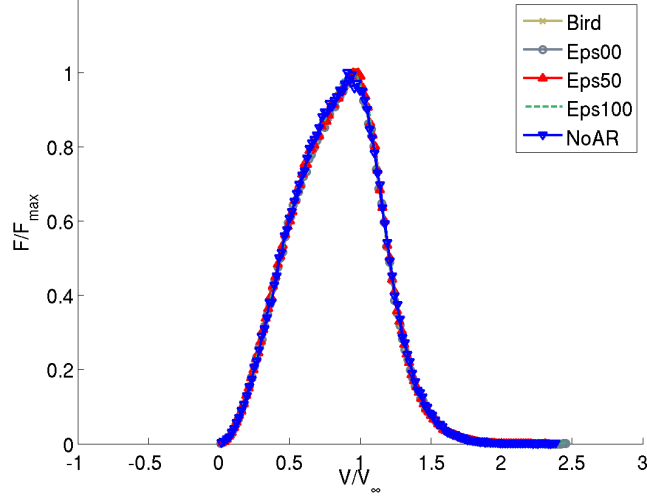
Figure 4.42:   Unweighted Velocity Distributions In Shock Mach 6

In Figure 4.42 the unweighted distributions have a peak at the bulk velocity, but the distribution is asymmetric and skewed to the right. Particles have collided and are moving slower than the bulk velocity, but there are still a significant portion of particles traveling at the bulk velocity.
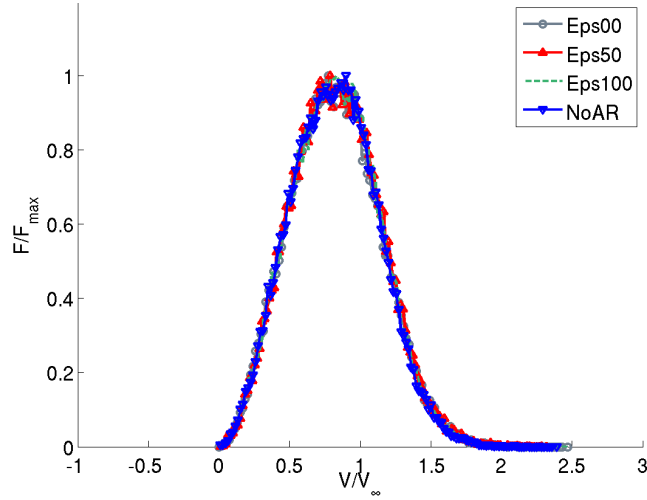
Figure 4.43:   Weighted Velocity Distributions In Shock Mach 6

The weighted distributions in Figure 4.43 has a peak to the left of the bulk velocity, which makes sense because the sampling is only from particles that have

71

collided. The weighted distributions are more symmetric and look more like the equilibrium distributions seen outside of the shock layer, which is expected.
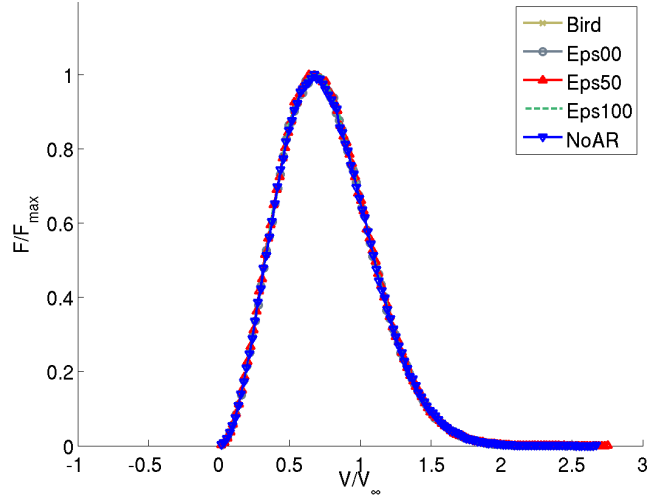
Figure 4.44:   Unweighted Velocity Distributions After Shock Mach 6

Figure 4.44 shows that after the shock, the unweighted distributions again look very similar to each other, indicating that in equilibrium the algorithms will simulate similar flow fields. The peak of the distributions are to the left of one, which shows that the bulk velocity after the shock is less than the bulk velocity before the shock.
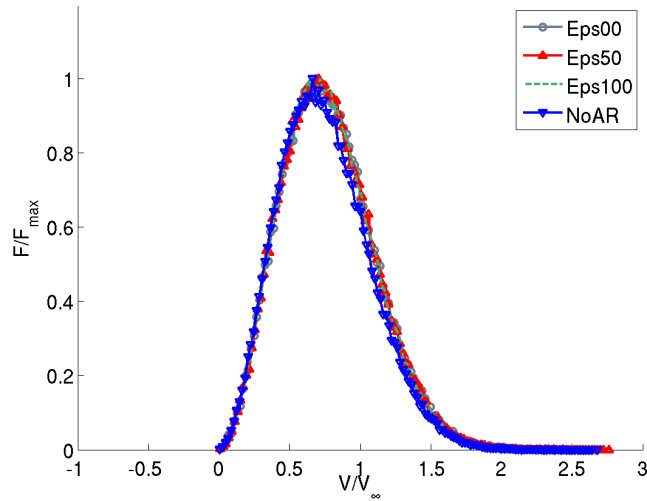
Figure 4.45:   Weighted Velocity Distributions After Shock Mach 6

The weighted distributions in Figure 4.45 are very similar to the unweighted distributions shown in the previous figure. The weighted distributions are less jagged than the distributions at lower Mach numbers, which is due to the increased density after this strong shock.
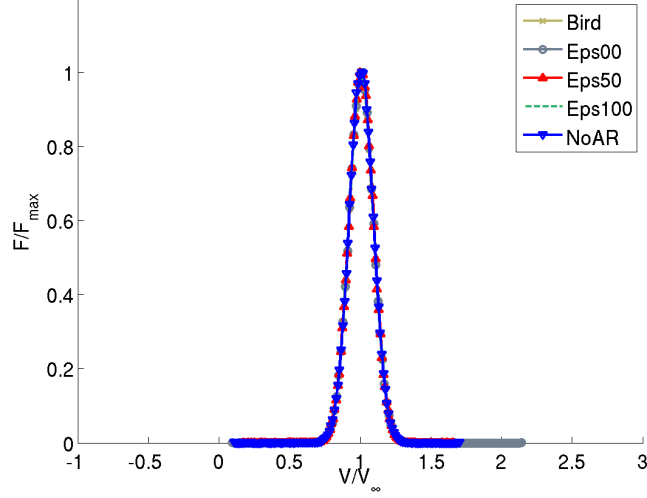
Figure 4.46:   Unweighted Velocity Distributions Before Shock Mach 9

In Figure 4.46, the distributions are all very thin and identical to each other. The peaks are located at the bulk velocity.
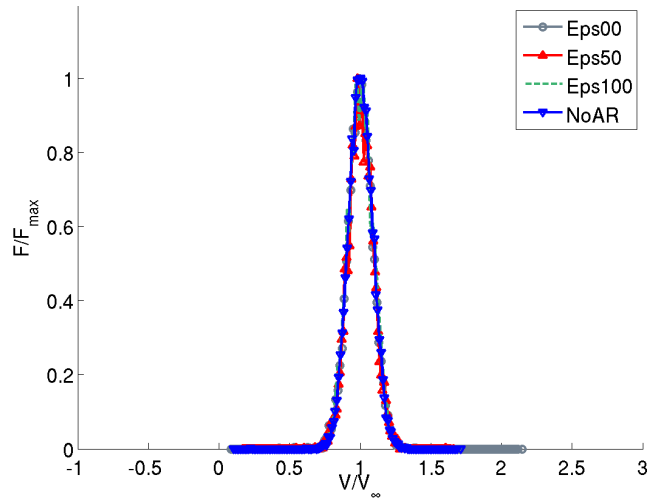
Figure 4.47:   Weighted Velocity Distributions Before Shock Mach 9

The weighted distributions in Figure 4.47 are thin and very similar to the unweighted distributions in Figure 4.46. NoAR has the smoothest distribution compared to the other weighted distributions, but overall they are comparable.
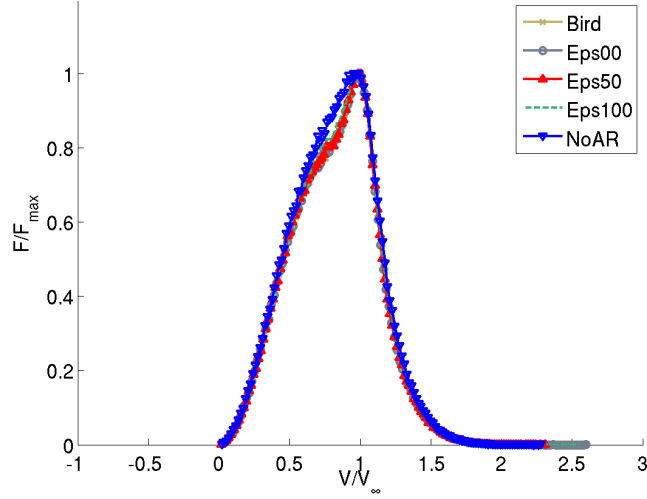
Figure 4.48:   Unweighted Velocity Distributions In Shock Mach 9

The bimodal distribution as discussed by Holtz and Muntz [19] is more distinguishable at Mach 9 in the unweighted distributions in Figure 4.48. NoAR shows the least bimodal behavior compared to the other unweighted distributions.
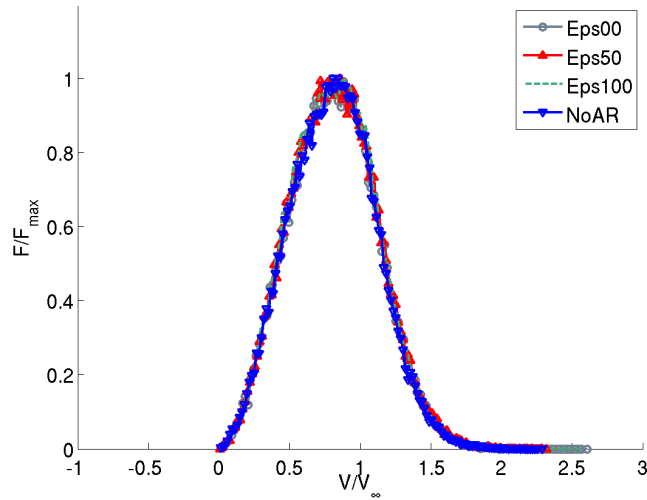
Figure 4.49:   Weighted Velocity Distributions In Shock Mach 9

The distributions in Figure 4.49 are not bimodal because all the particles have collided and are in equilibrium with each other. The weighted distributions match each other well and are nearly symmetric around the peak.
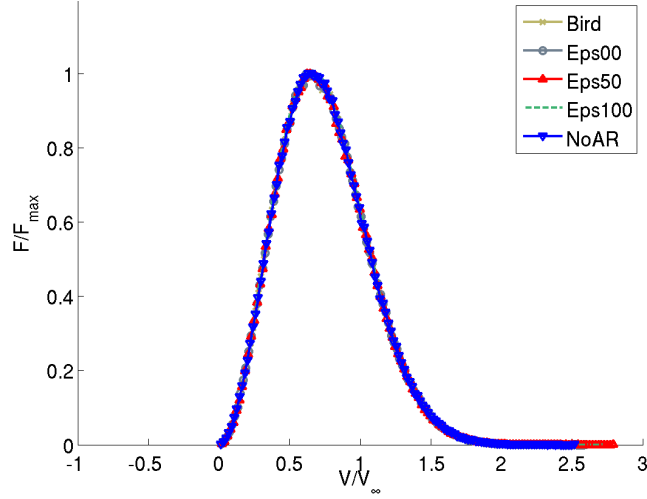
Figure 4.50:   Unweighted Velocity Distributions After Shock Mach 9

After the shock, in Figure 4.50, the unweighted distributions return to an equilibrium distribution with a peak at less than the bulk velocity. The distribution after the shock is much wider than before the shock because the particle collisions within the shock tend to create a distribution wider than before the particles collided.
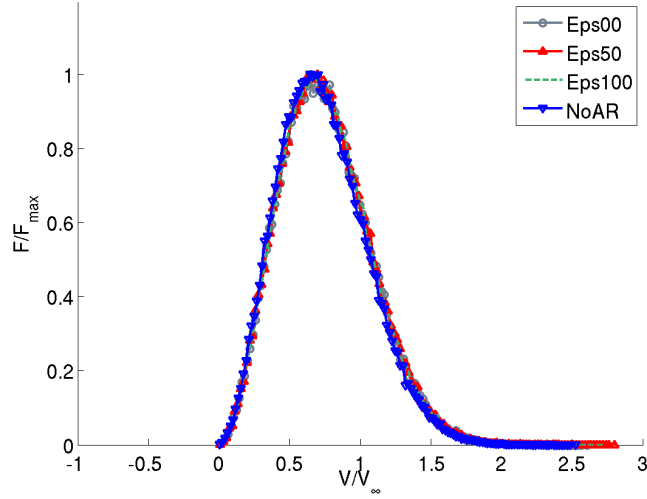
Figure 4.51:   Weighted Velocity Distributions After Shock Mach 9

In Figure 4.51, the weighted distributions are smoother than at lower Mach numbers, but still not as smooth as the unweighted distributions show in the previous figure. The distributions are very similar to the weighted distributions within the shock, but the peak is farther to the left after the shock. the nonequilibrium areas are where the major differences between the algorithms will be observed.

Based on the Holtz and Muntz comparison, and the further inspection of velocity distributions at four different Mach numbers it appears that Bird's code does not allow for enough collision to occur in order to properly equilibrate the cell. In order to confirm this idea, the Mach 9 simulation using Bird's code was run again, but the velocities of collided particles were accounted for separately from the uncollided particles. The collided and uncollided distributions were graphed both normalized and not normalized in order to allow the reader to see the overall affect and to be able to compare the distributions to distributions already shown.

(a) Not Normalized   (b) Normalized
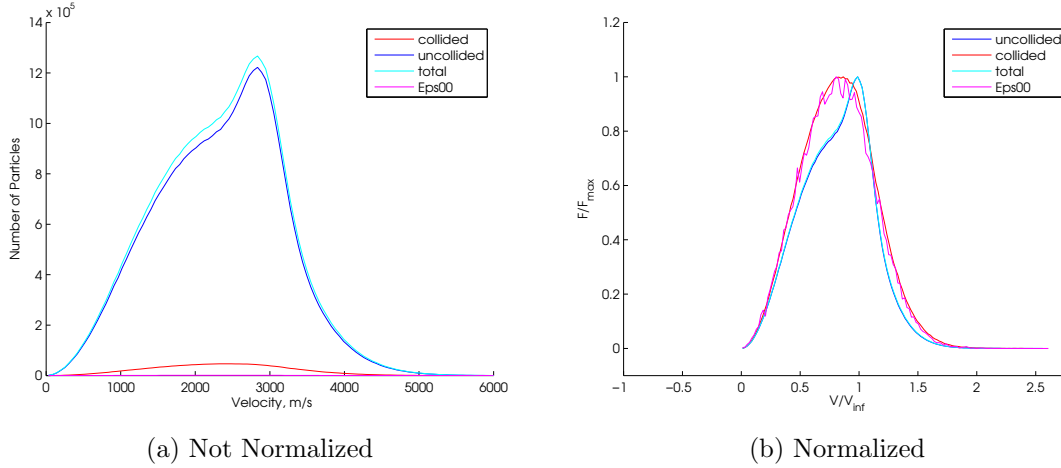
Figure 4.52:   Velocity Profiles for Collided and Uncollided Particles In Shock M=9

As seen previously with the Mach 9 distribution in the shock, there is a definite peak at the bulk velocity. Looking at just uncollided particles results in a distribution that is very similar to the distribution one gets when looking at all of the particles, regardless of weighting. However, the distribution of just the collided particles is substantially different. The smaller peak is due to particles that have collided in

76

previous cells. DSMC re-indexes the particles after each time step because of particles entering and leaving the flowfield. Therefore it is not currently possible to track the history of the particles and make a distribution of particles that have collided previously and a separate distribution of particles that have never collided. The distribution that has not been normalized shows that the number of collided particles is much smaller than the number of collided particles. The distribution is incredibly short compared to the uncollided distribution, but nearly as wide. The normalized distribution again shows the bimodal distribution for the uncollided particles, but the collided particles look very similar to the $\epsilon = 0\%$ weighted distribution which has been overlaid on the plot. Next, the statistical properties of the distributions looked at so far should be investigated for a better comparison.

The column on the left in Table 4.2 is the unweighted values, and the column on the right is the weighted values with the values grouped by algorithm and location. Kurtosis and skewness are calculated using equations 3.6 and 3.7. C_{mp} is the velocity that corresponds to the peak of the distribution, which loses some meaning with the bimodal distributions, so the average velocity is also calculated. The input velocity for Mach 1.5 is 478 m/s, and the analytically calculated value for the velocity after the shock is 278 m/s. As noticed with the distributions, the C_{mp} values for all the Mach 1.5 distributions are higher than the input velocity. The average velocities are a little higher than the most probable velocities, which implies that the distributions are skewed to the right. The skewness values are positive, which also indicates that the distributions are skewed to the right. The kurtosis values only vary slightly through the shock as would be expected given the minor changes observed when visually comparing the distributions. The shock is weak at Mach 1.5, therefore the flowfield does not change significantly through the shock.

77

Table 4.2:   Distribution Properties M=1.5

Bird	Kurtosis	Skewness	Cmp	Avg Vel
before	2.0221	0.7642	544.89	604.23
during	1.8668	0.6671	518.79	565.67
after	1.9740	0.7413	494.94	547.41

Eps00	Kurtosis	Skewness	Cmp	Avg Vel		Eps00	Kurtosis	Skewness	Cmp	Avg Vel
before	2.0221	0.7642	544.89	604.23		before	2.0394	0.7419	604.37	617.08
during	1.8668	0.6671	518.79	565.67		during	1.8794	0.6571	512.27	578.63
after	1.9740	0.7413	494.94	547.41		after	1.9532	0.7213	460.89	562.21

Eps25	Kurtosis	Skewness	Cmp	Avg Vel		Eps25	Kurtosis	Skewness	Cmp	Avg Vel
before	1.9627	0.7266	574.44	604.24		before	2.0647	0.7295	568.00	611.97
during	1.8313	0.6391	528.21	566.72		during	1.7927	0.5937	560.34	577.21
after	2.1445	0.8558	500.10	547.69		after	2.1556	0.8416	537.07	563.01

Eps50	Kurtosis	Skewness	Cmp	Avg Vel		Eps50	Kurtosis	Skewness	Cmp	Avg Vel
before	1.8073	0.6025	589.31	604.57		before	1.9954	0.6500	512.63	616.19
during	1.8174	0.6308	522.26	566.27		during	1.7965	0.6036	490.44	573.87
after	1.9542	0.7266	456.59	547.81		after	1.9090	0.6933	449.86	559.62

Eps75	Kurtosis	Skewness	Cmp	Avg Vel		Eps75	Kurtosis	Skewness	Cmp	Avg Vel
before	1.8271	0.6288	572.24	604.08		before	1.9166	0.6429	614.57	608.73
during	1.7691	0.5896	532.97	566.37		during	1.7417	0.5492	551.64	576.95
after	1.9076	0.6934	500.12	547.17		after	1.9057	0.6714	480.42	561.00

Eps100	Kurtosis	Skewness	Cmp	Avg Vel		Eps100	Kurtosis	Skewness	Cmp	Avg Vel
before	1.8643	0.6445	586.36	604.23		before	1.7874	0.5720	519.87	612.48
during	1.8222	0.6318	514.14	566.08		during	1.8353	0.6169	571.38	575.84
after	1.9807	0.7446	475.50	547.04		after	1.9693	0.7147	509.53	556.88

NoAR	Kurtosis	Skewness	Cmp	Avg Vel		NoAR	Kurtosis	Skewness	Cmp	Avg Vel
before	1.9125	0.6859	570.19	603.80		before	1.9674	0.7016	614.02	601.82
during	1.8467	0.6516	556.45	565.85		during	1.9672	0.7009	550.01	565.30
after	2.0548	0.7990	508.00	547.25		after	2.0585	0.7889	458.41	546.61

(a) Unweighted   (b) Weighted

At Mach 3, The input bulk velocity is 956 m/s, which matches best with the C_{mp} for the weighted $\epsilon = 75\%$. The unweighted C_{mp} values are all above the input velocity, as are the average velocity values. $\epsilon = 0\%$ and 75% have C_{mp} values below the input velocity, but the rest of the weighted values are above the input velocity. Kurtosis values are above the kurtosis values at Mach 1.5, which is expected because the distributions become thinner as Mach number increases. The skewness values before the shock are higher than Mach 1.5 skewness values, indicating that there are

78

Table 4.3:　Distribution Properties M=3

Bird	Kurtosis	Skewness	Cmp	Avg Vel
before	2.2735	0.9061	1012.04	1020.24
during	1.7173	0.5669	886.47	867.43
after	2.0991	0.8188	717.74	810.88

Eps00	Kurtosis	Skewness	Cmp	Avg Vel
before	2.2735	0.9061	1012.04	1020.24
during	1.7173	0.5669	886.47	867.43
after	2.0991	0.8188	717.74	810.88

Eps25	Kurtosis	Skewness	Cmp	Avg Vel
before	2.2041	0.8698	998.99	1020.01
during	1.7939	0.6288	902.10	867.18
after	2.0020	0.7578	718.47	810.05

Eps50	Kurtosis	Skewness	Cmp	Avg Vel
before	2.1292	0.8214	1021.60	1020.61
during	1.7081	0.5576	808.81	867.44
after	1.9053	0.6917	723.40	810.53

Eps75	Kurtosis	Skewness	Cmp	Avg Vel
before	2.1784	0.8536	1015.54	1020.06
during	1.7374	0.5838	862.12	868.19
after	2.0173	0.7688	737.52	810.34

Eps100	Kurtosis	Skewness	Cmp	Avg Vel
before	2.1602	0.8391	1059.76	1020.84
during	1.6658	0.5155	837.15	868.85
after	1.9002	0.6898	743.11	809.97

NoAR	Kurtosis	Skewness	Cmp	Avg Vel
before	2.2751	0.9130	985.30	1020.60
during	1.9210	0.7261	866.13	868.60
after	1.9625	0.7324	718.15	809.64

(a) Unweighted

Eps00	Kurtosis	Skewness	Cmp	Avg Vel
before	2.2935	0.8694	973.34	1028.29
during	1.6937	0.5318	821.83	880.43
after	2.0575	0.7817	664.48	834.05

Eps25	Kurtosis	Skewness	Cmp	Avg Vel
before	2.1639	0.8147	946.06	1022.88
during	1.7814	0.6018	777.59	876.20
after	1.9377	0.7209	749.10	832.71

Eps50	Kurtosis	Skewness	Cmp	Avg Vel
before	2.0127	0.7399	970.75	1021.79
during	1.6856	0.5314	817.97	880.94
after	1.8425	0.6478	694.03	834.73

Eps75	Kurtosis	Skewness	Cmp	Avg Vel
before	2.3998	0.9179	948.15	1025.41
during	1.7284	0.5603	890.15	881.62
after	1.9668	0.7309	686.00	834.12

Eps100	Kurtosis	Skewness	Cmp	Avg Vel
before	2.2380	0.8314	1007.92	1024.84
during	1.7015	0.5198	828.22	878.98
after	1.8340	0.6443	733.34	832.67

NoAR	Kurtosis	Skewness	Cmp	Avg Vel
before	2.2931	0.9259	977.51	1022.31
during	1.9245	0.7208	753.20	866.51
after	1.9591	0.7320	728.20	810.37

(b) Weighted

more particles traveling faster than C_{mp} at Mach 3 than Mach 1.5. The skewness of the distribution in the shock decreases compared to before the shock, and increases again after the shock.

In Table 4.4, the kurtosis is higher than the lower Mach numbers, as is expected. The skewness for all the results is very high before the shock, and within the shock drops to about half the before shock value. The unweighted distributions are beginning to exhibit more of a bimodal distribution within the shock, with the majority of

79

Table 4.4:   Distribution Properties M=6

Bird	Kurtosis	Skewness	Cmp	Avg Vel
before	3.0933	1.2717	1946.88	1944.65
during	1.8983	0.7060	1815.79	1588.58
after	2.0761	0.8065	1288.85	1453.75

Eps00	Kurtosis	Skewness	Cmp	Avg Vel		Eps00	Kurtosis	Skewness	Cmp	Avg Vel
before	3.0933	1.2717	1946.88	1944.65		before	2.8997	1.2031	1895.88	1942.54
during	1.8983	0.7060	1815.79	1588.58		during	1.8472	0.6502	1481.42	1597.09
after	2.0761	0.8065	1288.85	1453.75		after	2.0121	0.7684	1307.80	1497.80

Eps25	Kurtosis	Skewness	Cmp	Avg Vel		Eps25	Kurtosis	Skewness	Cmp	Avg Vel
before	2.6076	1.0729	1958.83	1944.69		before	2.5004	1.0153	1860.66	1947.59
during	1.8865	0.7025	1807.26	1588.67		during	1.8285	0.6486	1578.31	1606.84
after	1.9530	0.7288	1254.83	1454.14		after	1.8882	0.6871	1344.94	1497.11

Eps50	Kurtosis	Skewness	Cmp	Avg Vel		Eps50	Kurtosis	Skewness	Cmp	Avg Vel
before	2.7285	1.1255	1942.74	1945.64		before	2.8065	1.1458	1896.48	1943.76
during	1.7612	0.6013	1882.17	1588.42		during	1.6808	0.5348	1503.78	1603.75
after	2.1515	0.8533	1214.48	1453.14		after	2.0969	0.8212	1352.09	1498.16

Eps75	Kurtosis	Skewness	Cmp	Avg Vel		Eps75	Kurtosis	Skewness	Cmp	Avg Vel
before	4.3688	1.6862	1925.66	1944.99		before	4.3131	1.6639	1992.65	1948.26
during	1.8178	0.6536	1819.05	1590.00		during	1.7670	0.6030	1562.42	1607.37
after	2.0193	0.7705	1293.85	1453.81		after	1.9668	0.7386	1238.21	1496.06

Eps100	Kurtosis	Skewness	Cmp	Avg Vel		Eps100	Kurtosis	Skewness	Cmp	Avg Vel
before	3.0760	1.2700	1957.83	1944.77		before	3.0462	1.2378	1968.04	1949.94
during	1.8786	0.6971	1857.43	1592.88		during	1.8348	0.6540	1594.47	1602.79
after	1.9923	0.7532	1241.34	1453.60		after	1.9450	0.7225	1369.47	1496.01

NoAR	Kurtosis	Skewness	Cmp	Avg Vel		NoAR	Kurtosis	Skewness	Cmp	Avg Vel
before	3.1639	1.2992	1957.49	1945.07		before	3.3080	1.3231	1926.31	1947.13
during	1.8043	0.6449	1735.66	1592.13		during	1.7659	0.6102	1718.66	1584.39
after	2.0844	0.8128	1289.88	1452.84		after	2.0869	0.8141	1270.79	1451.10

(a) Unweighted   (b) Weighted

particles at the bulk velocity, which results in a slightly higher skewness compared to the weighted distributions. The C_{mp} values are closer to the bulk velocity compared to lower Mach numbers with the unweighted $\epsilon = 75\%$ value being closest to 1913 m/s followed closely by weighted NoAR. The average velocities match closely to the corresponding C_{mp} for each case, which is most likely due to the thin distributions at this Mach number.

Table 4.5:   Distribution Properties M=9

Bird	Kurtosis	Skewness	Cmp	Avg Vel
before	7.9963	2.5040	2920.43	2889.46
during	2.2365	0.8832	2836.36	2342.86
after	1.9950	0.7557	1879.09	2132.22

Eps00	Kurtosis	Skewness	Cmp	Avg Vel		Eps00	Kurtosis	Skewness	Cmp	Avg Vel
before	8.0031	2.5052	2920.43	2889.90		before	8.0371	2.5070	2854.28	2894.51
during	2.2259	0.8790	2840.32	2342.91		during	1.9988	0.7696	2312.20	2362.23
after	2.0709	0.8040	1885.12	2131.77		after	2.0230	0.7711	1857.28	2193.72

Eps25	Kurtosis	Skewness	Cmp	Avg Vel		Eps25	Kurtosis	Skewness	Cmp	Avg Vel
before	8.0031	2.5052	2920.43	2889.90		before	8.0371	2.5070	2854.28	2894.51
during	2.2259	0.8790	2840.32	2342.91		during	1.9988	0.7696	2312.20	2362.23
after	2.0709	0.8040	1885.12	2131.77		after	2.0230	0.7711	1857.28	2193.72

Eps50	Kurtosis	Skewness	Cmp	Avg Vel		Eps50	Kurtosis	Skewness	Cmp	Avg Vel
before	5.4030	1.9559	2861.51	2891.05		before	5.3606	1.9472	2813.49	2893.92
during	1.9425	0.7029	2823.89	2342.08		during	1.7342	0.5831	2453.08	2359.71
after	2.2519	0.9091	1789.82	2131.85		after	2.2049	0.8792	1999.04	2193.51

Eps75	Kurtosis	Skewness	Cmp	Avg Vel		Eps75	Kurtosis	Skewness	Cmp	Avg Vel
before	5.6947	2.0239	2922.12	2890.30		before	5.3905	1.9572	2938.74	2892.81
during	2.0237	0.7615	2840.26	2344.60		during	1.8209	0.6484	2247.58	2359.73
after	1.9517	0.7242	1830.55	2129.80		after	1.9092	0.6946	1961.83	2190.56

Eps100	Kurtosis	Skewness	Cmp	Avg Vel		Eps100	Kurtosis	Skewness	Cmp	Avg Vel
before	5.6799	2.0230	2892.93	2890.86		before	5.4770	1.9643	2909.62	2890.52
during	2.1203	0.8306	2731.01	2345.75		during	1.8761	0.7133	2486.22	2359.85
after	2.1727	0.8672	1971.78	2133.05		after	2.1322	0.8413	1942.71	2194.89

NoAR	Kurtosis	Skewness	Cmp	Avg Vel		NoAR	Kurtosis	Skewness	Cmp	Avg Vel
before	5.9486	2.0822	2895.75	2890.21		before	5.9833	2.0894	2878.54	2893.26
during	1.8620	0.6631	2737.73	2349.70		during	1.7779	0.6049	2323.30	2346.14
after	2.0118	0.7633	1873.70	2131.64		after	2.0070	0.7593	1846.73	2133.53

(a) Unweighted   (b) Weighted

The before shock values for kurtosis and skewness are much higher compared to previous Mach numbers and the weighted and corresponding unweighted distributions have very similar values. Within the shock, skewness is again higher for the unweighted distributions. The C_{mp} values before the shock are fairly close to the average velocities, with the exception of the SAR cases previously discussed. The C_{mp} value closest to the input velocity of 2867 m/s is the weighted NoAR value of 2878 m/s. The bimodal distribution seen with the unweighted distributions leads to a lower

81

average velocity compared to the most probable velocity. Evaluating these velocity distributions have allowed for a better understanding of the microscopic behavior of the particles, and the change of the behavior when using SAR and NoAR. Through the shock, the number of collisions as calculated in Bird's code is obviously too low, which causes a longer equilibration thereby making the shock layer thicker compared to experimental data.

4.4 2d Axisymmetric Hollow Cylinder Results

The DSMC2A code was used for a variety of analyses: density plots compared to Davis' experimental data, percent difference contour plots, surface plots, contour plots, and the cell size was reduced to one quarter the original size with results were compared to Davis' data. Before viewing the results in comparison to experimental data, the contour plots should be investigated so that the overall flowfield is understood. Since density is the primary flowfield parameter investigated in this project, it should be the first one discussed. There are only slight variations in the flowfields between Bird, SAR, and NoAR, so only Bird, $\epsilon = 0\%$, $\epsilon = 100\%$, and NoAR will be shown in this section.

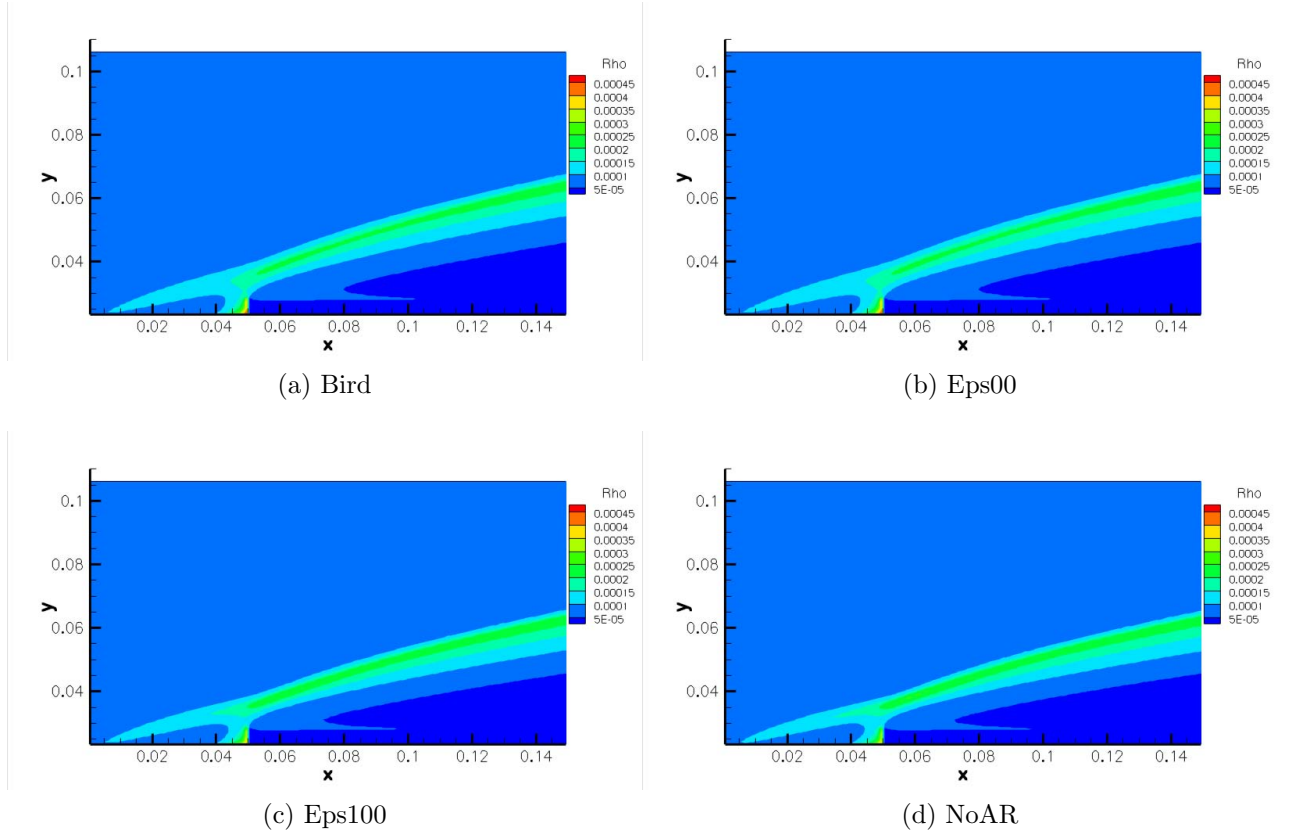(a) Bird

(b) Eps00

(c) Eps100

(d) NoAR

Figure 4.53:   Density Contour Plots

The stagnation point is very visible in Figure 4.53 for all the cases, as is the shock layer. Only very slight variations in the shock layer can be seen when comparing

the cases. NoAR results in a shock layer closer to the step that appears to be thicker than Bird's shock layer. The temperature plots are also very similar to each other in Figure 4.54.

(a) Bird

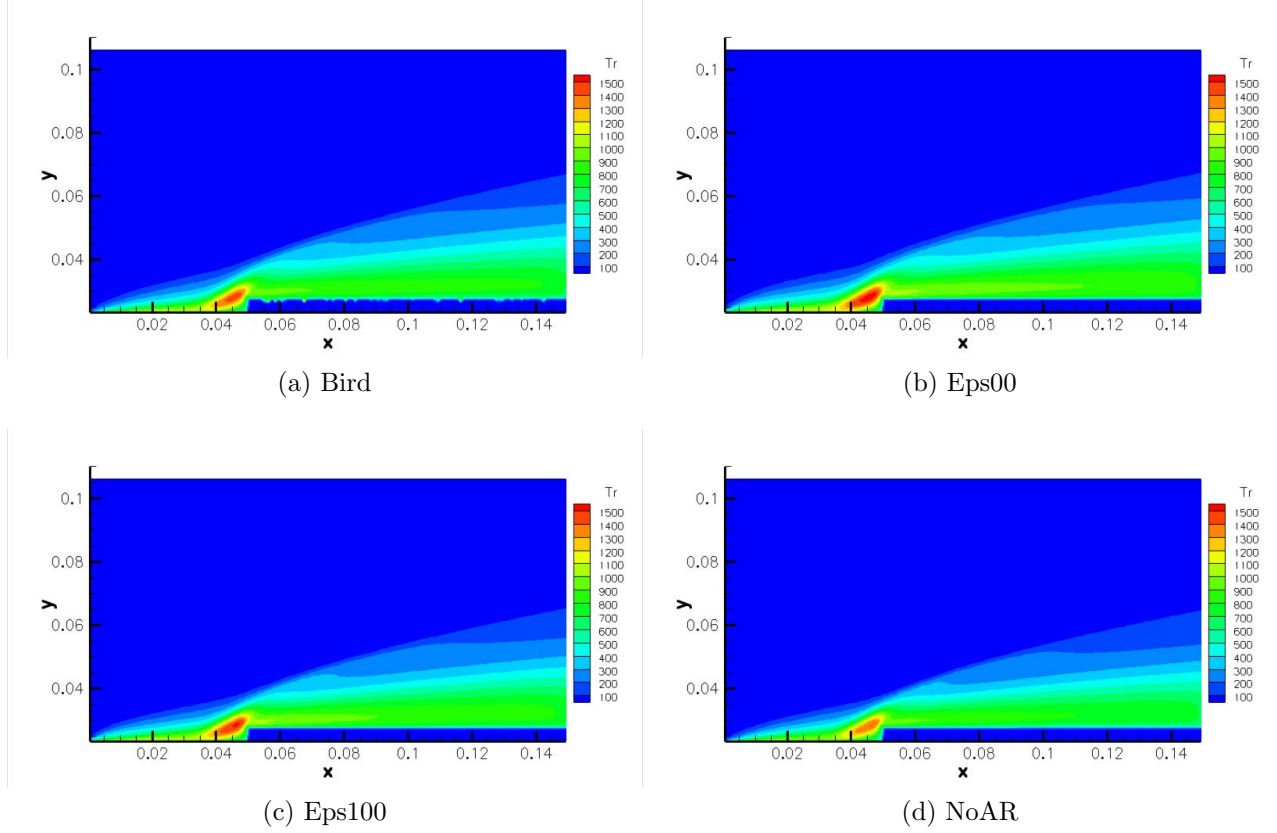(b) Eps00

(c) Eps100

(d) NoAR

Figure 4.54:   Translational Temperature Contour Plots

An area of hot gas can be seen before the step in Figure 4.54, where the shock layer and boundary layer are converging. The size and temperature of that area varies with algorithm. The shock layer above the step can also be seen, with minor changes for each case. Note that on the horizontal face of the step in Bird's case, the step does not seem flat: there are pockets of hot air throughout the length of the step. The issue on the step is due to low populations of particles in the cells in that area, which causes statistical errors. The SAR and NoAR cases do not suffer the same problem, even though they also have few cells behind the shock along the horizontal face of the step, which will be shown shortly.
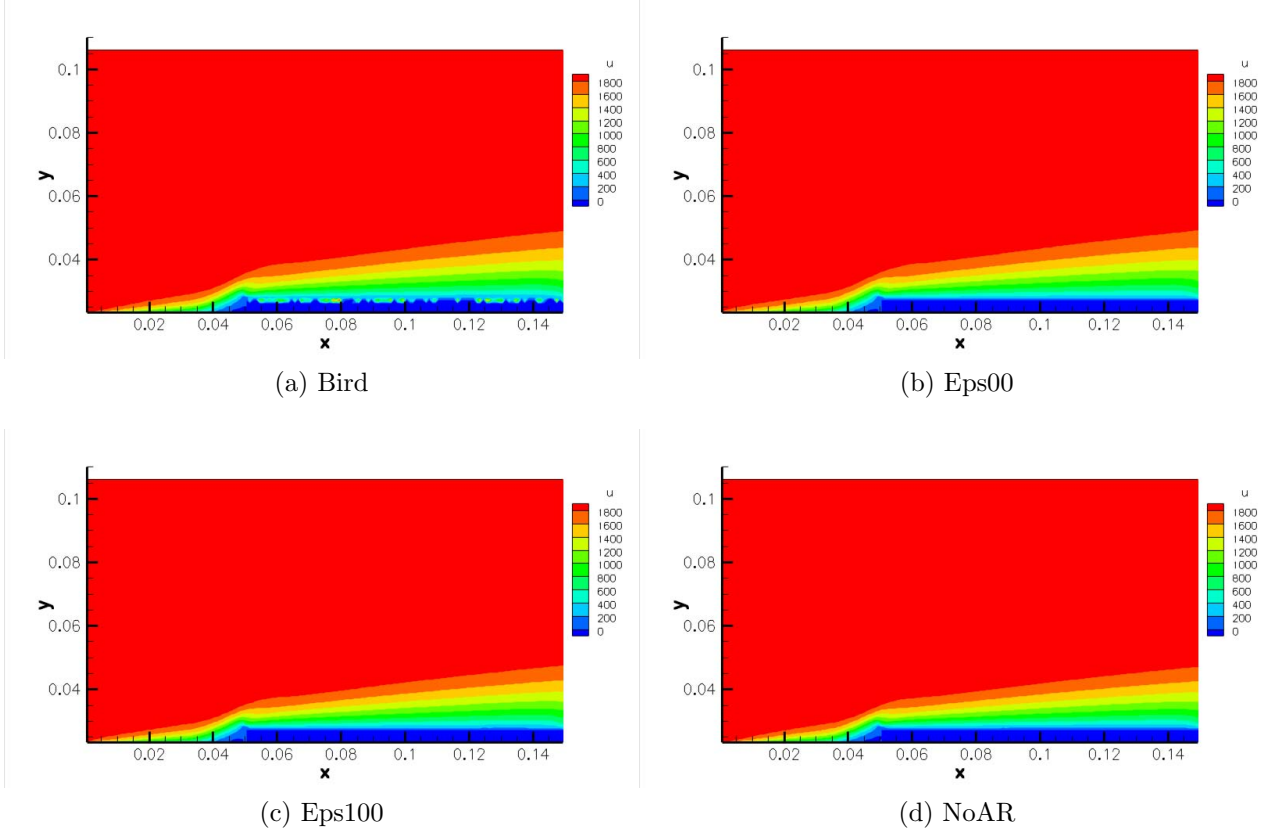
84

(a) Bird

(b) Eps00

(c) Eps100

(d) NoAR

Figure 4.55:   U-Velocity Contour Plots

In Figure 4.55a, the same problem along the top of the step can be seen again, but it is not seen with SAR and NoAR. In order to show the amount of rarefaction in each cell, these cases were run again and the number of particles per cell was printed out to a file.

As seen in Figure 4.56, the number of particles is less than 10 on the horizontal face of the step. In the stagnation region, the number rises to about 40 particles, and in the shock layer the number of particles increases even more to approximately 60 particles. The flowfield makes choosing a ratio of simulated particles to real particles a difficult one. If the ratio is too small, the rarefied areas of the flow become even more rarefied, leading to errors. If the ratio is too large, particles will collide more than once per time step in stagnation regions and in the shock layer and the assumption of decoupled particle collisions and motion is no longer valid. SAR and NoAR provide

85

(a) Bird

(b) Eps00

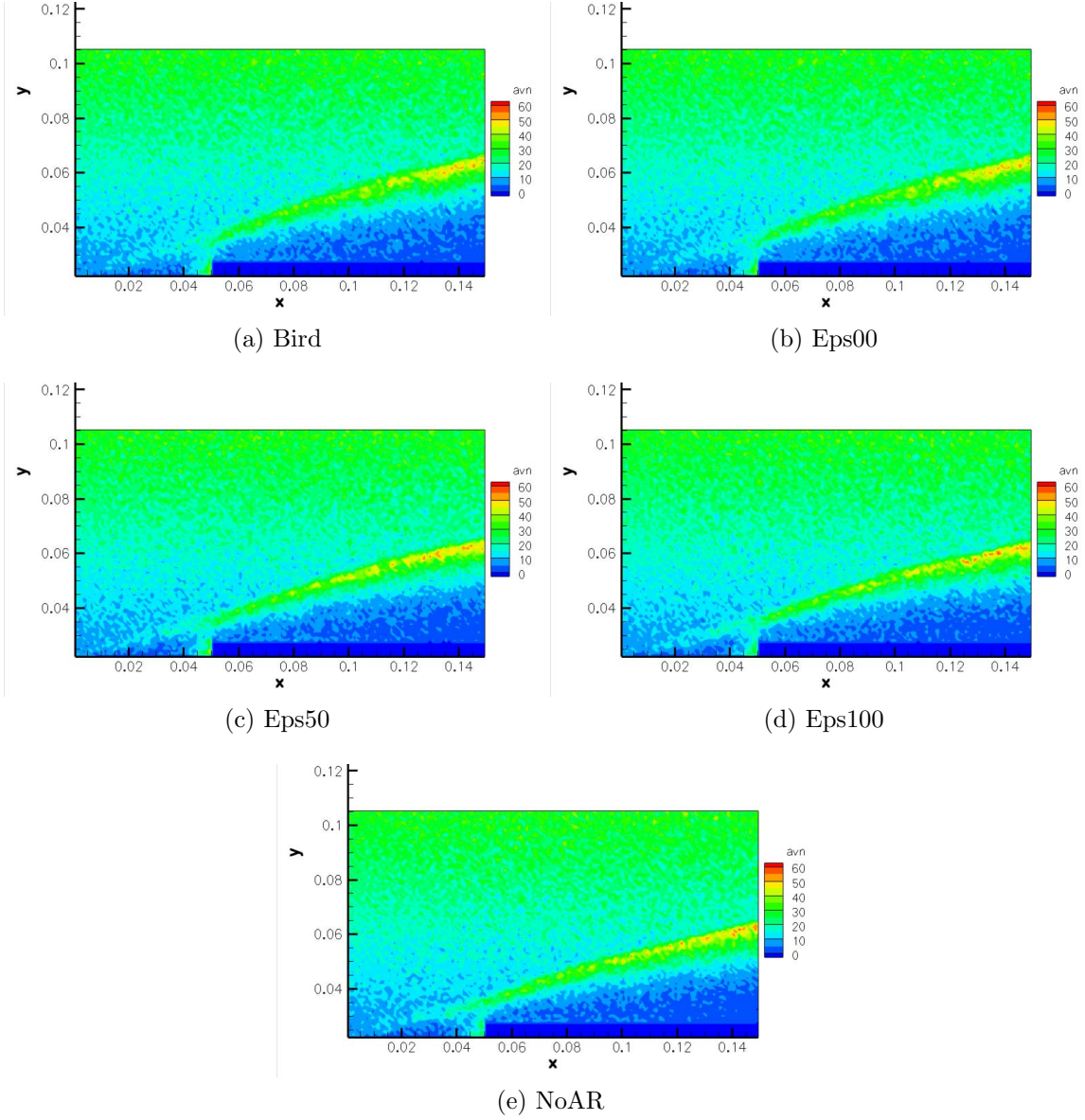(c) Eps50

(d) Eps100

(e) NoAR

Figure 4.56:   Average Number of Particles Per Cell

good results, even in areas of higher rarefaction, which is an important point to consider. The sampling algorithm in SAR and NoAR is most likely what causes the change, since $\epsilon = 0\%$ results do not have the same problem as Bird's results even though their accept/reject criteria are identical. The weighting algorithm in SAR and NoAR most likely changes the variance significantly in these low populated regions, and allows for the flowfield properties to be correctly sampled.

4.4.1 Comparison to Davis' Experimental Data. Previous comparison to experimental data showed that the NoAR and Bird results were usually the extrema with the SAR values in between with the 0% case closest to Bird and higher ϵ values tending toward NoAR [11]. The density profile results from the current simulation shows the same trend.
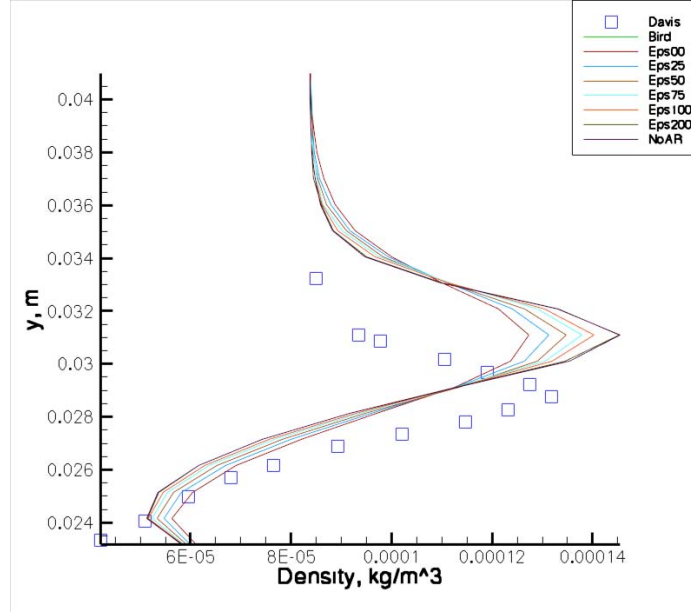

Figure 4.57: Density Profile at x=.0313m

In Figure 4.57, the profile data is taken .0187m upstream of the step. All the cases result in a shape that is fairly similar to the experimental data, but SAR with $\epsilon = 50\%$ is matches best with the change in density. Throughout the profile Bird and $\epsilon = 00\%$ match, which is why Bird's green line does not appear.
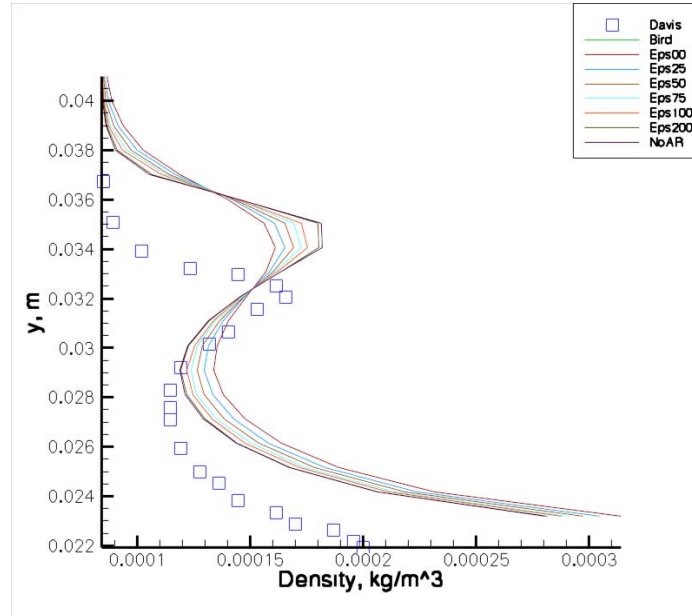
Figure 4.58:   Density Profile at x=.0462m

Again, all the cases provide results that have the same shape, but $\epsilon = 50\%$ has the same change in density at y=0.032 m. None of the computational results match the solution closer to the wall, but NoAR and the high ϵ value of 200% are the closest.
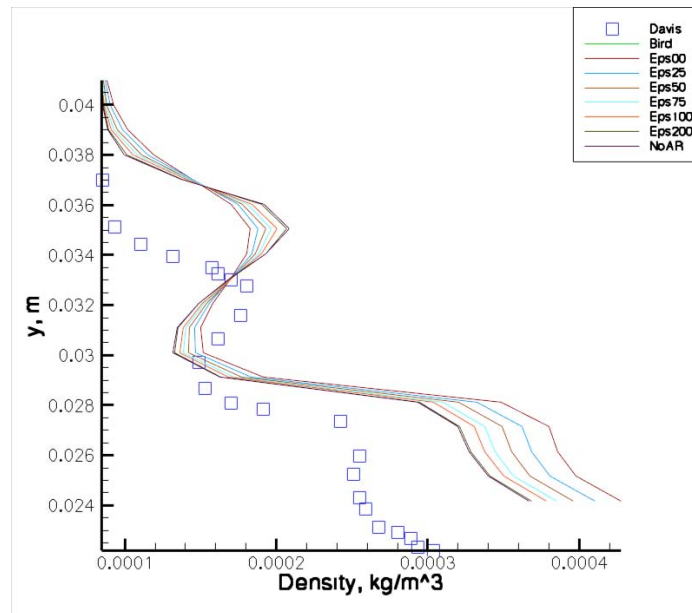
Figure 4.59:   Density Profile at x=.0495m

At the step, the $\epsilon = 25\%$ value is closest to the density peak at y= 0.033 m, and NoAR and $\epsilon = 200\%$ match the best closest to the wall. All the computational results match the overall behavior of the density profile.

Figure 4.60:   Density Profile at x=.0509m

Past the stagnation point in Figure 4.60, the density profile is similar to the first profile at x=0.0313 m. The change in density is larger, as the shock is stronger after the step. Again, just after the step $\epsilon = 25\%$ matches best with the change in density.
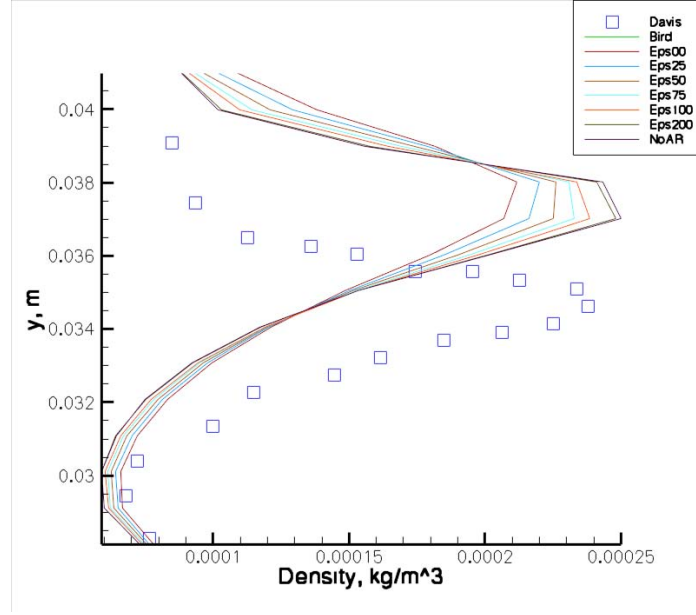
Figure 4.61:   Density Profile at x=0.0561m

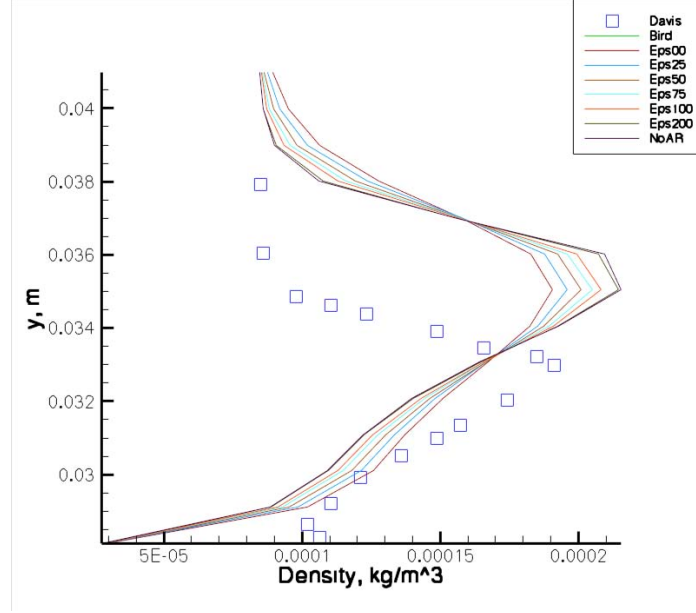The shock is even stronger 6 mm downstream from the step, as shown by the change in density at x=0.0561 m in Figure 4.61. Farther downstream from the step, the change in density most closely matches with $\epsilon = 100\%$. Below y=0.034 m, Bird and $\epsilon = 0\%$ match the best to the experimental plots. None of the plots show good agreement near the wall, which may be due to the specular boundary condition in DSMC2A. At a molecular level, the surface of the cylinder will not be completely flat, which means that a specular boundary condition is not realistic.

In an effort to see why different ϵ values match at different points on the profile, temperature and velocity plots have been created. These plots can be compared to the density plots for an overall understanding of the fluid at the sampling locations.

(a) Velocity
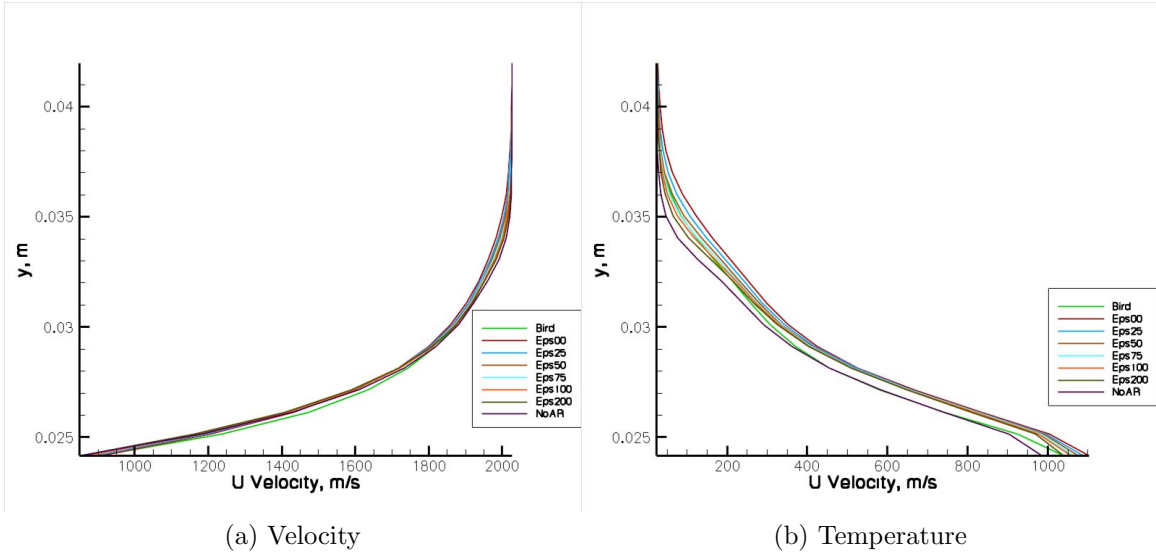
(b) Temperature

Figure 4.62:   Velocity and Temperature Profiles at x=0.0313m

The shock layer is not very visible in the velocity profile, which matches the velocity contour plot. The boundary layer is very clear in the velocity profile, however. The temperature profile shows a slight change in the temperature gradient at 0.029 m, which is the peak of the density profile. The temperature gradient changes again at approximately y=0.025 m, which is where an inflection point in the density profile exists.

(a) Velocity
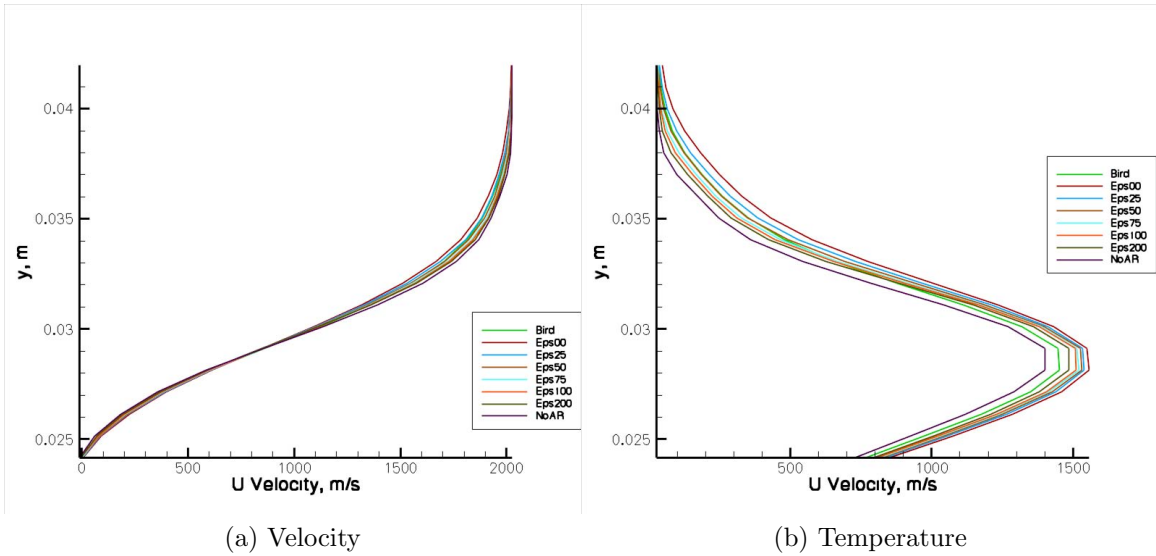
(b) Temperature

Figure 4.63:   Velocity and Temperature Profiles at x=0.0462m

The velocity profile at x=0.0462 m has the beginnings of what looks to be an unfavorable gradient, which occurs before the boundary layer separates from the wall, or in the case of this experiment, as the flow moves toward a stagnation point. The temperature profile has an inflection point at y=0.03 m, which matches one of the inflection points in the density profile.

(a) Velocity
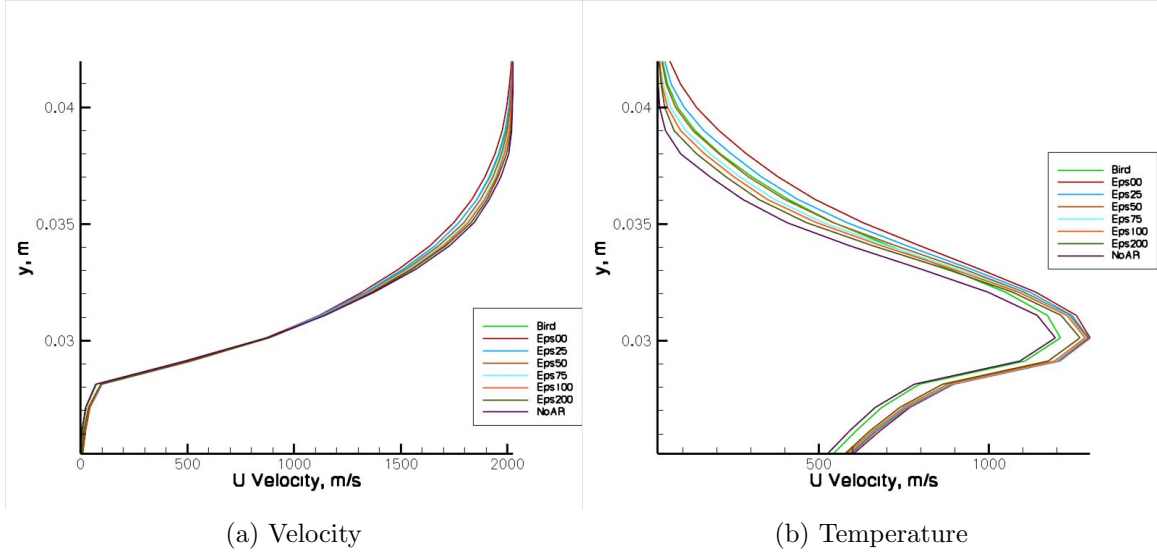
(b) Temperature

Figure 4.64:   Velocity and Temperature Profiles at x=.0495m

The velocity profile very clearly shows a stagnation region below y=0.028 m. Again, the inflection point in the temperature profile corresponds to the second inflection point in Figure 4.59.

(a) Velocity

(b) Temperature

Figure 4.65:   Velocity and Temperature Profiles at x=.0509m

After the step, the velocity profile returns to a normal boundary layer velocity profile. Interestingly, the temperature profile in Figure 4.65 has an inflection point that does not match the simulated results, but it does match the experimental inflection point.

(a) Velocity

(b) Temperature
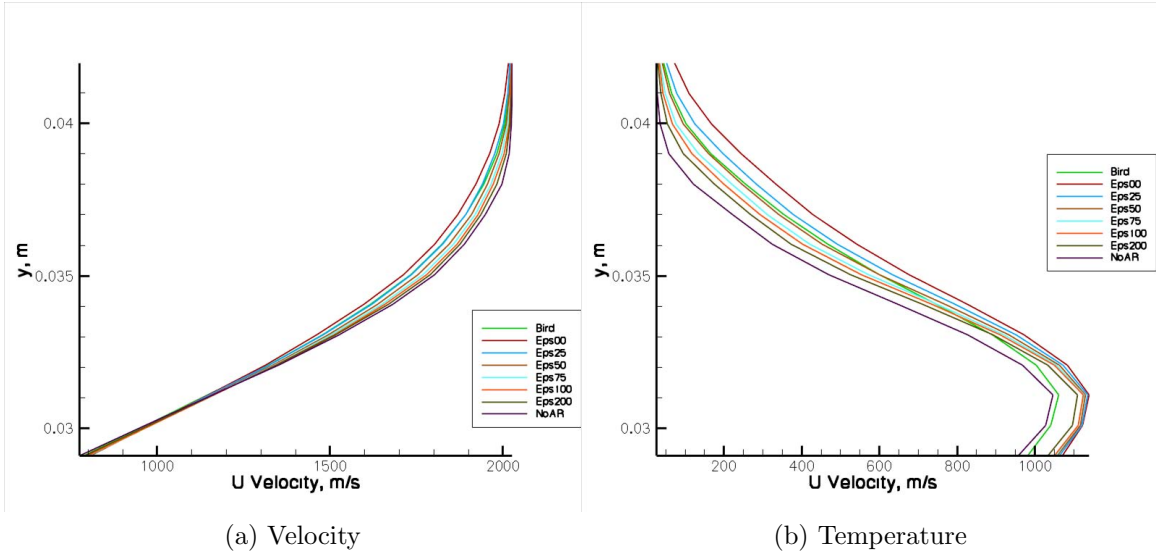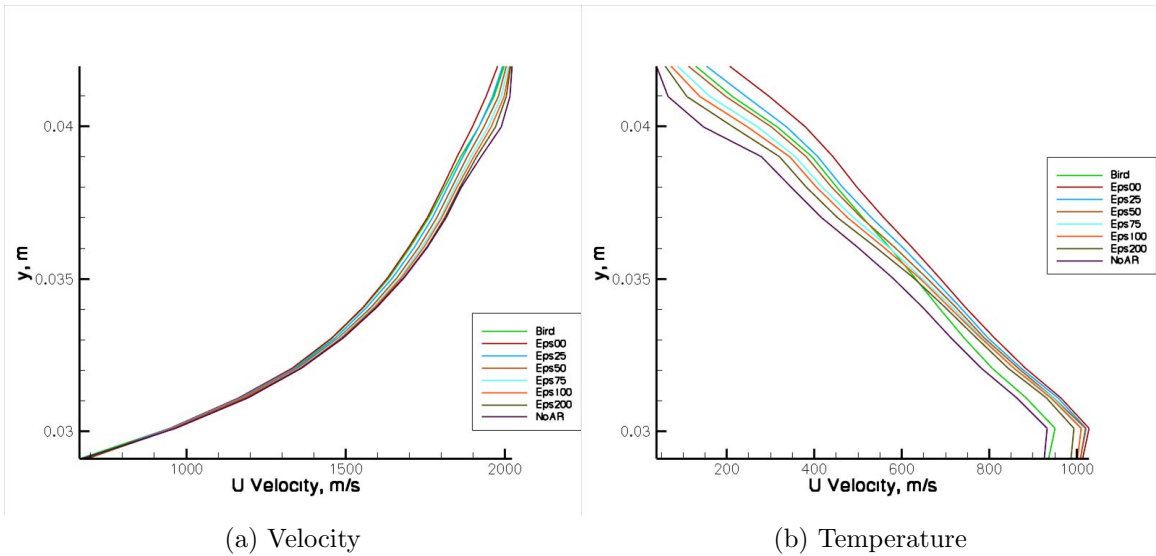
Figure 4.66:   Velocity and Temperature Profiles at x=.0561m

93

The last velocity profile shows a higher boundary layer, and the temperature profile has an inflection point that again matches the density profile's inflection point.

All of the plots show that the computational results match the same behavior as the experimental profiles. The computational results tend to be approximately 0.003 m higher than the experimental results, which could easily be explained by uncertainty of the experimental data. Uncertainty of the experimental data and the conversion of the graphical data from Davis' thesis to plots is significant, and therefore the comparison of the experimental data to the simulations is considered reasonable. However, due to the uncertainty associated with the experimental data, it it very difficult to definitively say that one algorithm is better than the other. Rather, the DSMC2A results should be used to show that the SAR and NoAR algorithms display similar behavior in a 2-dimensional axisymmetric program as they do in the 1-dimensional shock program.

4.4.2   Quarter Cell Size Cases.   In Bird's book, it is suggested that the cell size be on the order of the mean free path [4]. The cell size for the original case is approximately 1 mm by 1 mm while the mean free path is 0.47 mm. The cell sized was reduced to 0.5 mm by 0.5 mm to see if the results compared to Davis can be further refined.
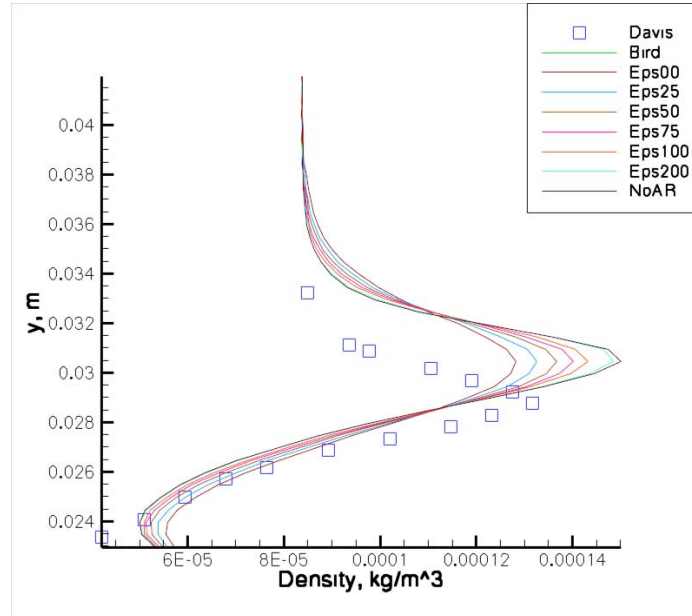
Figure 4.67:   Density Profile at x=.0313m

The first profile shows that the SAR value that would compare best to the experimental data is between ϵ values of 25% and 50%, which is slightly lower than the original results.
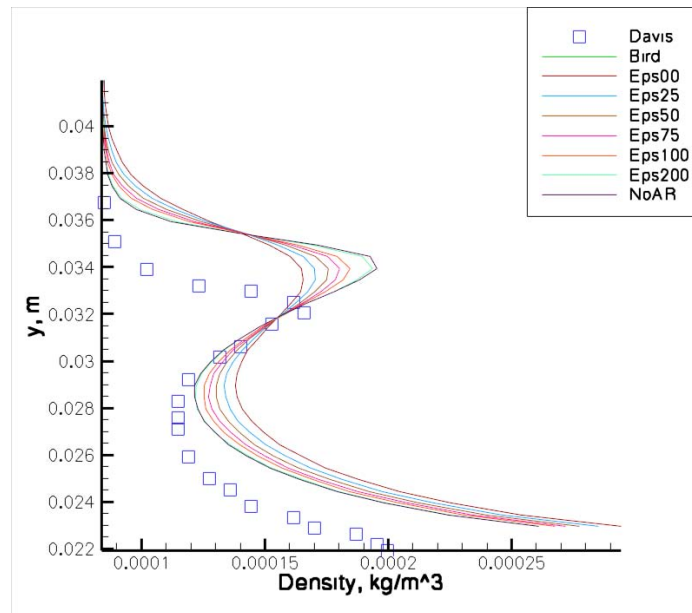
Figure 4.68:   Density Profile at x=.0462m

Figure 4.68 compares best with 25% at the peak which is again less than the original grid. NoAR is closest below the peak.
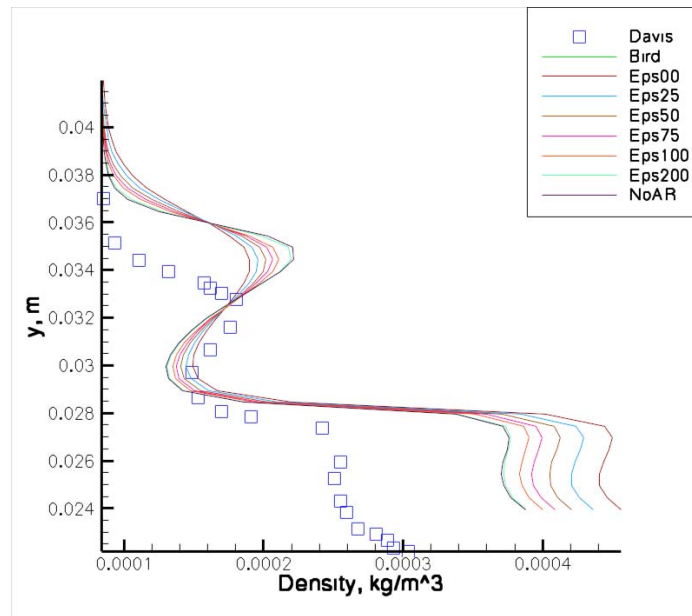
Figure 4.69:   Density Profile at x=.0495m

Figure 4.69 compares best with Bird and 00% at the peak, and below the peak NoAR compares the best. Note that the exaggerated behavior of the computational results compared to experimental results still exists.
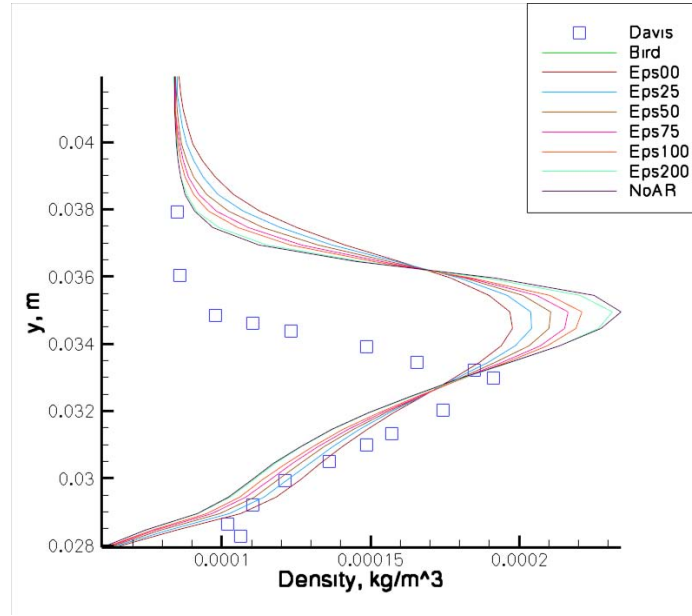
Figure 4.70:   Density Profile at x=.0509m

Again, Bird and 00% match best with the profile just after the step, while 25% matches best for the original grid. Below the peak, more of the cases are closer to experimental data compared to Figure 4.60.
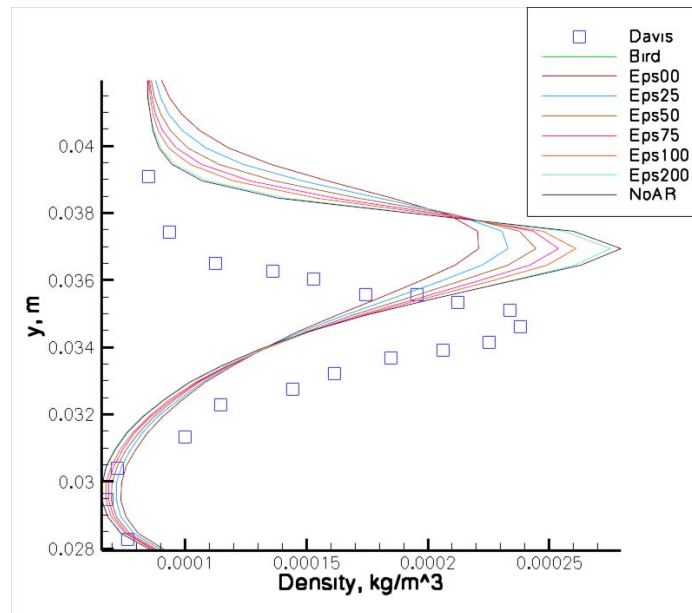
Figure 4.71:   Density Profile at x=.0561m

The last profile, which is taken well downstream of the step, matches closest with 50% at the peak, and NoAR closer to the wall. The original grid matches closest with $\epsilon = 100\%$.

The smaller grid consistently required a smaller ϵ value to match the results. Since the ratio of simulated particles to real particles was increased proportionally to the decreased size of the cells, the collision ratio and variance stayed approximately the same. This study consists of comparing to experimental data with one Mach number, which does not allow for further research into the Mach number dependency for the ϵ input value. The important lesson from this study is that reducing the cell size to the length of the mean free path does significantly change the ϵ value that matches experimental data through the shock layer. The addition of more cells and increase in the ratio of particles caused the computational time to grow significantly. Each of these cases took approximately 3 days to complete, compared to less than half a day for the original grid. The smaller grid will provide a more refined solution, but may not be worth the additional computational time to get the better solution.

4.4.3 Percent Difference Contour Plots. Contour plots of the flowfields have been shown earlier in this section in order to show the differences between the results of the cases. It is difficult to see all the differences with these contour plots, however. The percent difference plots allow for a better understanding of the changes in the flowfield for SAR and NoAR compared to Bird's output. The percent difference contour plots were created for density, temperature, and u-velocity. The contour plots of percent difference for density for each of the cases is plotted in Figure 4.72.

In Figure 4.72a, all the cells have a value of zero, indicating that the flowfield exactly matches that of Bird, which make sense since density is not sampled using the weightings from SAR and they have the same accept/reject criteria. There are large differences in density in the shock layer, and along the horizonontal face of the step, where issues with Bird's results have previously been noted. The differences increase with higher ϵ values, with NoAR providing the largest differences. The areas of large
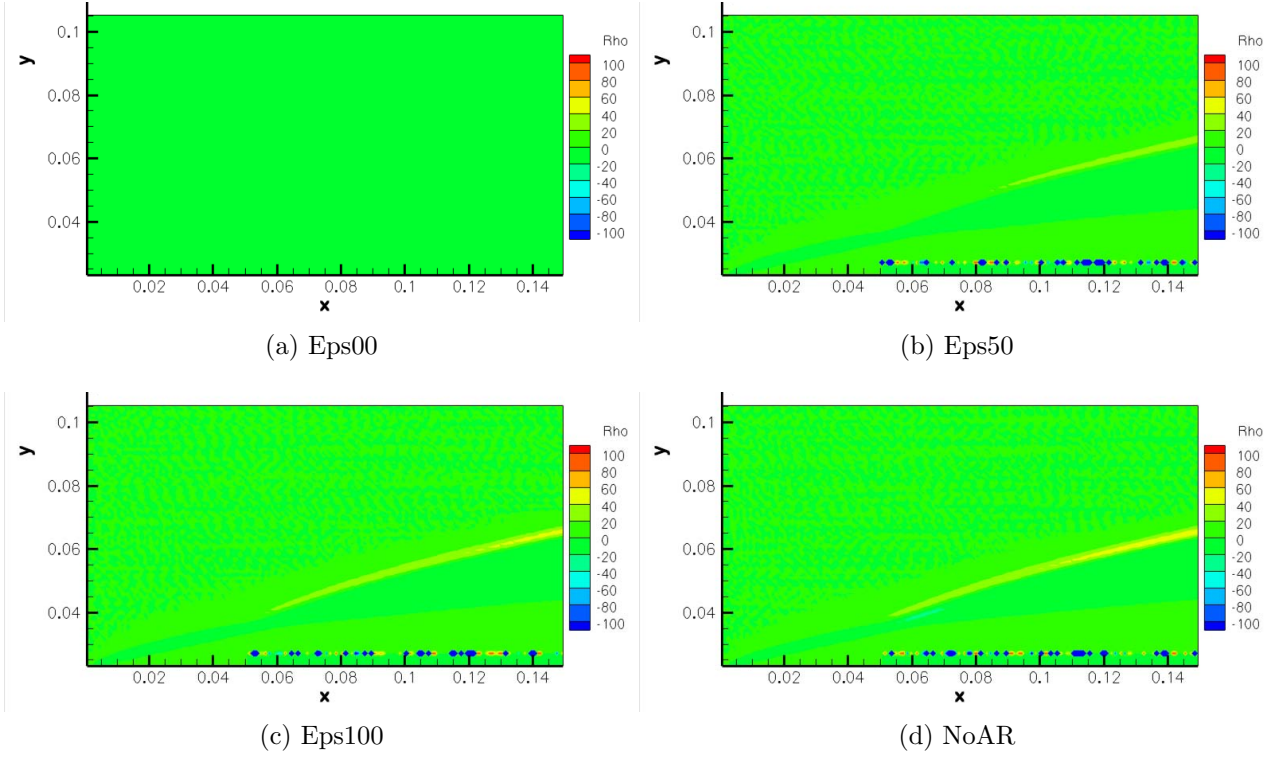
Figure 4.72:   Percent Difference Density Contour Plots Compared to Bird

differences along the horizontal face of the step is due to an issue with DSMC. The number of particles in the area behind the shock along the step is very small, which results in a large amount of variance and causes problems with the correct simulation at that location. Temperature is investigated next.

The largest temperature differences in Figure 4.73 are found at the leading edge of the hollow cylinder where the shock layer begins and throughout the shock layer. As the ϵ value increases, so do the differences between Bird and the SAR case. NoAR shows the greatest difference compared to Bird. The SAR results show negative differences, especially near the leading edge of the cylinder, while the NoAR results does now show any negative differences. The red rectangle is the step that is attached to the hollow cylinder. Note there is not a large difference in the boundary layer, even though it is a region of nonequilibrium. The amount of nonequilibrium in the boundary layer is much smaller than the amount found in the shock associated with this flowfield.
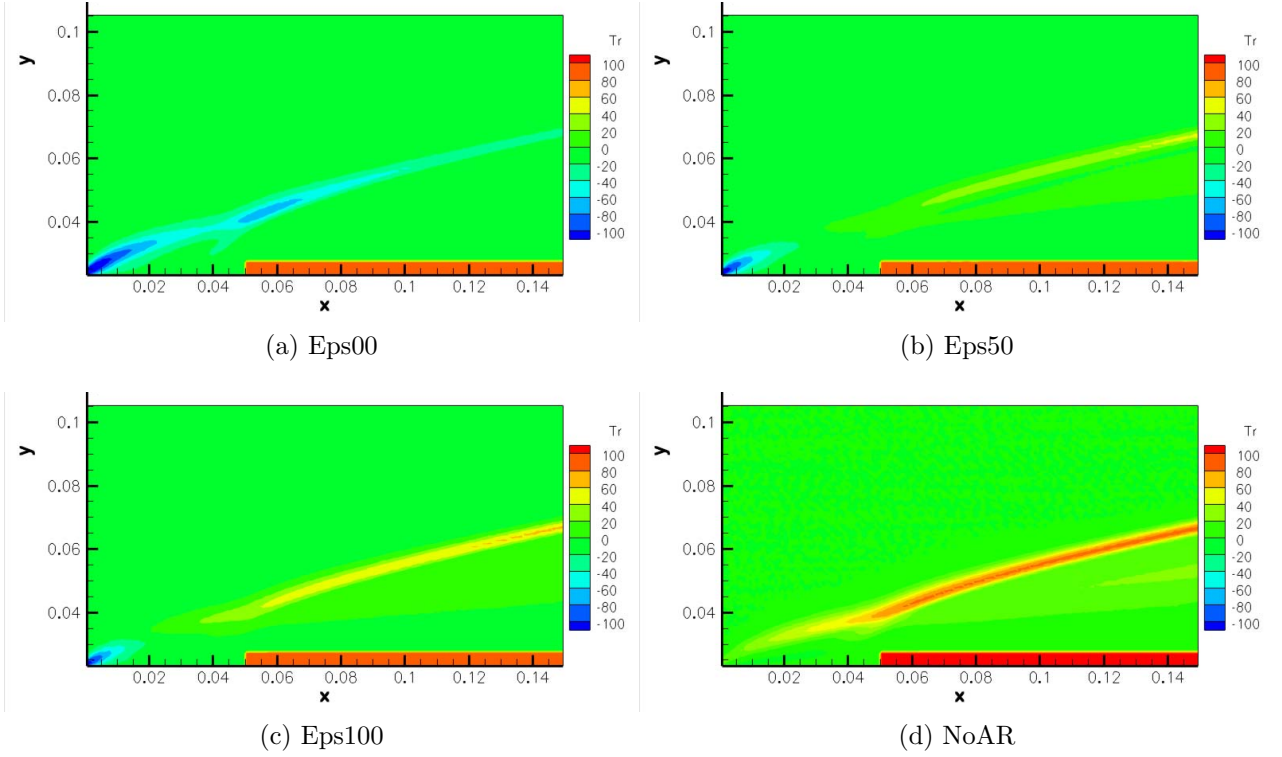
Figure 4.73:   Percent Difference Temperature Contour Plots Compared to Bird

Most of the flowfield matches Bird's results well for u-velocity, and the largest differences are found at the stagnation point. Figure 4.75 focuses on the stagnation region in order to better view the differences in that area.

Interestingly, NoAR shows the least amount of difference compared to Bird in the stagnation region in Figure 4.75. The SAR values all show very similar differences, but $\epsilon = 0\%$ shows the most difference and $\epsilon = 100\%$ shows the least of the SAR cases. The two changes made to the code involve the accept/reject criteria, which affects the collision rate, and the flowfield sampling. Flowfield sampling does not affect the surface values, so the percent difference for surface properties should also be looked at to evaluate the changes to the system due to the accept/reject criteria alone.

As would be expected, in Figure 4.76, the $\epsilon = 0\%$ case shows no difference from Bird's results. The only difference between Bird and $\epsilon = 0\%$ is the sampling, but since sampling doesn't affect the surface values, they have the same results. Both

(a) Eps00   (b) Eps50

(c) Eps100   (d) NoAR
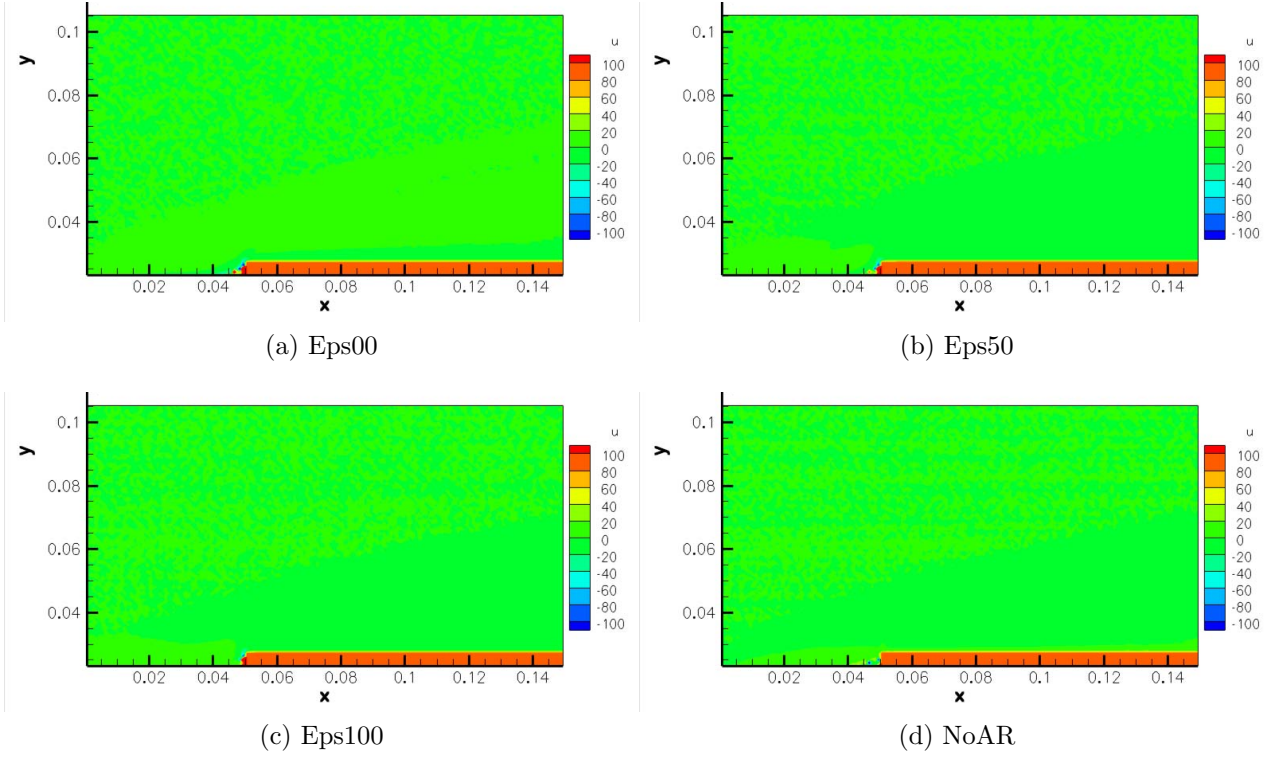
Figure 4.74:   Percent Difference U-Velocity Contour Plots Compared to Bird

plots show that NoAR is the most different from Bird and the SAR results are between Bird and NoAR. The vertical face shows a maximum difference of about 16% and the horizontal face shows a maximum difference of 18%. The differences on the surface are much smaller than the difference in the temperature flowfield values, which range from -160% to 80%, which proves that sampling has a more more profound effect on the results of the simulation than SAR does.

4.4.4   Surface Plots.   Surface plots for incident pressure, incident translational temperature, and heat flux have also been graphed for both the horizontal and vertical faces of the step. These plots can be used to help understand the effect of the SAR and NoAR algorithms on the surfaces.

(a) Eps00   (b) Eps50

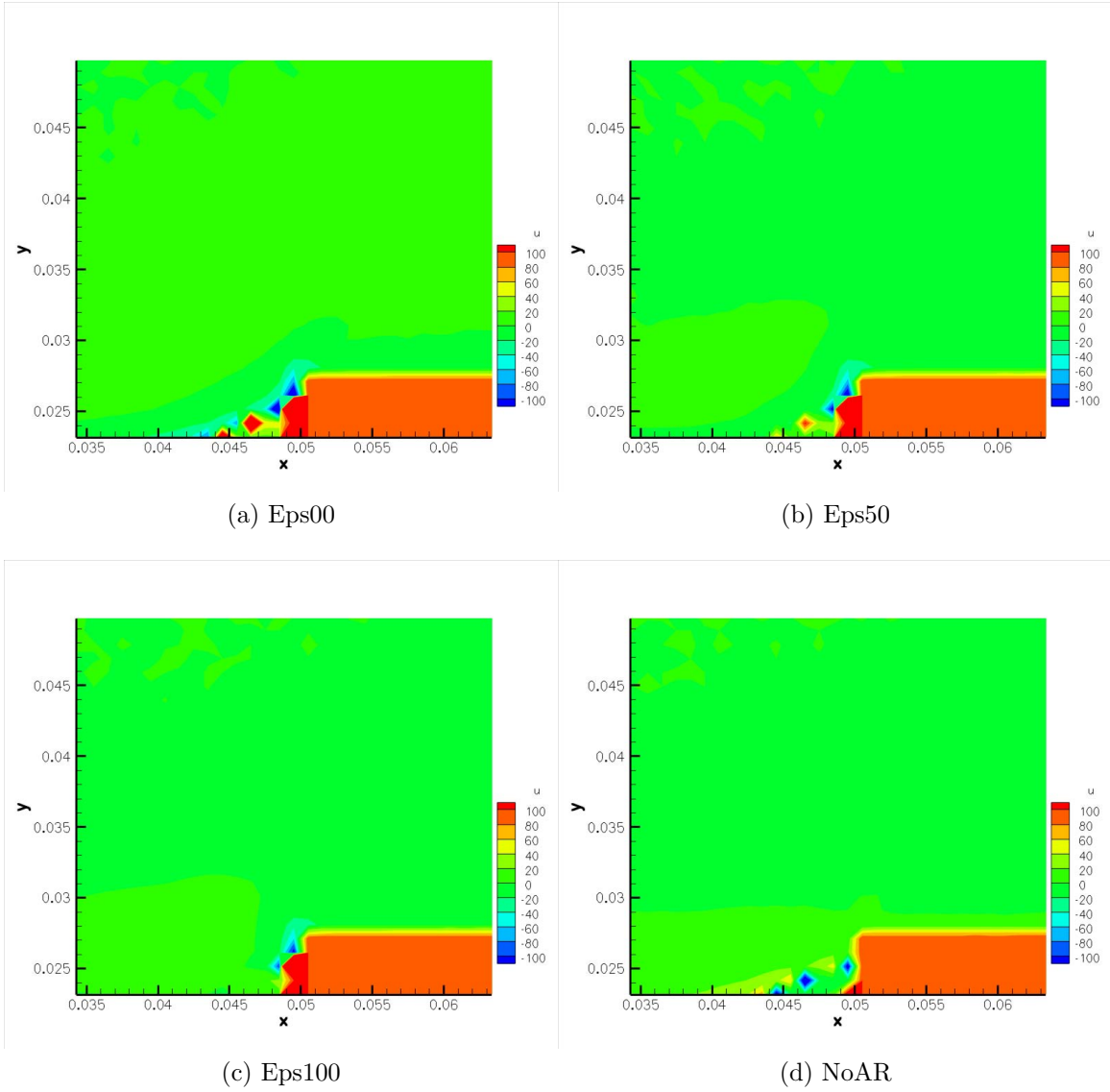(c) Eps100   (d) NoAR

Figure 4.75:   Percent Difference U-Velocity Contour Plots Compared to Bird

The vertical face of the step causes a stagnation point where it meets the edge
of the hollow cylinder. Heat flux is a function of the temperature gradient, so it makes
sense that the heat flux in Figure 4.77c follows the profile of the incident temperature
in Figure 4.77b.

(a) Vertical Step Surface   (b) Horizontal Step Surface
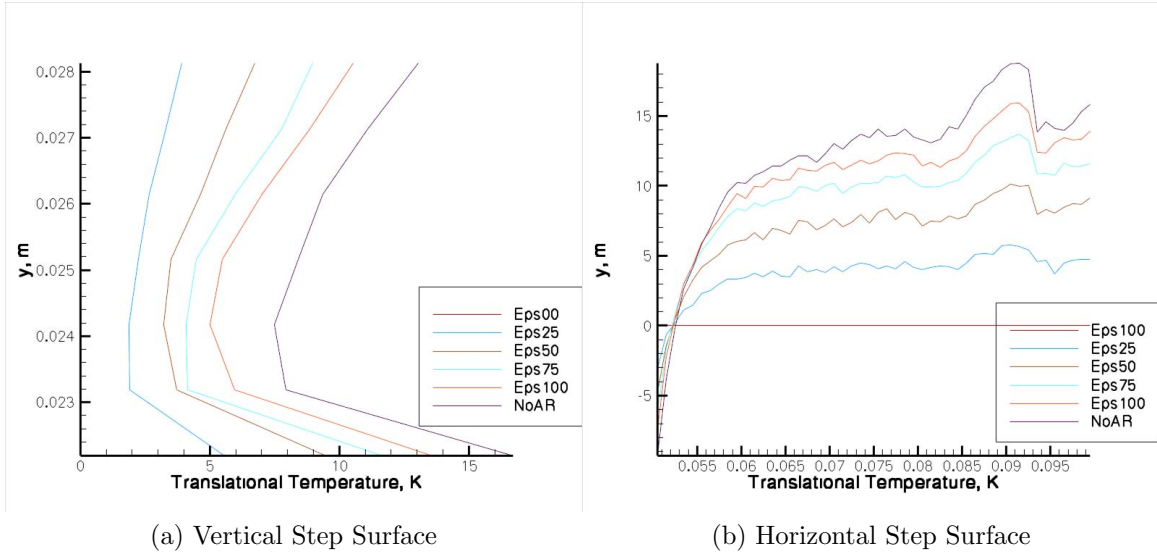
Figure 4.76:   Surface Percent Difference Plots

The horizontal surface shows a slight increase in incident pressure just after the step, followed by a steady decrease until x=0.08m when there is a sudden spike followed by drop in pressure. The same behavior can be seen in all of the profiles in Figure 4.78.

4.4.5 Velocity Distributions.   Now that the macroscopic properties have been discussed, the velocity distributions for Mach numbers 1, 3, 6, and 9 will be shown. The DSMC2A cases cannot be compared to a theoretical distribution like the 1d cases. The 2-dimensional axisymmetric flowfield is much more complicated, with a shock layer, a circulation region, a stagnation region, and a boundary layer. These flowfield effects are associated with a change in bulk velocity, and there is not a way to calculate what the bulk velocity should be in each of these cells. Therefore, the SAR and NoAR speed distributions will be compared to Bird only, without the theoretical distribution at each of the sampled cells. The sample cells are located in the stagnation region, boundary layer, shock layer, and behind the shock.

As with the 1-dimensional results, the unweighted distributions are on the left and the weighted are on the right for all of the figures. Bird's distribution is plotted

103
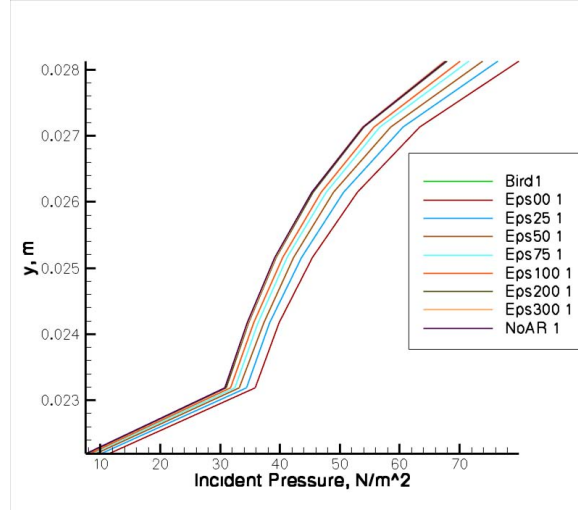
(a) Pressure
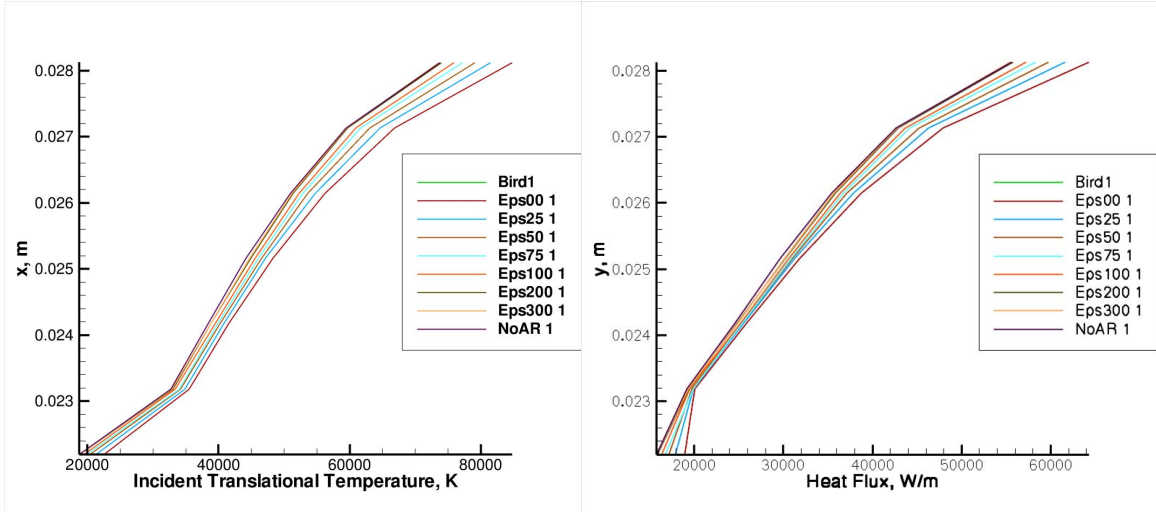
(b) Temperature

(c) Heat Flux

Figure 4.77:   Surface Plot for Front Face of Step

in the background of all of the plots for comparison. In Figures 4.79 and 4.80, the distributions were taken at the stagnation region. The stagnation region show particle velocities that are slower than the bulk velocity, which is 2000 m/s, so the distribution is to the left of the bulk velocity. The unweighted $\epsilon = 0\%$ distribution is nearly identical to Bird, which is expected since they have the same accept/reject criteria. The weighted $\epsilon = 0\%$ distribution shows only slight differences compared to Bird, as do the weighted and unweighted $\epsilon = 50\%$ distributions.
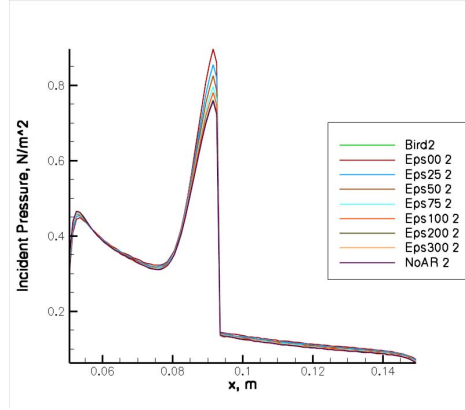
(a) Pressure
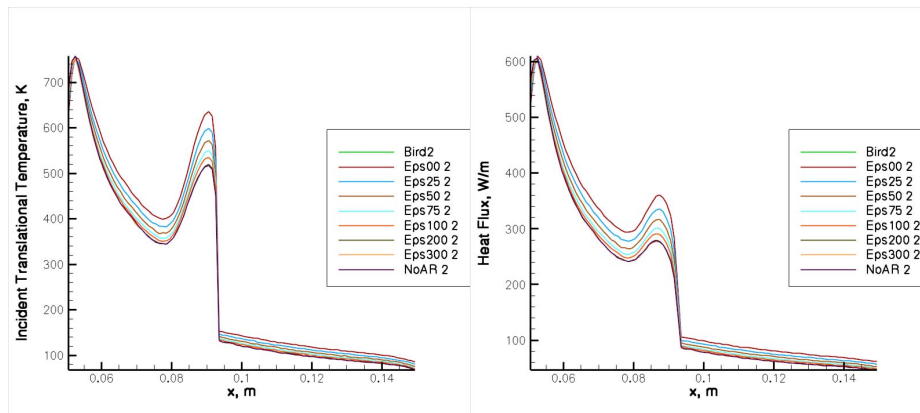
(b) Temperature

(c) Heat Flux

Figure 4.78:   Surface Plot for Horizontal Face of Step

In Figure 4.80, the $\epsilon = 100\%$ distributions are again very similar to Bird, and the NoAR distributions are the most different from Bird, as would be expected.

Unweighted Particle Velocity at N=350 –Eps00

(a) Unweighted Eps00

Weighted Particle Velocity at N=350 –Eps00

(b) Weighted Eps00

Unweighted Particle Velocity at N=350 –Eps50

(c) Unweighted Eps50

Weighted Particle Velocity at N=350 –Eps50

(d) Weighted Eps50
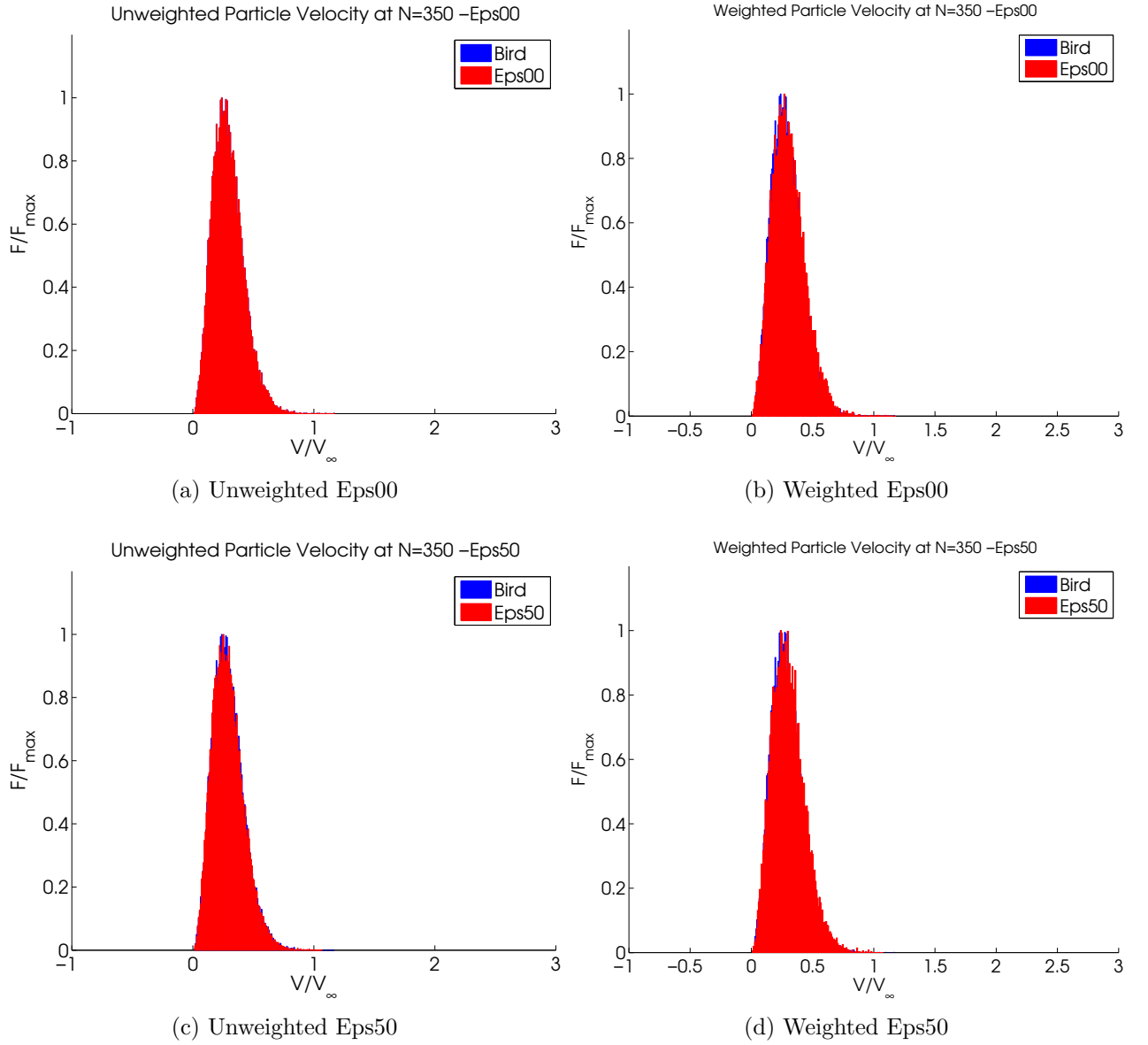
Figure 4.79:   Velocity Distributions for DSMC2A Case in Stagnation Region

Figure 4.81 shows a slightly wider distribution than was seen in the stagnation region, and the weighted $\epsilon = 0\%$ and both of the $\epsilon = 50\%$ cases are fairly similar to Bird. All of the distributions are more jagged than what was observed with the 1-dimensional cases, indicating that the number of particles are fewer in this sample cell. The peaks of the distributions before the step appear to be farther to the right compared to the distributions at the stagnation point, which means that the particles

(a) Unweighted Eps100

(b) Weighted Eps100

(c) Unweighted NoAR

(d) Weighted NoAR
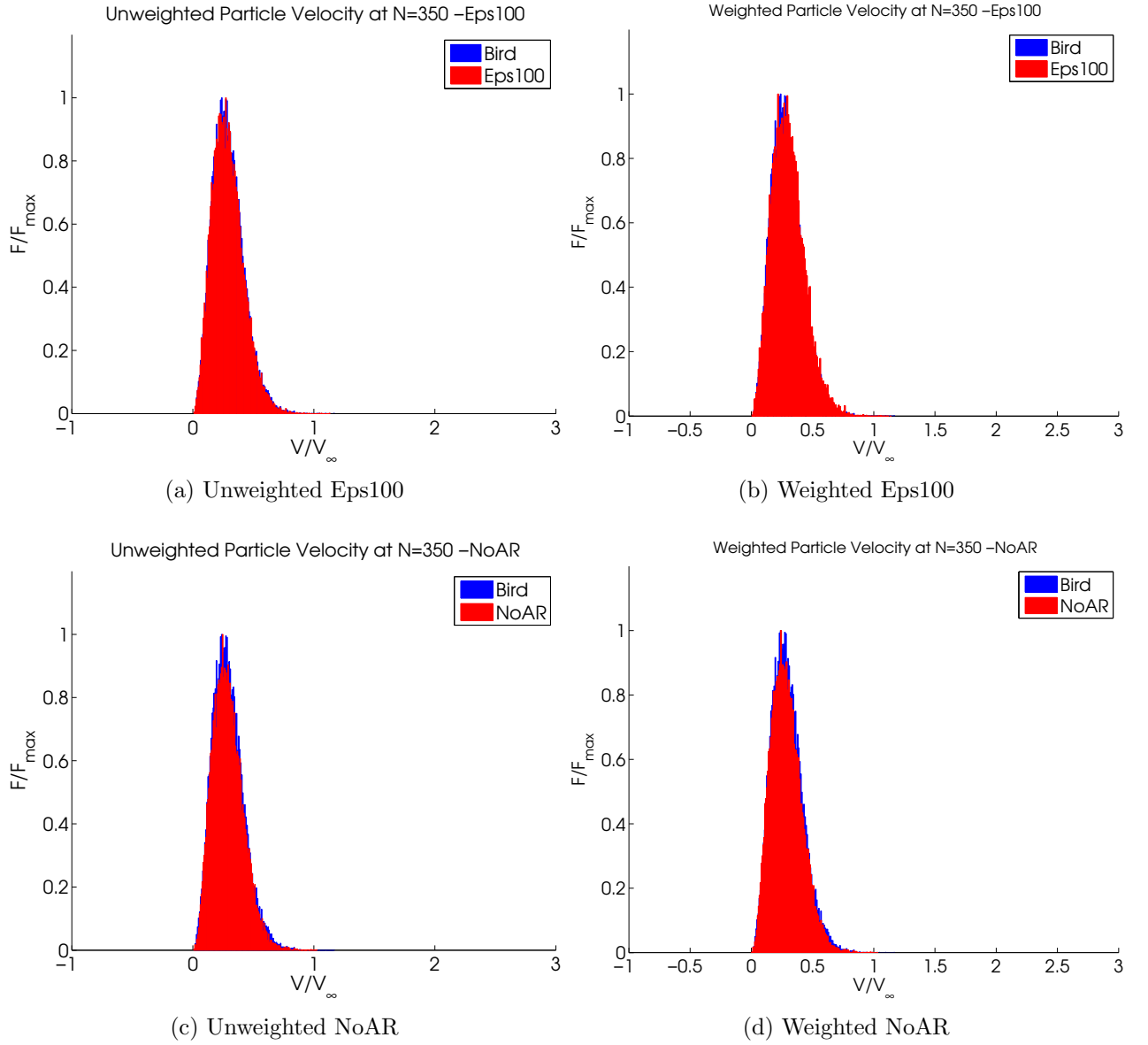
Figure 4.80:   Velocity Distributions for DSMC2A Case in Stagnation Region

are traveling faster as one would expect. Observing Figures 3.4 and 3.5, this sample location is within the area where the boundary layer and shock layer merge, so one would expect the particle velocities to be slower and for the distribution to be fairly wide.

The differences between the $\epsilon = 100\%$ and NoAR distributions and Bird's distribution are more noticeable at this sample location. The tops of these distributions

(a) Unweighted Eps00

(b) Weighted Eps00

(c) Unweighted Eps50

(d) Weighted Eps50
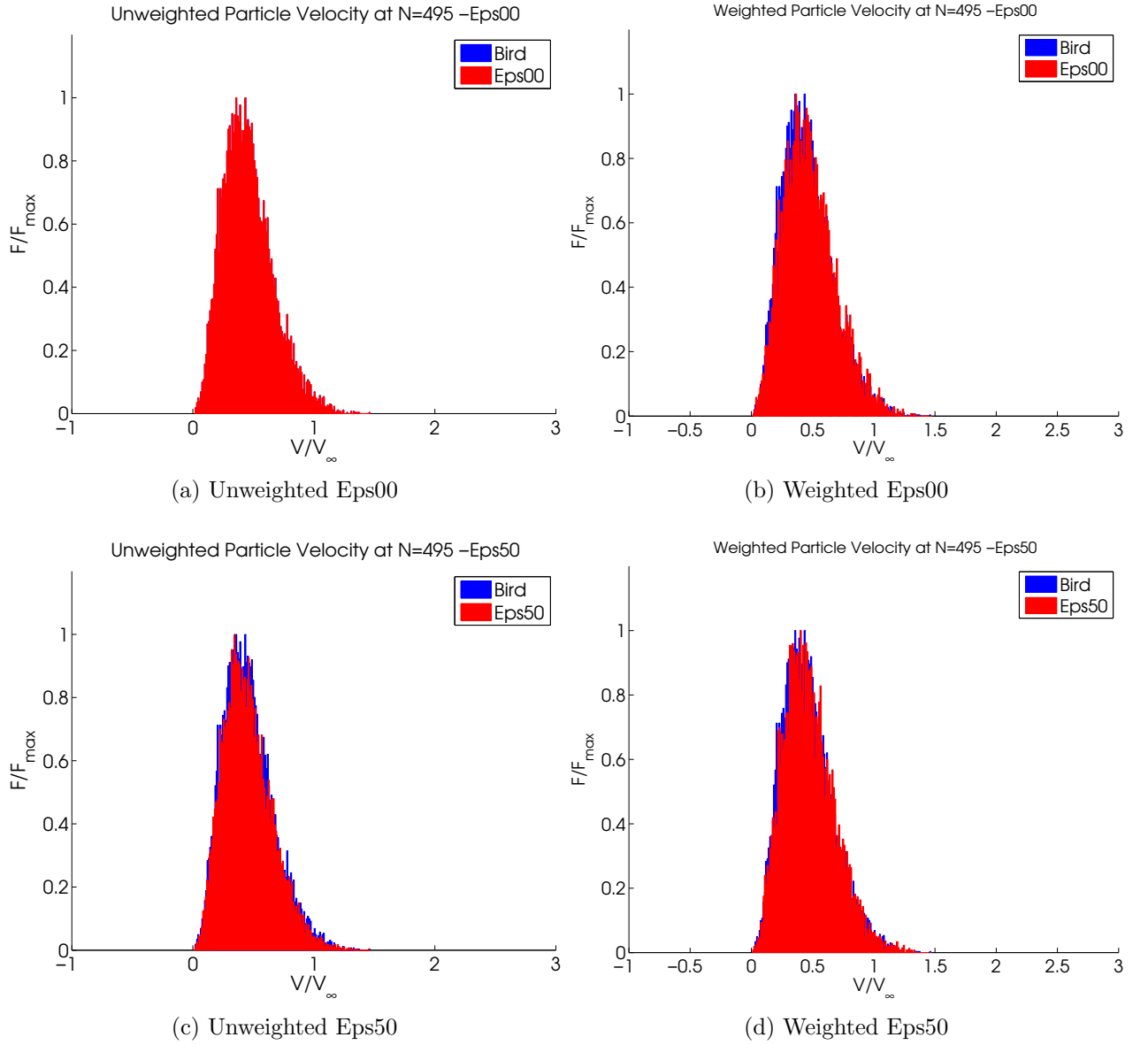
Figure 4.81:   Velocity Distributions for DSMC2A Case Before Step

are wide, and there is no clear point along the x-axis to name as C_{mp}. This sampling cell would have many particles at varying speeds due to the shock layer and boundary layer merging.

The sampling location for Figure 4.83 is similar to the the previous location. The sampling cells are at the same x location, but cell 795 is 2 mm higher than cell 495. At this height, the cell is not at the merging location of the boundary layer and

(a) Unweighted Eps100

(b) Weighted Eps100

(c) Unweighted NoAR

(d) Weighted NoAR
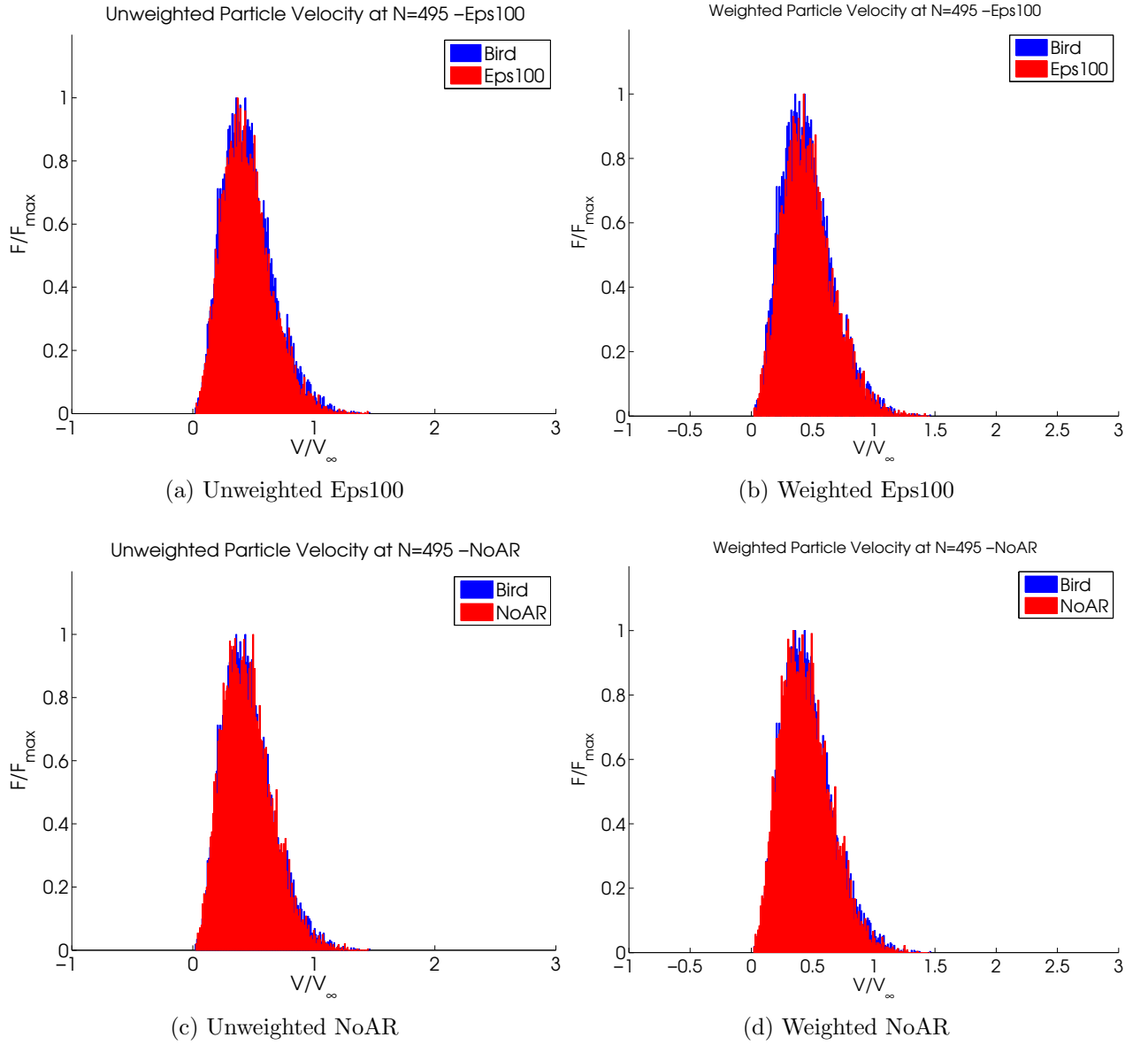
Figure 4.82:   Velocity Distributions for DSMC2A Case Before Step

shock layer, but it is still in the shock layer, which means the particles are moving slower than the bulk velocity. The distributions at this point are much wider than have been observed at the previous sampling locations. Additionally, the difference between the weighted $\epsilon = 50\%$ distribution and Bird's distribution is greater than previously seen.

(a) Unweighted Eps00

(b) Weighted Eps00

(c) Unweighted Eps50

(d) Weighted Eps50
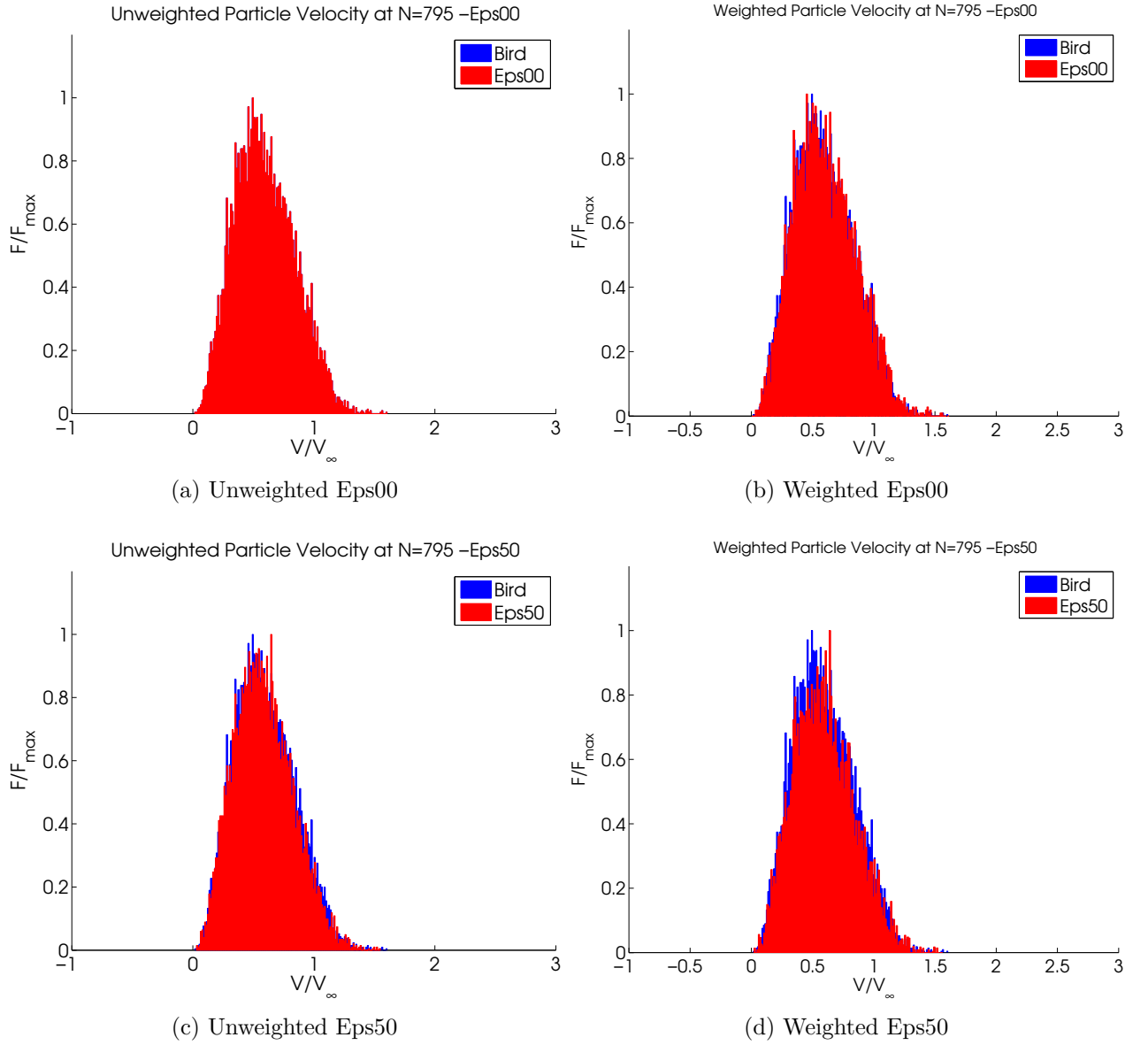
Figure 4.83:   Velocity Distributions for DSMC2A Case at Leading Edge of Step

In Figure 4.84, the weighted and unweighted $\epsilon = 100\%$ and NoAR distributions are similar to Bird's distribution. The NoAR distributions show slightly fewer particles traveling at or above the bulk velocity than Bird. Recalling the 1-dimensional distributions, it should not be a surprise that DSMC2A would predict more particles traveling at the bulk velocity compared to NoAR.

(a) Unweighted Eps100

(b) Weighted Eps100

(c) Unweighted NoAR

(d) Weighted NoAR
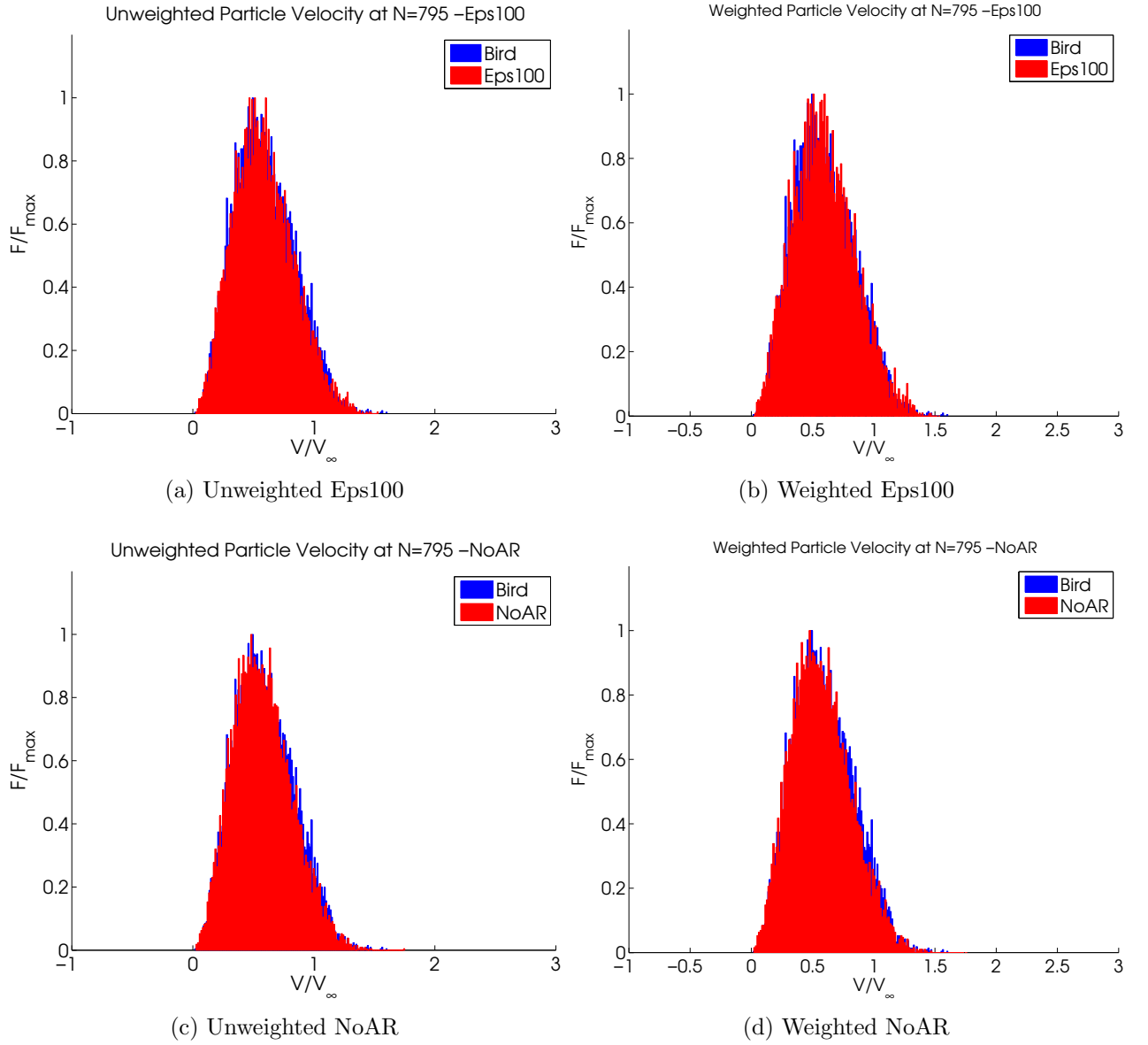
Figure 4.84:   Velocity Distributions for DSMC2A Case at Leading Edge of Step

Just after the step in Figure 4.85, all of the distributions are very similar to Bird, which may indicate that at this sampling location the particles are near the after shock equilibrium state.

Interestingly, the distribution in Figure 4.86 that shows the greatest change from Bird is the unweighted $\epsilon = 100\%$ case.

(a) Unweighted Eps00   (b) Weighted Eps00

(c) Unweighted Eps50   (d) Weighted Eps50
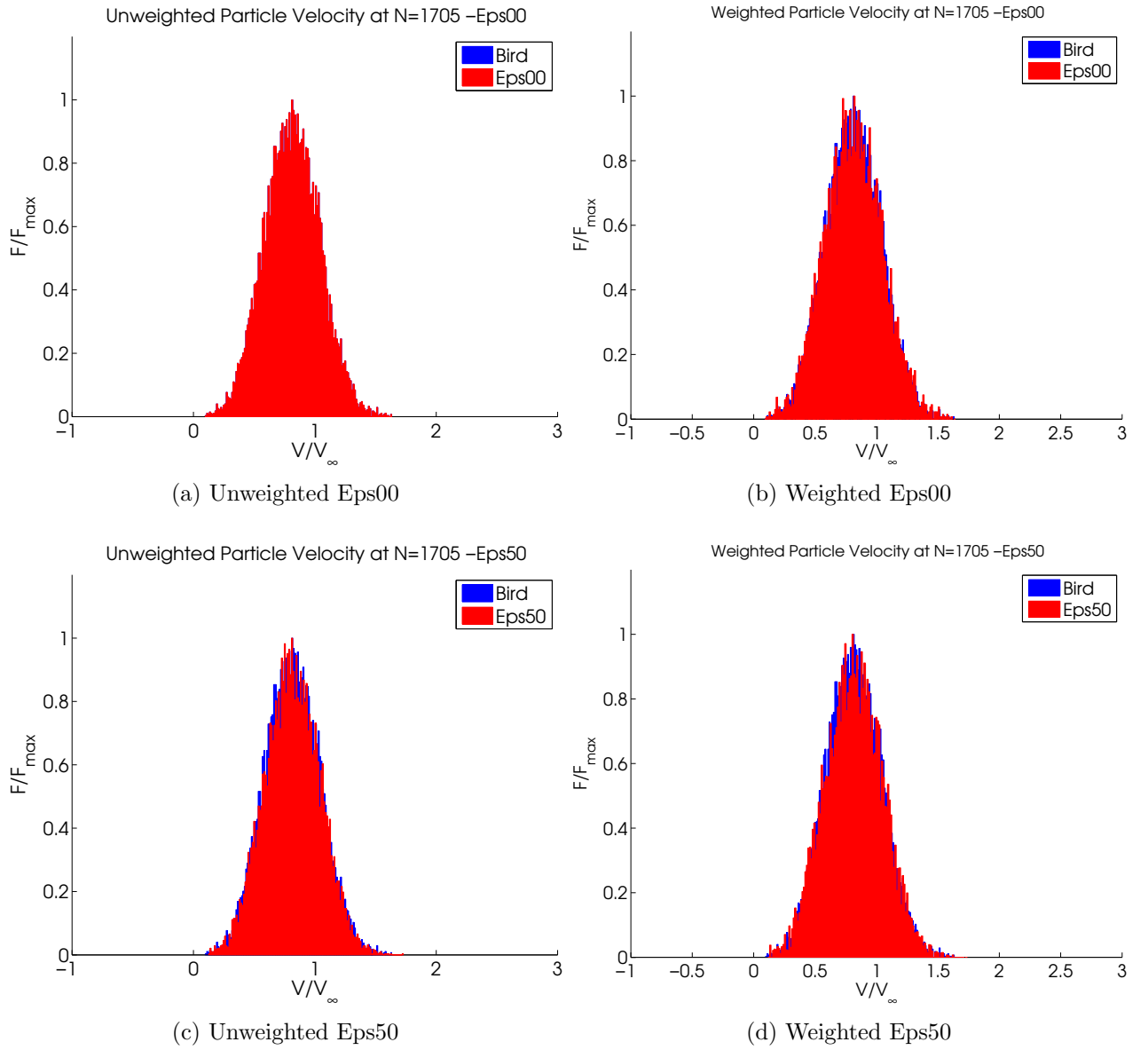
Figure 4.85:   Velocity Distributions for DSMC2A Case 1mm After the Step

Farther downstream of the step, at sample cell 1755, the particles distributions are fairly similar. None of the distributions are very smooth, which indicates a small sample size. Figure 4.56 shows that the number density behind the shock along the top of the step is low, which causes the jagged distributions and causes the inconsistencies noted in the contour plots with Bird's simulations.
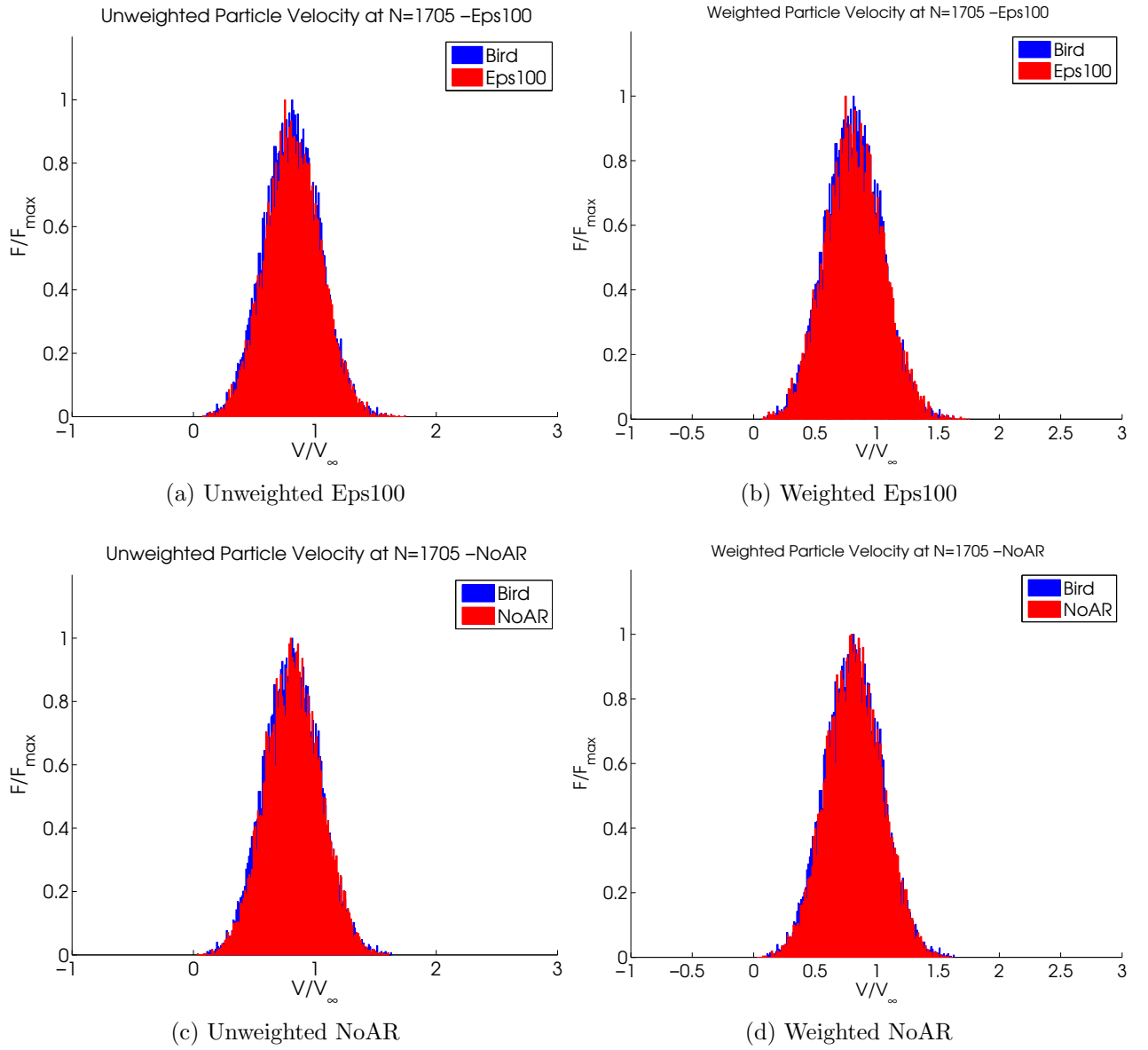
Figure 4.86:   Velocity Distributions for DSMC2A Case 1mm After the Step

The weighted $\epsilon = 100\%$ case shows the greatest difference compared to Bird at the current sample location.

(a) Unweighted Eps00   (b) Weighted Eps00

(c) Unweighted Eps50   (d) Weighted Eps50
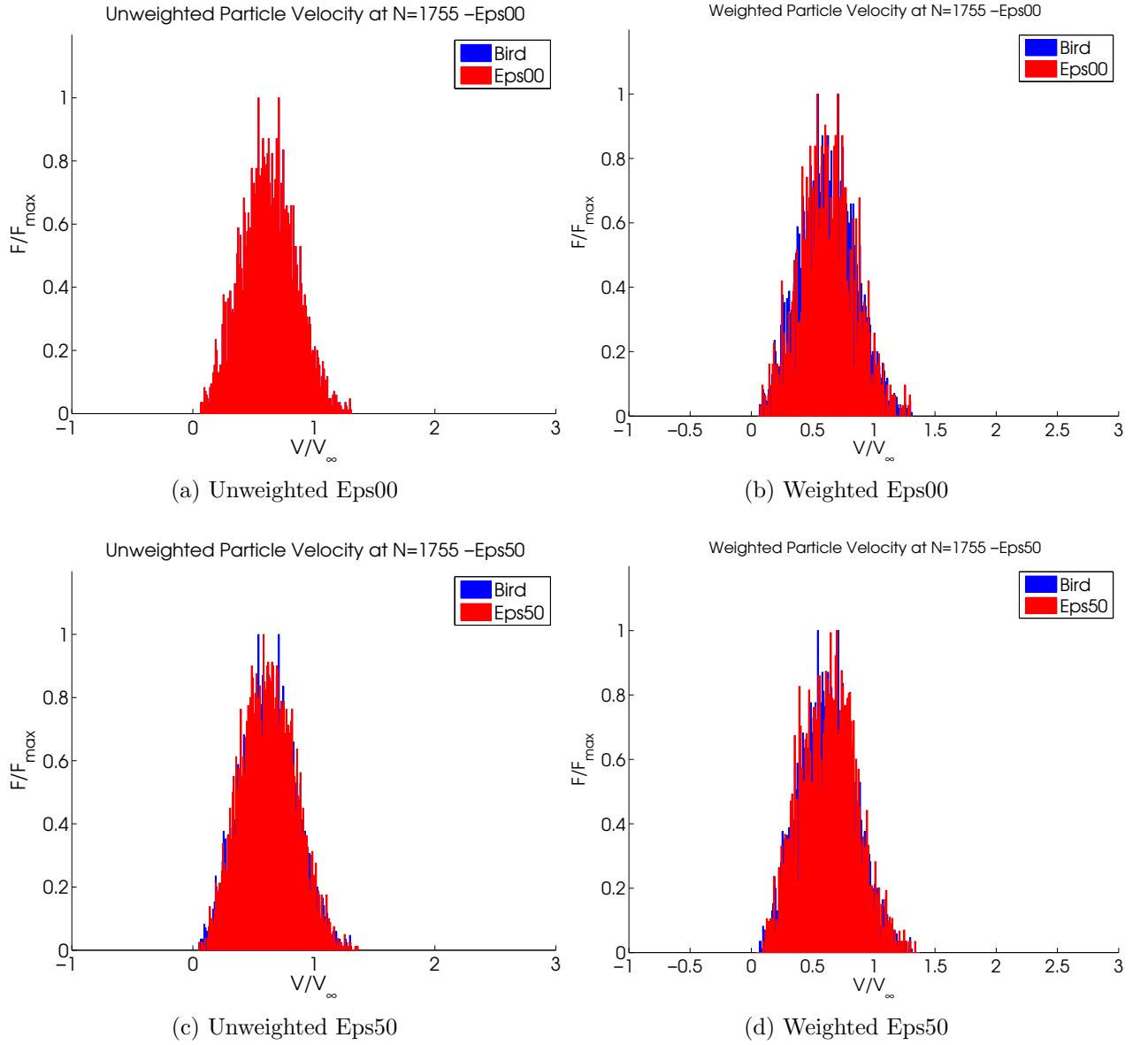
Figure 4.87:   Velocity Distributions for DSMC2A Case Downstream of the Step

The location of the shock layer differed amongst the simulations, as was seen in the contour plots. Bird and $\epsilon = 0\%$ have a shock layer than is farther from the body and thicker than the other simulations. Therefore, Bird and $\epsilon = 0\%$ distributions are very thin with a few particles in the wings. The unweighted $\epsilon = 50\%$ distribution is thin as well, but does not have as many particles in the wings, indicating that the sample cell in the $\epsilon = 50\%$ is farther from the shock layer compared to Bird. The
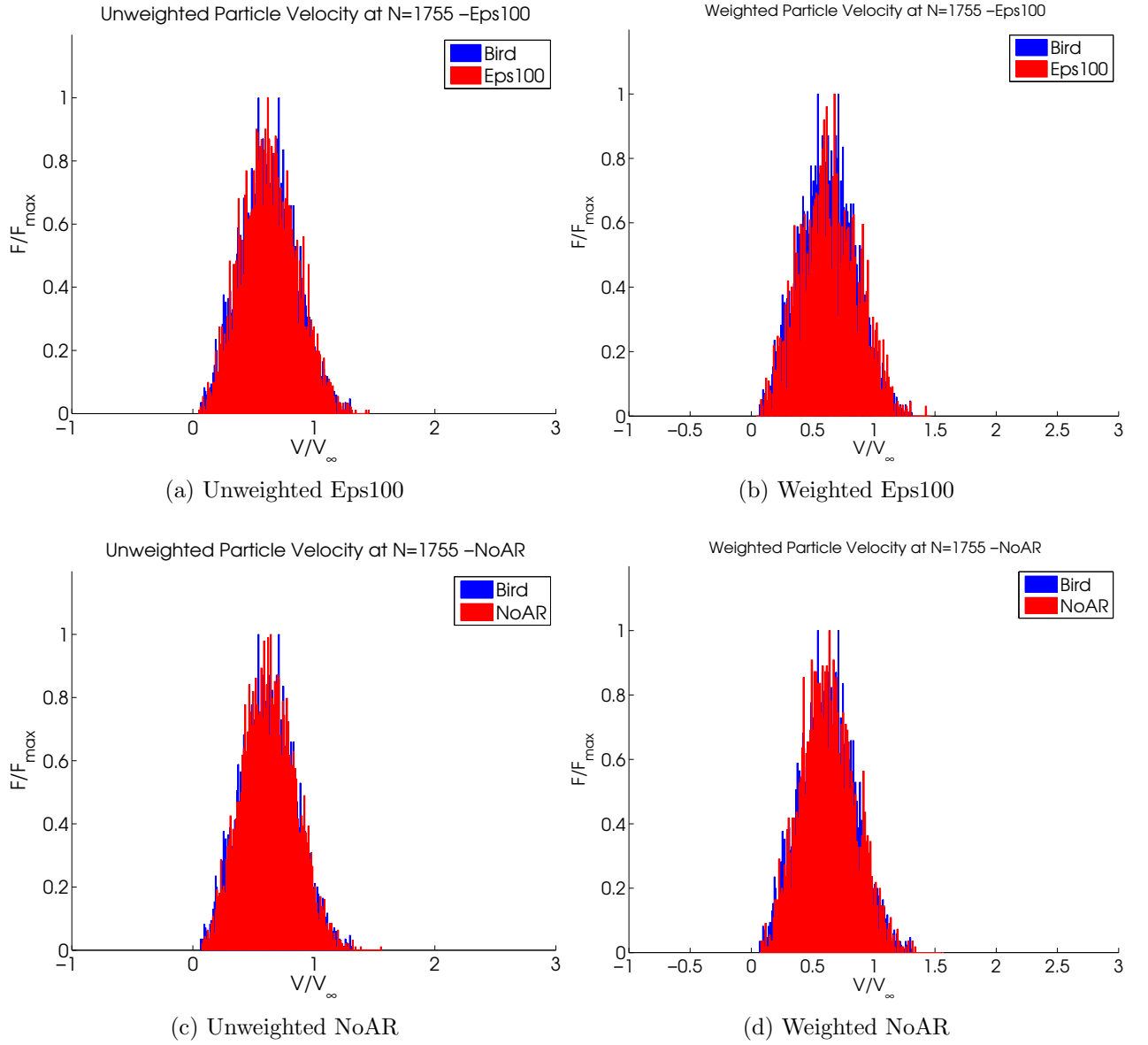
Figure 4.88:   Velocity Distributions for DSMC2A Case Downstream of the Step

weighted $\epsilon = 50\%$ has about the same number of particles in the wings because these
particles that are not at the bulk velocity have collided, hence the different velocities.

The $\epsilon = 100\%$ and NoAR distributions again show more particles near the bulk
velocity, indicating that the sample cell is not in the shock layer.

(a) Unweighted Eps00   (b) Weighted Eps00

(c) Unweighted Eps50   (d) Weighted Eps50
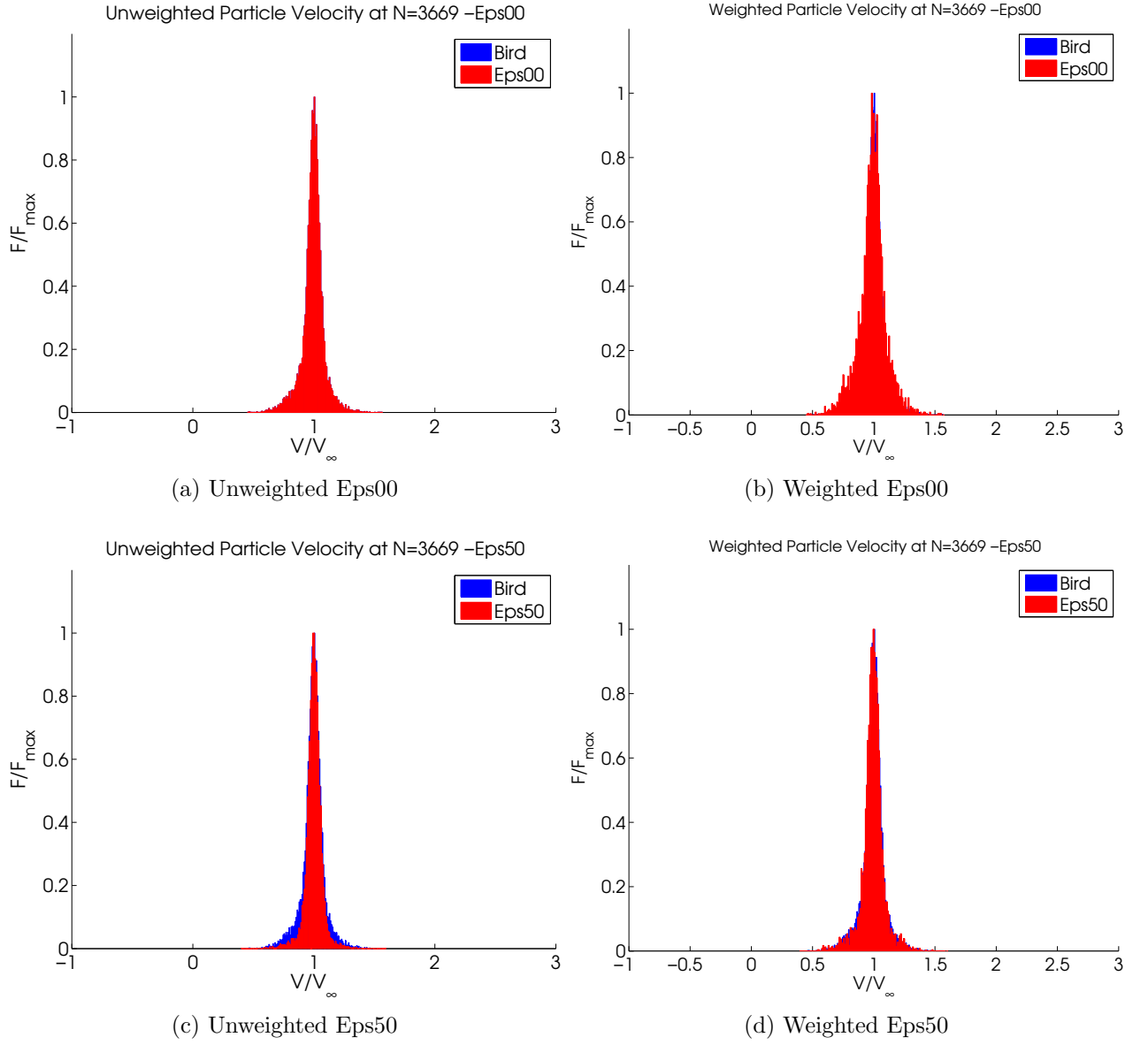
Figure 4.89:   Velocity Distributions for DSMC2A Case in Shock Layer

(a) Unweighted Eps100

(b) Weighted Eps100

(c) Unweighted NoAR

(d) Weighted NoAR

Figure 4.90:   Velocity Distributions for DSMC2A Case in Shock Layer

117

Table 4.6:   Distribution Properties For DSMC2A Simulations

Bird	Kurtosis	Skewness	Cmp	Avg Vel
495	1.9287	0.6757	728.18	930.52
795	1.6312	0.3718	1004.23	1206.81
350	2.4384	1.0009	485.69	595.24
3669	7.6340	2.3864	2037.71	2015.08
1705	1.7028	0.5148	1650.06	1647.81
1755	1.7987	0.3291	1101.59	1266.08

Eps00	Kurtosis	Skewness	Cmp	Avg Vel
495	1.9287	0.6757	728.18	930.52
795	1.6312	0.3718	1004.23	1206.81
350	2.4384	1.0009	485.69	595.24
3669	7.6340	2.3864	2037.71	2015.08
1705	1.7028	0.5148	1650.06	1647.81
1755	1.7987	0.3291	1101.59	1266.08

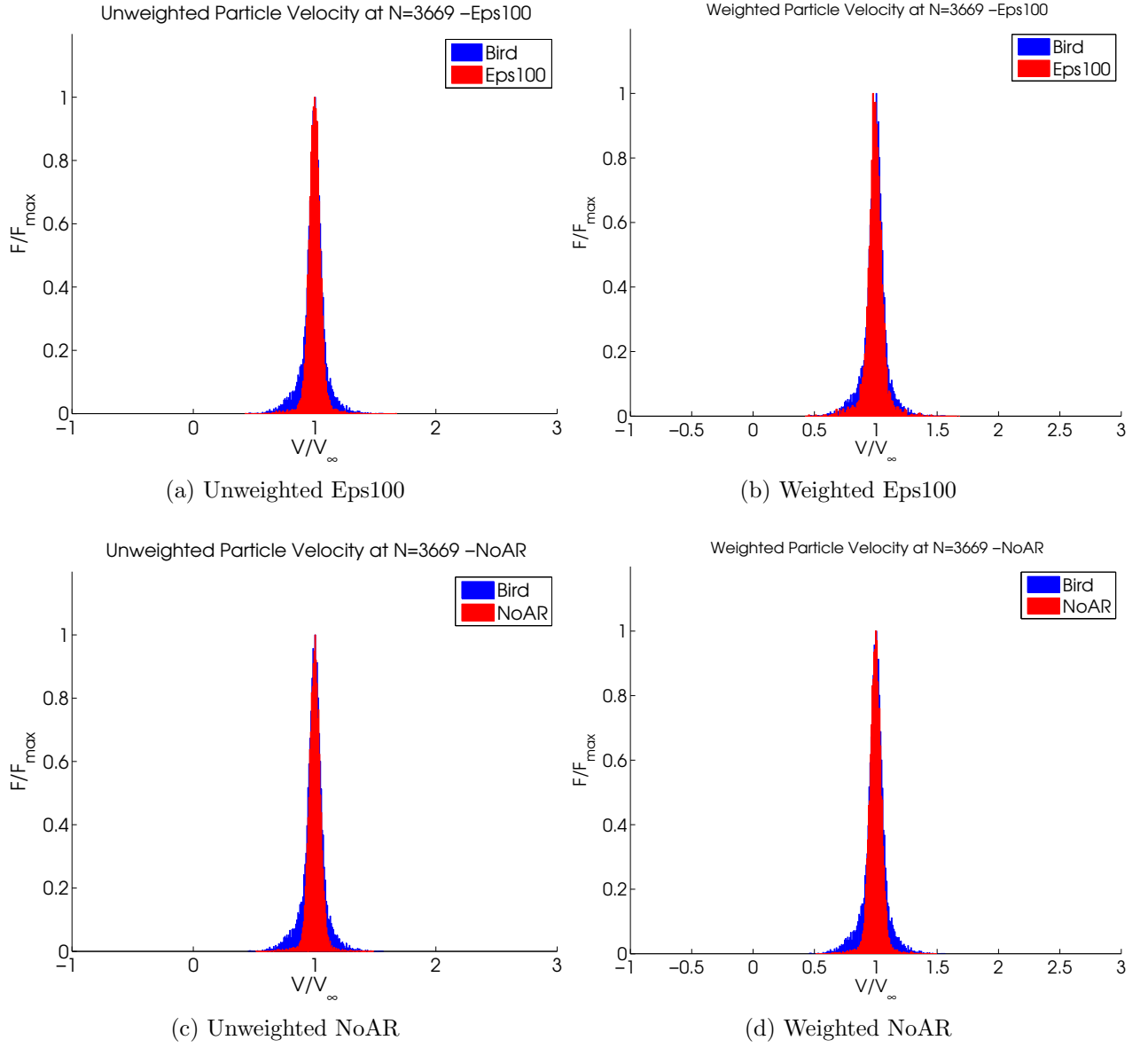| Eps25	Kurtosis	Skewness	Cmp	Avg Vel
495	1.9652	0.6749	743.82	924.68
795	1.5995	0.3164	1233.86	1197.04
350	2.5125	1.0360	492.20	596.26
3669	7.9278	2.4592	2027.63	2021.17
1705	1.7581	0.5297	1565.48	1658.40
1755	1.7277	0.5111	1258.97	1263.96

Eps50	Kurtosis	Skewness	Cmp	Avg Vel
495	2.0369	0.7172	697.99	922.54
795	1.6470	0.3745	1313.31	1187.32
350	2.1418	0.8453	514.38	593.24
3669	9.6403	2.7690	2014.41	2026.38
1705	1.8692	0.6067	1648.15	1652.61
1755	1.5609	0.2717	1186.09	1266.50

Eps75	Kurtosis	Skewness	Cmp	Avg Vel
495	2.0761	0.7281	741.33	910.85
795	1.5762	0.3321	1014.61	1181.70
350	2.5055	1.0185	547.18	593.34
3669	7.0833	2.3225	2035.59	2027.47
1705	1.8372	0.5897	1734.23	1666.23
1755	1.8564	0.4565	1358.77	1281.05

Eps100	Kurtosis	Skewness	Cmp	Avg Vel
495	2.0077	0.7222	750.70	911.47
795	1.7353	0.3966	949.55	1186.89
350	2.3224	0.9447	553.70	589.91
3669	10.0339	2.8572	2029.40	2027.33
1705	1.9272	0.6783	1530.80	1666.63
1755	1.7879	0.4319	1258.85	1279.68

NoAR	Kurtosis	Skewness	Cmp	Avg Vel
495	1.8315	0.6180	1011.21	916.90
795	1.7896	0.5803	980.27	1170.36
350	2.1030	0.8132	499.81	588.20
3669	7.5541	2.4122	2037.80	2029.24
1705	1.8650	0.6038	1627.75	1669.07
1755	1.8153	0.5213	1306.17	1276.72

(a) Unweighted

Eps00	Kurtosis	Skewness	Cmp	Avg Vel
495	1.9198	0.6349	739.12	979.30
795	1.6580	0.3800	919.92	1236.47
350	2.3359	0.9362	547.20	626.53
3669	5.5671	1.9010	1995.51	2012.54
1705	1.7426	0.5000	1661.69	1660.13
1755	2.1695	0.6175	1092.15	1282.78

Eps25	Kurtosis	Skewness	Cmp	Avg Vel
495	1.9652	0.6418	733.16	970.41
795	1.5995	0.3577	1222.33	1231.20
350	2.5125	0.9910	501.24	625.18
3669	7.9278	2.0934	2003.65	2017.97
1705	1.7581	0.5030	1670.70	1664.17
1755	1.7277	0.6966	1223.01	1290.67

Eps50	Kurtosis	Skewness	Cmp	Avg Vel
495	2.0369	0.6681	818.37	969.55
795	1.6470	0.4093	1301.79	1217.33
350	2.1418	0.8041	490.44	623.25
3669	9.6403	2.5059	2023.47	2023.36
1705	1.8692	0.5588	1636.00	1664.44
1755	1.5609	0.3811	1415.57	1295.48

Eps75	Kurtosis	Skewness	Cmp	Avg Vel
495	2.0761	0.6781	773.17	958.70
795	1.5762	0.3721	933.28	1212.79
350	2.5055	0.9396	609.01	621.01
3669	7.0833	2.1991	2028.38	2028.17
1705	1.8372	0.5943	1722.11	1682.86
1755	1.8564	0.5162	1262.01	1303.50

Eps100	Kurtosis	Skewness	Cmp	Avg Vel
495	2.0077	0.6963	869.19	956.80
795	1.7353	0.3854	1212.05	1221.74
350	2.3224	0.8836	442.98	621.19
3669	10.0339	2.7731	1982.18	2023.66
1705	1.9272	0.6393	1518.13	1674.38
1755	1.7879	0.5120	1376.14	1301.92

NoAR	Kurtosis	Skewness	Cmp	Avg Vel
495	1.8315	0.6175	697.77	915.52
795	1.7896	0.5835	967.21	1172.81
350	2.1030	0.8128	492.10	588.20
3669	7.5541	2.3963	2030.43	2029.13
1705	1.8650	0.6079	1615.81	1671.19
1755	1.8153	0.5941	1294.91	1282.84

(b) Weighted

In Figure 4.6, Bird and the unweighted $\epsilon = 0\%$ values are exactly the same, as expected since the distributions are colocated. The C_{mp} value is the lowest at sample cell 350 for all of the weighted and unweighted simulations, which makes sense since the cell is in the stagnation region. The largest C_{mp} value is at sample cell 3669, which is in the free stream for some simulations, but in the beginning of the shock later for Bird and $\epsilon = 0\%$. Kurtosis is highest for sample cell 3669, as expected since it has the thinnest distribution compared to the other cells. The lowest amount of kurtosis is located in cell 795, which was noted to have a wide distribution. Cells 795 and 1755 have low skewness values, indicating that the distributions are more symmetric compared to distributions from other cells. In general, the weighted distributions have lower skewness values compared to the unweighted distributions, just as was seen with the normal shock simulations.

4.5 Hard Sphere Comparisons

The last piece of this investigation is determining what results the SAR and NoAR algorithms give when using the HS model. Given the Mach dependency associated with both models, the question has been asked if the SAR algorithm could replace the VHS model, or if it is best used to augment it. The HS model was implemented for both the DSMC1S and DSMC2A codes, and the results have been compared to VHS results and experimental data.

4.5.1 1-Dimensional Shock.
The HS results were compared to the VHS results through looking at line plots and also comparing the inverse shock thickness calculations.

The dashed lines are the HS results and the solid lines are the VHS results. The shock is much thinner for the HS model than the VHS model.

The offset temperatures can be see again, but the HS results are farther off than the VHS results.
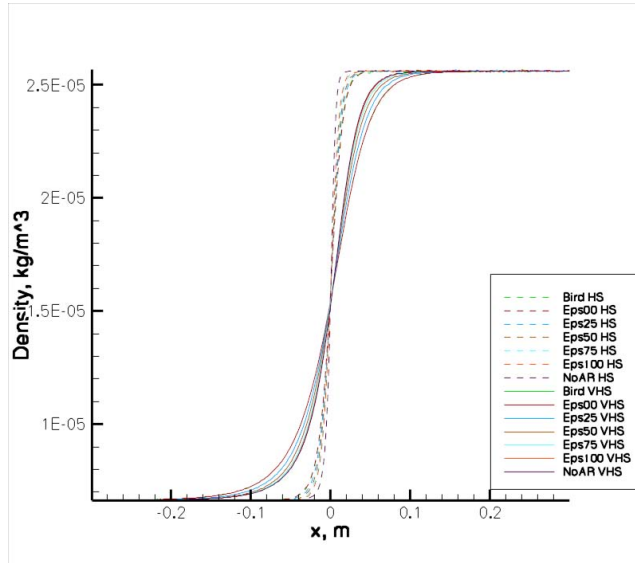
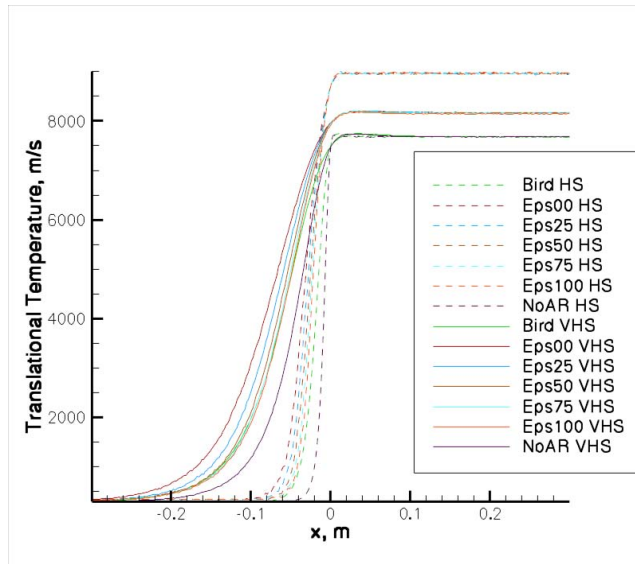Figure 4.91:   Normal Shock Density Line Plot

Figure 4.92:   Normal Shock Temperature Line Plot

The magnified figure better shows how the HS results for Bird and NoAR provide a consistent temperature as the VHS results, but the SAR VHS and HS results do not match.

Again, Figure 4.94 shows that the HS model has a much thinner shock, but the values before and after the shock match.
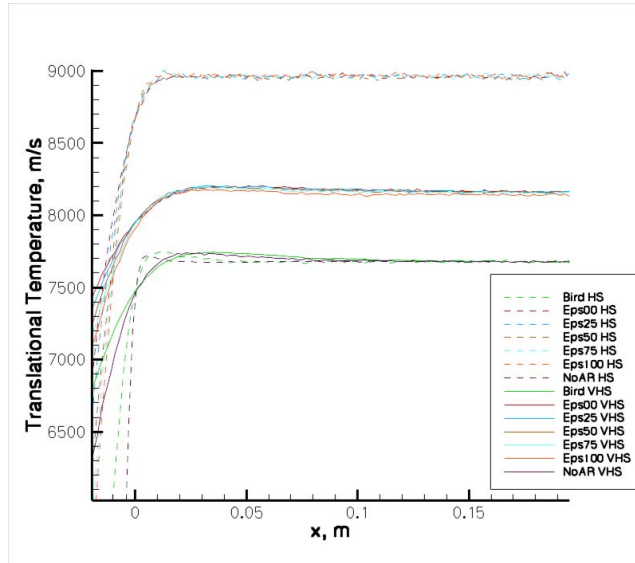
120

Figure 4.93:   Normal Shock Temperature Line Plot Magnifiied
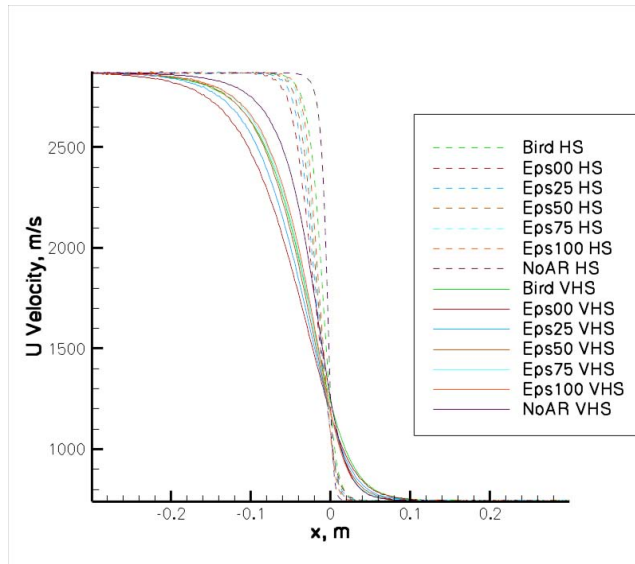

Figure 4.94:   Normal Shock U-Velocity Line Plot

The shock in Figure 4.95, the inverse shock thickness is clearly not consistent with experimental data, and SAR and NoAR results are actually worse than Bird's result.
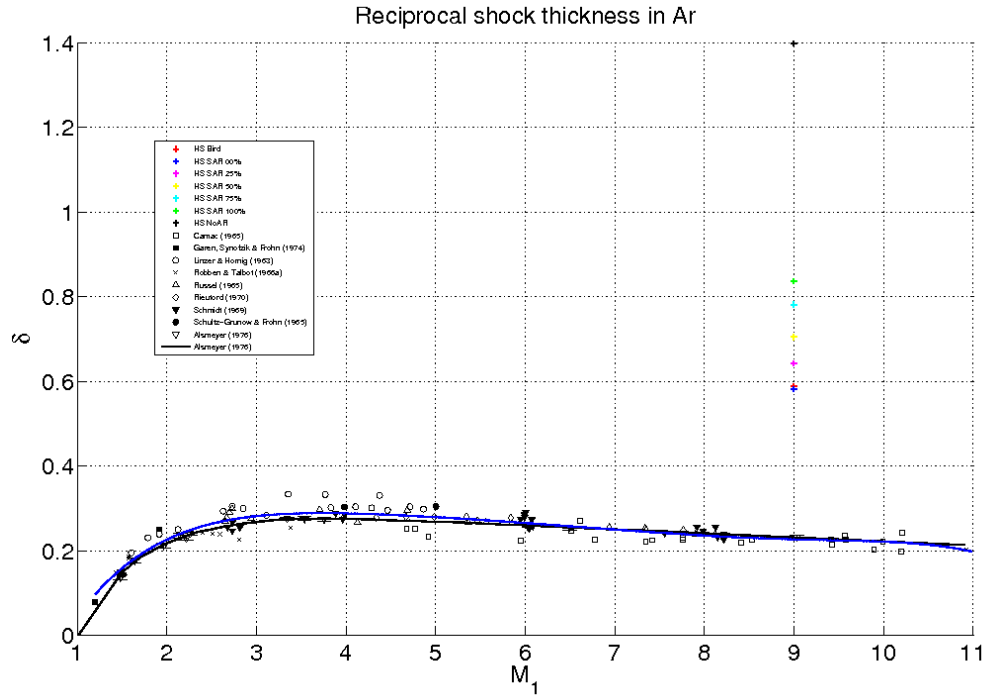
Figure 4.95:   Inverse Shock Thickness for HS Model at Mach 9

4.5.2   2-Dimensional Axisymmetric Cylinder.   The HS results provide similar comparisons to the Davis experimental data, but HS tends to exaggerate the change in density, which results in a long, pointed profile.
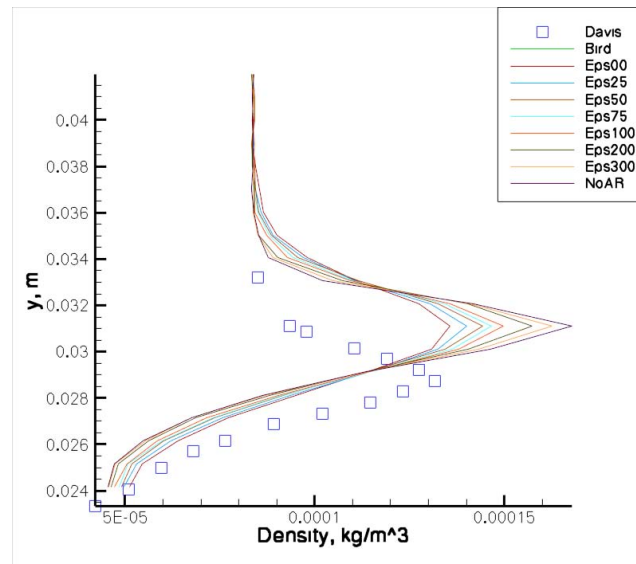

Figure 4.96:   HS Density Profile at x=.0313m

In Figure 4.96 Bird and $\epsilon = 0\%$ match closest to the experimental data, which differs from the VHS case by 50%.
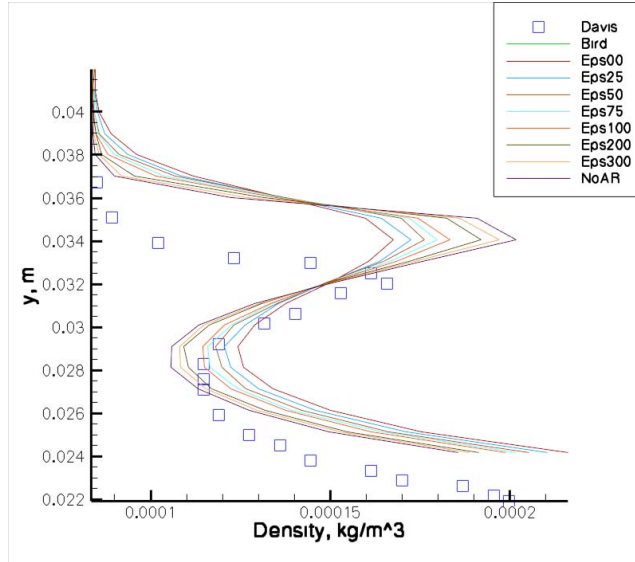
Figure 4.97:   HS Density Profile at x=.0462m

In Figure 4.97, $\epsilon = 25\%$ is the closest to experimental data, compared to 50% for the VHS results.
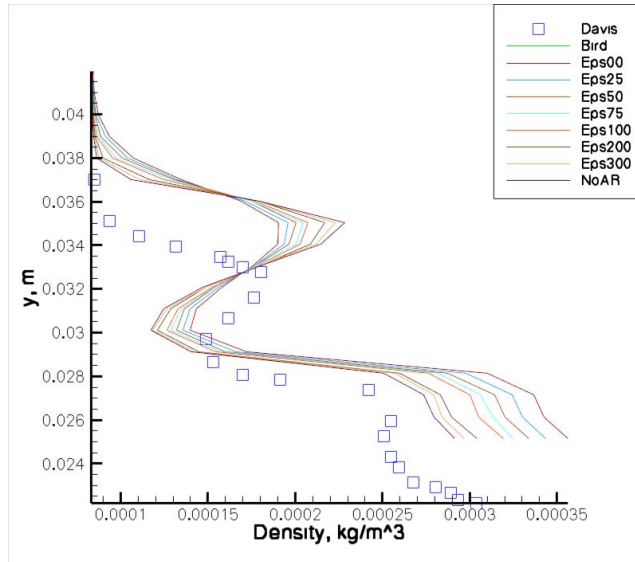
Figure 4.98:   HS Density Profile at x=.0495m

Bird and $\epsilon = 0\%$ are most comparable to the experimental data until y=0.029 m. Afterwards NoAR matches most closely. HS and VHS results are very similar at the step.
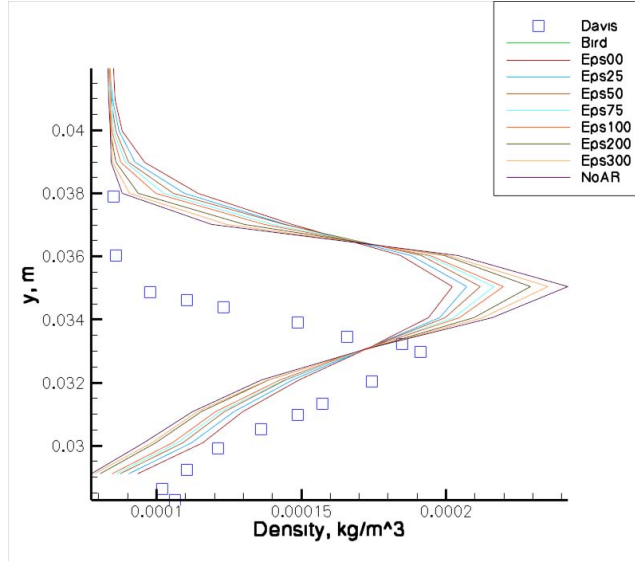
Figure 4.99:   HS Density Profile at x=.0509m

Again, the HS model results in a very pointed profile, and Bird and $\epsilon = 0\%$ match the closest to Davis' data. The profile farthest downstream is also extremely
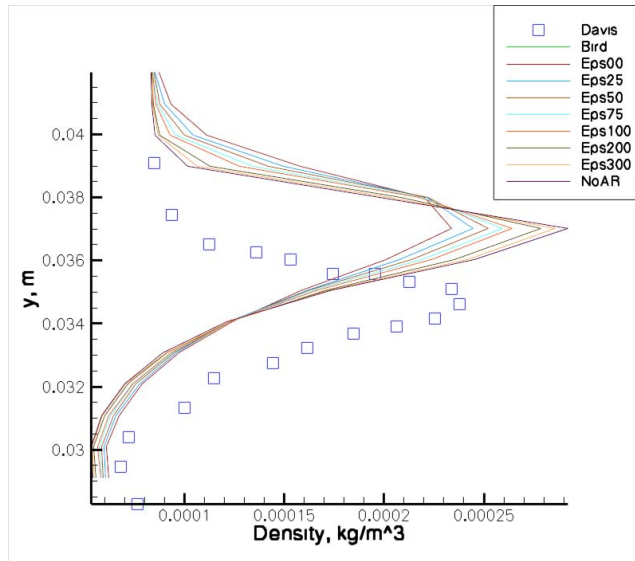
Figure 4.100:   HS Density Profile at x=.0561m

pointed and $\epsilon = 25\%$ matches most closely. The HS model consistently overpredicts the density gradient at the edge of the boundary layer compared to the VHS models, but actually underpredicts the density closer to the wall. The normal shock simulations also showed that the HS model overpredicts the density gradient.

V. Conclusions

5.1 Experimental Comparison

The current project has compared the new SAR and NoAR algorithms to three sets of experimental data: Alsmeyer's inverse shock thickness, velocity distribution by Holtz and Muntz, and Davis' 2-dimensional axisymmetric hollow cylinder. The Alsmeyer and Davis comparisons are based on the macroscopic density for the system, and certain SAR values do match the experimental data better than Bird. The inverse shock thickness plots show that as Mach number increases, the ϵ value must also increase in order to match the experimental data. An empirically derived curve fit was used to relate Mach number to ϵ. The comparison to Davis' data also demonstrates that SAR can be used to change DSMC2A results to best match the experimental data. Due to the complicated flowfield and the fact that the experiment occured at only one Mach number, a value of ϵ cannot be clearly labeled as the appropriate value for the simulation, and a Mach relationship cannot be identified. The main point made from the inverse shock thickness and hollow cylinder comparisons is that the user defined ϵ input allows for control over the flowfield in order to best match the experimental data. The potential exists after further research for SAR to be used as method of producing more accurate results for a multitude of DSMC simulations.

The velocity distributions allow for a deeper investigation into the effect of SAR and NoAR on the flowfield. Holtz and Muntz performed an experiment at Mach 7.18 to find the velocity distributions of the particles through a normal shock layer. Comparing these results to Bird, SAR, and NoAR shows that in equilibrium, the distributions are very nearly the same. The idea that in equilibrium the algorithms produce similar results is confirmed when looking at the macroscopic results. For the 1-dimensional normal shock, the line plots show that before and after the shock the values are the same, and only through the shock do the flowfield properties change with the exception of temperature. There is a problem with the way temperature is sampled which results in a higher value compared to Bird for SAR, but not NoAR. The DSMC2A code samples temperature the same way, but does not suffer from

the same problem. Further research into this matter is required. For DSMC2A, the percent difference plots show very little difference in flowfield parameters in the freestream. The differences were noticed in the shock layer, boundary layer, and stagnation region. These are areas where the gradients, and thus nonequilibrium are high. Velocity distributions were taken at three locations within the shock and compared to Holtz and Muntz. The plots definitively show that the SAR algorithm agrees with the experimental velocity distributions the best. The SAR algorithm differs from Bird's code in two respects: the collision rate, and flowfield sampling. The change in collision rate does alter the flowfield, but not significantly. The real change is due to the flowfield sampling. SAR and NoAR only sample particles that have collided during the current time step. The partial weighting associated with SAR allows particles to collide that normally would be rejected. While these partial collisions are weighted less than one, their inclusion changes the velocity profiles and allows for more accurate results. Bird's resulting velocity profiles show a significant number of particles at the bulk velocity deep in the shock layer, which according to the experimental data is not reasonable. The collision rate does not allow for local equilibration, which is a key assumption of DSMC, and the reason the velocity distributions show a spike at the bulk velocity within the shock. NoAR tended to produce velocity distributions that underestimate the number of particles traveling slower than the bulk velocity within the shock layer, as did $\epsilon = 100\%$.

5.2   Further Results

There is also important information to be gleaned from the other data not compared to experimental data. Velocity distributions were created for Mach numbers 1, 3, 6, and 9. The lower Mach numbers of 1 and 3 show that the DSMC simulation is able to maintain the local equilibrium distribution within the cell. The gradient within the shock is shallow enough that DSMC is accurate, which is why through Mach 3, the inverse shock thickness values are accurate. At Mach numbers 6 and 9, the velocity distributions within the shock are bimodal, indicating that the particles

are not in equilibrium with each other. The failure to maintain local equilibrium causes the simulation to take longer to equilibrate through the shock, which results in a thicker shock compared to experimental data. One situation that can cause a simulation to not maintain local equilibrium is a cell that is larger than the mean free path. In a shock layer, the density increases, which would in turn decrease the mean free path. The mean free path in the freestream is an order of magnitude larger than the cell size, but to rule out the possibility, a simulation with the cell size reduced by half was run. The resulting velocity distribution in the shock showed little appreciable difference from the original velocity distribution.

Running the DSMC2A code with a grid that was a quarter the size of the original grid resulted in requiring a smaller ϵ value to match results. The smaller grid allowed for the particles to maintain local equilibrium better, which means a smaller ϵ value can be used, just as a smaller ϵ value can match the inverse shock thickness for lower Mach numbers. The required ϵ input value is proportional to Mach number because the higher Mach numbers create more nonequilibrium within the shock layer, which needs to be overcome by a larger ϵ to allow for proper equilibration.

The VHS algorithm is already known to produce better results, and Figure 4.95 shows that even with SAR, the HS results do not compare well to experimental data. The HS density plots in Figures 4.96 through 4.100 show an exaggerated change in density compared to the VHS density profiles, and in general the SAR and NoAR results are actually farther from experimental data. Therefore, the HS model cannot be used in conjunction with SAR to produce accurate results.

5.3 Future Work

For SAR to be used in simulations a few things need to first occur: SAR needs to be compared to more complex simulations and geometry, and SAR needs to be compared to experiments having higher Mach numbers than the Alsmeyer data contains. In order for SAR to be used on cases with more complexity, SAR will need to be applied to a DSMC code that allows for geometries such as a blunt body, which has

been used in experiments. Bird has not made his more recent source codes available to the public, so a DSMC code would need to be developed specifically with the SAR modifications, or another open source DSMC code could be used for modification. The results of the SAR simulations can be compared to experimental data. Additionally, in order to understand the Mach dependency, further experimental comparisons that vary Mach number throughout the hypersonic regime will need to be completed. Additionally, the DSMC2A code was compared to experimental data at one Mach number, data that varies Mach number should be used to best compare DSMC to SAR and NoAR implemented into a 2-dimensional algorithm.

Bibliography

1. Alsmeyer, H., "Density Profiles in Argon and Nitrogen Shock Waves Measured by the Absorption of an Electron Beam," *Journal Fluid Mechanics*, Vol. 74, No. 3, 1976.

2. Dahm, W. J., "Technology Horizons A Vision for Air Force Science and Technology During 2010-2030," Tech. Rep. AF/ST-TR-10-01-PR, United States Air Force, 2010.

3. Rault, D. F. G., "Aerodynamics of Shuttle Orbiter at High Altitudes," *Journal of Spacecraft and Rockets*, Vol. 3, No. 6, 1994.

4. Bird, G., *Molecular Gas Dynamics and the Direct Simulation of Gas Flows*, Oxford University Press, Inc, New York, 1st ed., 1994.

5. Bird, G., "Application of the Direct Simulation Monte Carlo Method to the Full Shuttle Geometry," *AIAA/ASME 5th Joint Thermophysics and Heat Transfer Conference*, June 1990, AIAA Paper 1990-1692.

6. Moss, J. M., Bird, G. A., and Markelov, G. N., "DSMC Simulations of Hypersonic Flows and Comparison With Experiments," .

7. Bird, G., "Recent Advances and Current Challenges for DSMC," *Computers and Math Applications*, Vol. 35, No. 1/2, 1998.

8. Schwartzentruber, T. E. and Valentini, P., "Molecular Dynamics Simulation of Normal Shocks in Dilute Gases," *41st AIAA Thermophysics Conference*, June 2009, AIAA Paper 2009-3602.

9. Burt, J. M., Deschenes, T. R., Boyd, I. D., and Josyula, E., "Evaluation of a Hybrid Boltzmann-Continuum Method for High Speed Nonequilibrium Flows," *48th AIAA Aerospace Sciences Meeting*, January 2010, AIAA Paper 2010-1569.

10. Camberos, J., Greendyke, R., and Lambe, L., "On Direct Simulation Quasi-Monte Carlo Methods," *40th AIAA Thermophysics Conference*, June 2008, AIAA Paper 2008-3915.

11. Camberos, J. A., Greendyke, R. B., Lambe, L. A., and Bentley, B. I., "Computational Experiments with Direct Simulation Quasi-Random Monte Carlo," *41st AIAA Thermophsyics Conference*, San Antonio, TX, 2009.

12. Vincenti, W. G. and Kruger, Charles H., J., *Introdruction to Physical Gas Dynamics*, Krieger Publishing Company, Malabar, FL, 1st ed., 1965.

13. Harris, S., *An Introduction to the Theory of the Boltzmann Equation*, Dover Publications, Inc, Mineloa, NY, 1st ed., 2004.

14. Greendyke, R. B. and Summers, S. E., "A Smoothed Accept-Reject Algorithm for Collisional Modeling in DSMC," *10th AIAA/ASME Joint Thermophysics and Heat Transfer Conference*, Chicago, IL, 2010.

15. Bird, G., "Definition of Mean Free Path for Real Gases," *Physics of Fluids*, Vol. 26, No. 11, November 1983.

16. Bird, G., "Monte-Carlo Simulation in an Engineering Context," *12th International Symposium on Rarefied Gas Dynamics*, Charlottesville, VA, 1980.

17. Davis, J., *An Experimental Study to Evaluate and Develop the Direct-Simulation as Applied to Rarefied Hypersonic Flow Fields*, Ph.D. thesis, Imperial College, June 1978.

18. Harvey, J., Jeffery, R., and Uppington, D., "The Imperial College Graphite Heated Hypersonic Windtunnel," Tech. rep., Department of Aeronautics, Imperial College, 1972.

19. Holtz, T. and Muntz, E., "Molecular velocity distribution functions in an argon normal shock wave at Mach number 7," *Physics of Fluids*, Vol. 26, No. 9, September 1983.

20. Berg, B. A., *Markov Chain Monte Carlo Simulations and Their Statistical Analysis*, World Scientific, Singapore, 2004.

Vita

Captain Sarah Summers graduated from Oklahoma State University in 2005 with degrees in Mechanical and Aerospace Engineering and commissioned into the Air Force through ROTC. Her first position was as an aircraft maintenance officer in the 552d Air Control Wing at Tinker Air Force Base, OK. There, she held multiple positions including Computers Flight Commander, Support Flight Commander, Red Aircraft Maintenance Unit (AMU) Assistant Officer-in-Charge (OIC), Quality Assurance Flight Commander, and Maintenance Group Executive Officer. She deployed to CENTCOM for five months and performed a Presidential support deployment both as the AMU OIC during her time in the 552d ACW. She was accepted into AFIT in November 2008, and has a follow-on assignment to the Air Vehicles Directorate in the Air Force Research Labs at Wright-Patterson AFB, OH.

Permanent address: 2950 Hobson Way
Air Force Institute of Technology
Wright-Patterson AFB, OH 45433

REPORT DOCUMENTATION PAGE

Form Approved
OMB No. 0704–0188

1. REPORT DATE *(DD–MM–YYYY)*	2. REPORT TYPE	3. DATES COVERED *(From — To)*
24–03–2011	Master's Thesis	Aug 2009 — Mar 2011

4. TITLE AND SUBTITLE

Improved Collision Modeling for Direct Simulation Monte Carlo Methods

5a. CONTRACT NUMBER

5b. GRANT NUMBER

5c. PROGRAM ELEMENT NUMBER

6. AUTHOR(S)

Summers, Sarah E., Capt, USAF

5d. PROJECT NUMBER

5e. TASK NUMBER

5f. WORK UNIT NUMBER

7. PERFORMING ORGANIZATION NAME(S) AND ADDRESS(ES)

Air Force Institute of Technology
Graduate School of Engineering and Management (AFIT/EN)
2950 Hobson Way
Wright-Patterson AFB, OH 45433-7765

8. PERFORMING ORGANIZATION REPORT NUMBER

AFIT/GAE/ENY/11-M29

9. SPONSORING / MONITORING AGENCY NAME(S) AND ADDRESS(ES)

John Schmisseur john.schmisseur@afosr.af.mil Office of Scientific Research 875 North Randolph Street, Suite 325, Room 3112 Arlington, Va., 22203-1768 DSN 426-6962

10. SPONSOR/MONITOR'S ACRONYM(S)

OSR

11. SPONSOR/MONITOR'S REPORT NUMBER(S)

12. DISTRIBUTION / AVAILABILITY STATEMENT

APPROVED FOR PUBLIC RELEASE; DISTRIBUTION UNLIMITED.

13. SUPPLEMENTARY NOTES

This material is declared a work of the U.S. Government and is not subject to copyright protection in the United States.

14. ABSTRACT

In the Smoothed Accept/Reject (SAR) algorithm, the accept/reject criteria is altered from Direct Simulation Monte Carlo (DSMC): rather than a binary function of rejection or acceptance, collisions can be partially accepted with a linear weighting between zero and one. The partial acceptance is based on a band around the original accept/reject criteria defined as a percentage of the collision criteria, which is called ϵ. A relationship previously noted between Mach and ϵ is explored. Velocity distributions of the particles are examined for all algorithms and compared to experimental data to determine the effect of the SAR algorithm at a microscopic level. All of the comparisons to experiment show a Mach dependency that has previously been noted, and the dependency was defined for the normal shock simulations. DSMC does adequately simulate the nonequilibrium within the cells at a high Mach number through the shock, but SAR does. The SAR algorithm models the flowfield in the shock better than DSMC through a change in the collision rate and particle sampling methods, which allows for a more accurate simulation.

15. SUBJECT TERMS

Direct Simulation Monte Carlo, hypersonics, Mach number, shock layer

16. SECURITY CLASSIFICATION OF:			17. LIMITATION OF ABSTRACT	18. NUMBER OF PAGES	19a. NAME OF RESPONSIBLE PERSON
a. REPORT	b. ABSTRACT	c. THIS PAGE			Dr. Robert Greendyke (ENY)
U	U	U	UU	150	19b. TELEPHONE NUMBER *(include area code)* (937) 785-3636x4567; robert.greendyke@afit.edu

Standard Form 298 (Rev. 8–98)
Prescribed by ANSI Std. Z39.18